CMB Angular Power Spectra and Cosmological Implications from the 2003 LDB Flight of the BOOMERANG Telescope

by

Carolyn Judith MacTavish

A thesis submitted in conformity with the requirements
for the degree of Doctor of Philosophy
Graduate Department of Physics
University of Toronto

Your file Votre référence
ISBN: 978-0-494-15923-1
Our file Notre référence
ISBN: 978-0-494-15923-1

Abstract

CMB Angular Power Spectra and Cosmological Implications from the 2003 LDB Flight of the BOOMERANG Telescope

Carolyn Judith MacTavish

Doctor of Philosophy

Graduate Department of Physics

University of Toronto

June 2006

In January 2003 the BOOMERANG telescope completed a second successful flight over the Antarctic continent. In this thesis an overview of the BOOMERANG instrument is given, with emphasis on the pointing system. The analysis of the BOOMERANG 2003 (B03) flight data from Cosmic Microwave Background (CMB) maps to angular power spectra is also described. The final B03 temperature angular power spectrum represents the most precise *intermediate* scale measurement of CMB temperature anisotropy to date. The final polarization power spectrum represents a $\sim 5\sigma$ detection in the $\ell = 100$ to $\ell = 1000$ multipole range. The Polarization Sensitive Bolometers (PSBs) used in B03 are the first of their kind and will be used in the High Frequency Instrument (HFI) on the Planck Surveyor satellite. The successful B03 CMB anisotropy measurements using PSBs represents a critical first step for the Planck satellite mission.

The B03 data alone constrains the parameters of the *standard* ΛCDM model–a Universe in which Cold Dark Matter and a cosmological constant, Λ, are the dominant energy components–remarkably well and is consistent with constraints from a multi-experiment combined CMB data set (hereafter CMBall). Several extensions to the standard model are tested using both the CMBall data set and a combined CMBall + Large Scale Structure (LSS) data set. The resulting constraints from the CMBall+LSS data set, representing the most up-to-date parameter analysis, are: slight evidence (both $< 2\sigma$) for a run-

ning index and curvature; an upper (95% confidence) limit on the tensor-to-scalar ratio of $A_t/A_s < 0.36$; an upper (95% confidence) limit on the neutrino mass of $m_\nu < 0.40\,\mathrm{eV}$ $m_\nu < 0.4eV$ ($m_\nu < 1.0eV$ from CMB data alone); and, after adding the supernova (SNIa) data, a constraint on the dark energy equation of state of $w = -0.94^{+0.093}_{-0.097}$ (68% confidence interval). Also included is an analysis of the CMBall + HST (H_0 value determined from the Hubble Space Telescope Key Project) constraints to a model which includes a CDM isocurvature mixture. The resulting allowed isocurvature CMB bandpower contamination is only a few percent.

For Mom and Dad

Acknowledgements

Thanks to the entire BOOMERANG Antarctic field team for being part of the experience of a lifetime; particularly to Barth Netterfield, Francesco Piacentini, Ted Kisner, Bill Jones, Enzo Pascale, Tom Montroy and Brendan Crill. It was an honour to work with Brendan Crill, Tom Montroy, Carlo Contaldi and Bill Jones during the long, hard years of data analysis. Thanks to my theorist friends Carlo Contaldi, Antony Lewis and Dick Bond for their patience and guidance in parameter estimation. Thanks to my committee members, Kim Strong and Norm Murray, for their positive feedback and accessibility. Finally, thanks especially to Barth Netterfield for his continuous support on all matters, both large and small, throughout my degree. Every graduate student should be so lucky as to have a supervisor with such boundless enthusiasm, limitless knowledge and an ability to both challenge and inspire.

This thesis wouldn't have been possible without the support of my family and friends. Thanks especially to Jen Cutts, Heather MacLeod, Randy Ray, Tammy Grime, Jen Egsgard, Nicole Fram, Rebecca Kohler and A.K. Cowdy. Thanks to the all the fabulous ladies of the book club and to my improv buddies. Thanks most of all to my family: to Matt for climbing the walls with me and for being such a good listener; to Alli for reminding me that I am a sun worshiper and that there is a whole world out there; to Mom for her infinite wisdom and endless supply of kind words; and to Dad for inspiring me to do this in the first place.

BOOMERANG Collaboration

Case Western Reserve University J. Ruhl, T. Kisner, E. Torbet, T. Montroy

Universita' di Roma La Sapienza P. de Bernardis, S. Masi, F. Piacentini, A. Iacoangeli, G. De Troia, A. Melchiorri G. Polenta, S. Ricciardi, F. Nati, P. Santini, M. Veneziani

California Institute of Technology A. Lange, W. Jones, V. Hristov

University of Toronto B. Netterfield, C. MacTavish, E. Pascale

Cardiff University P. Ade, P. Mauskopf

IROE Andrea Boscaleri

ING G. Romeo, G. di Stefano

JPL J. Bock

IPAC E. Hivon, B. Crill

CITA D. Bond, A. M. Lewis

LBNL, UC Berkeley J. Borrill

Imperial College A. Jaffe, C. Contaldi

Institut d'Astrophysique S. Prunet

University of Alberta D. Pogosyan

Universita' di Roma Tor Vergata N. Vittorio, G. de Gasperis, P. Natoli, A. Balbi, P. Cabella

MIT M. Tegmark, A. de Oliveira-Costa

Contents

List of Tables

List of Figures

Table of Acronyms

ACBAR	Arcminute Cosmology Bolometer Array Receiver Experiment
ACS	Attitude Control System
B03	BOOMERANG 2003 Flight
B98	BOOMERANG 1998 Flight
BB	B-mode Polarization Angular Power Spectrum
BOOMERANG	Balloon Observations of Millimetric Extragalactic Radiation And Geophysics
CBI	Cosmic Background Imager Experiment
CCD	Charge-Coupled Device
CMB	Cosmic Microwave Background
DAS	Data Acquisition System
DASI	Degree Angular Scale Interferometer Experiment
EB	E-mode–B-mode Angular Cross Power Spectrum
EE	E-mode Polarization Angular Power Spectrum
FLC	Flight Logic Computer
FSS	Fixed Sun Sensor
RF	Radio Frequency
RW	Robertson Walker metric
FRW	Friedman-Robertson Walker solution
GPS	Global Positioning System
HFI	High Frequency Instrument the Planck Surveyor Satellite
HST	Hubble Space Telescope
JFET	Junction Field Effect Transistor
ΛCDM	Λ Cosmological Constant-Cold Dark Matter Model
LSS	Large Scale Structure
MAXIMA	Millimeter Anisotropy Experiment Imaging Array
NTD	Neutron Transmutation Doped
PID	Proportional-Integral-Derivative Control Algorithm
PSS	Pointed Sun Sensor
PSB	Polarization Sensitive Bolometer
PSD	Power Spectral Density
PV	Pressure Vessel
PWM	Pulse Width Modulated
SC	Star Camera
SDSS	Sloan Digital Sky Survey
TB	Temperature–B-mode Polarization Angular Cross Power Spectrum
TE	Temperature–E-mode Polarization Angular Cross Power Spectrum
TOD	Time-Ordered Data
TT	Temperature Angular Power Spectrum
2dFRG	Two Degree Field Galaxy Redshift Survey
VSA	The Very Small Array Experiment
WMAP	Wilkinson Microwave Anisotropy Probe Experiment

Chapter 1

Introduction

BOOMERANG is a balloon-borne, microwave telescope designed to measure the intensity and polarization anisotropies of the Cosmic Microwave Backgound (CMB). The CMB is a field of electromagnetic radiation that is *cosmic* in origin, that is originating from the Universe itself. It radiates in the *microwave*, ranging from 0.3 GHz to 630 GHz, with a near perfect blackbody spectrum which peaks at 160.4 GHz, corresponding to a temperature of 2.725 K. The CMB covers the entire sky and appears as a *background* behind all other objects for instance stars, galaxies, etc. While the CMB is extremely uniform, there are tiny fluctuations or anisotropies in CMB intensity and polarization. These anisotropies trace tiny non-uniformities in the early Universe which grow into the large scale structure observed in the sky today.

Polarization of a radiation field is generally expressed in terms of the *Stokes parameters* I, Q, U and V. The latter, the Stokes V, characterizes circular polarization and since the CMB is not expected to be circularly polarized it can be ignored. The Stokes I describes the radiation intensity, while Q and U represent linear polarization. Note that since the CMB field is conventionally described in terms of temperature all of these quantities are determined in μK and the Stokes I is sometimes replaced by T. So the inital observables (derived from the raw data) that BOOMERANG obtains are T, Q

and U maps describing the temperature and polarization anisotropies of the CMB sky in units of μK.

In cosmology it has become both customary and convenient to provide a statistical description of the CMB anisotropies (the T, Q, U maps) in the form of their *angular power spectra.* CMB fluctuations are distributed over the surface of a sphere (the sky). The spherical harmonic transform of the CMB field is the spherical polar equivalent of the Fourier transform of a density field described in three Cartesian dimensions. From the amplitudes of the spherical harmonic components the angular power spectra may be constructed in terms of the variance, C_ℓ, of the CMB fluctuations as a function of multipole number ℓ. For example the measured CMB temperature fluctuation field, T, can be decomposed in terms of the spherical harmonic coefficients

$$a_{T,lm} = \int d\Omega {Y^0_{lm}}^* T(\hat{\mathbf{n}})$$

where the term Y^0_{lm} represents the spherical harmonic functions and $\hat{\mathbf{n}}$ is the line of sight unit vector. The temperature angular power spectrum (in shorthand TT) is then

$$C_l^{TT} = \frac{1}{2l+1} \sum_m < a^{T*}_{lm} a^T_{lm} > . \tag{1.1}$$

The multipole or angular wavenumber, ℓ, of a spherical harmonic mode is related to an angular separation on the sky of $\theta \approx \pi/\ell$.

The polarization field is a bit more complicated to describe. From linear combinations of Q and U and using *spin-weighted* (spin 2) spherical harmonic functions E-mode and B-mode polarization can be derived (see Section 6.5). This is simply another more convienient formalism for characterizing the polarization of a radiation field. It is useful in cosmology because one type of initial pertubations (scalar) are known to produce only E-mode polarization, while another type (tensor) produce both E-mode and B-mode polarization. The E-mode and B-mode definitions are analogous to electric and magnetic

fields, since B-modes are curl-like and E-modes are curl-free. The final data set from the BOOMERANG 2003 flight is comprised of four power spectra: the temperature power spectrum, TT; the EE (curl-free) and BB (curl-like) polarization power spectra; and the TE cross-power spectrum. Two other cross spectra are presented, TB and EB, but are consistent with zero (as predicted by theory) and are not used in the final parameter estimation analysis.

The measured CMB angular power spectra may be compared with angular power spectra derived from cosmological models. The position and amplitude of the peaks and dips of the CMB spectra are sensitive to such parameters as the geometry of the Universe, the cosmological constant and the energy densities associated with baryons and cold dark matter [8]. Thus, the CMB angular power spectra have become invaluable observables for constraining cosmological models. The CMB temperature spectrum has been measured with high precision on large angular scales by the Wilkinson Microwave Anisotropy Probe (WMAP) experiment [35], while smaller angular scales have been probed by ground and balloon-based CMB experiments [73, 70, 21, 48, 32]. Figure 1.1 summarizes the current status of measurements of the CMB temperature angular power spectrum. These data are remarkably consistent with a ΛCDM model in which the Universe is spatially flat and is composed of radiation, baryons, neutrinos and the ever mysterious duo, cold dark matter (CDM) and dark energy (the cosmological constant, Λ).

One of the firm predictions of this *standard model* is that the CMB is intrinsically polarized. On large angular scales the polarization is sensitive to the details of the *reionization*–the era when the first stars and galaxies formed–and the curl component (B-mode) is a unique signature of tensor perturbations. On smaller angular scales the polarization spectra can verify some of the basic assumptions made in the standard model. For instance, peaks in the polarization spectra arise from the same acoustic oscillations at last scattering as those in the total temperature spectra. However, the peaks in the polarization spectra are predicted to be out of phase with the temperature peaks since the

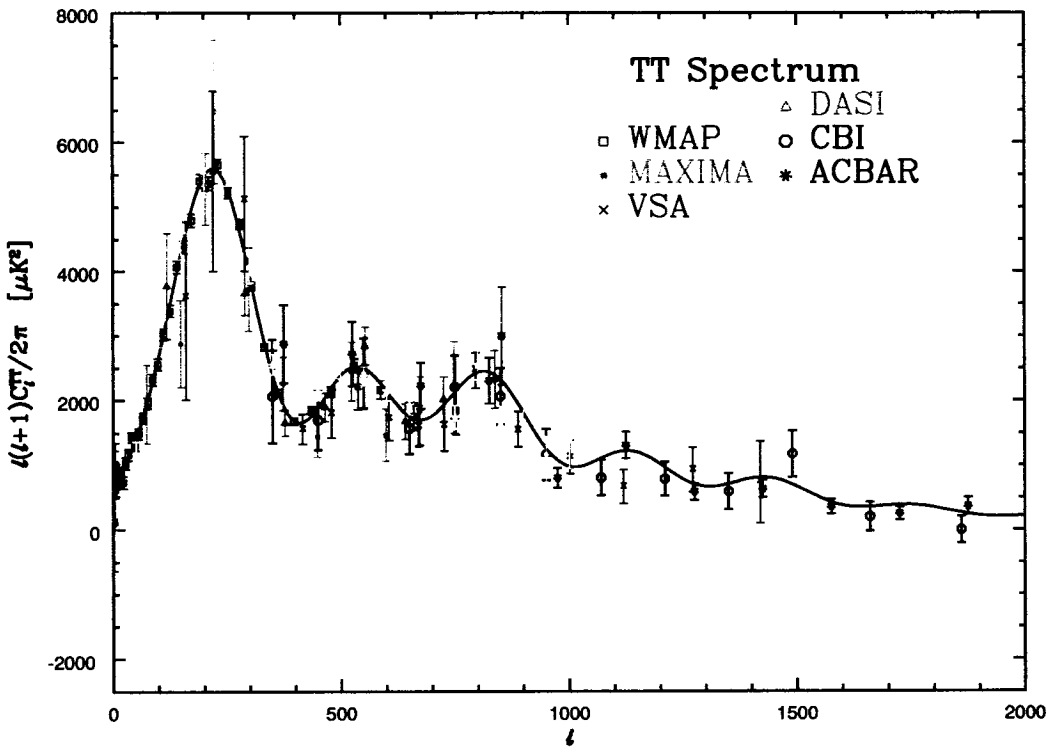

Figure 1.1: Summary of recent temperature angular power spectrum, TT, measurements from various ground (VSA, DASI, CBI, ACBAR), balloon (B98, MAXIMA) and satellite (WMAP) CMB experiments. Vertical axis is the variance in CMB temperature fluctuations. Horizontal axis is the angular wavenumber which can be related to an angular separation on the sky by $\theta \approx \pi/\ell$. Acronyms for the experiments can be found in a table at the beginning of this thesis. Model plotted (solid curve) is the previous concordance model, a best fit to WMAP(first-year)+CBI+ACBAR data from `http://lambda.gsfc.nasa.gov/product/map/`.

former are sourced by the velocity term of the primordial photon-baryon fluid as opposed to its density. Observations of the polarization power spectra, and the correlation with the total temperature spectra can therefore be used as a powerful consistency check, as well as potentially providing additional cosmological information.

The recent polarization measurements of the Degree Angular Scale Interferometer (DASI) [47], WMAP [44], the Cosmic Background Imager (CBI) [71] and the Cosmic Anisotropy Polarization Mapper (CAPMAP) [4] experiments have confirmed that

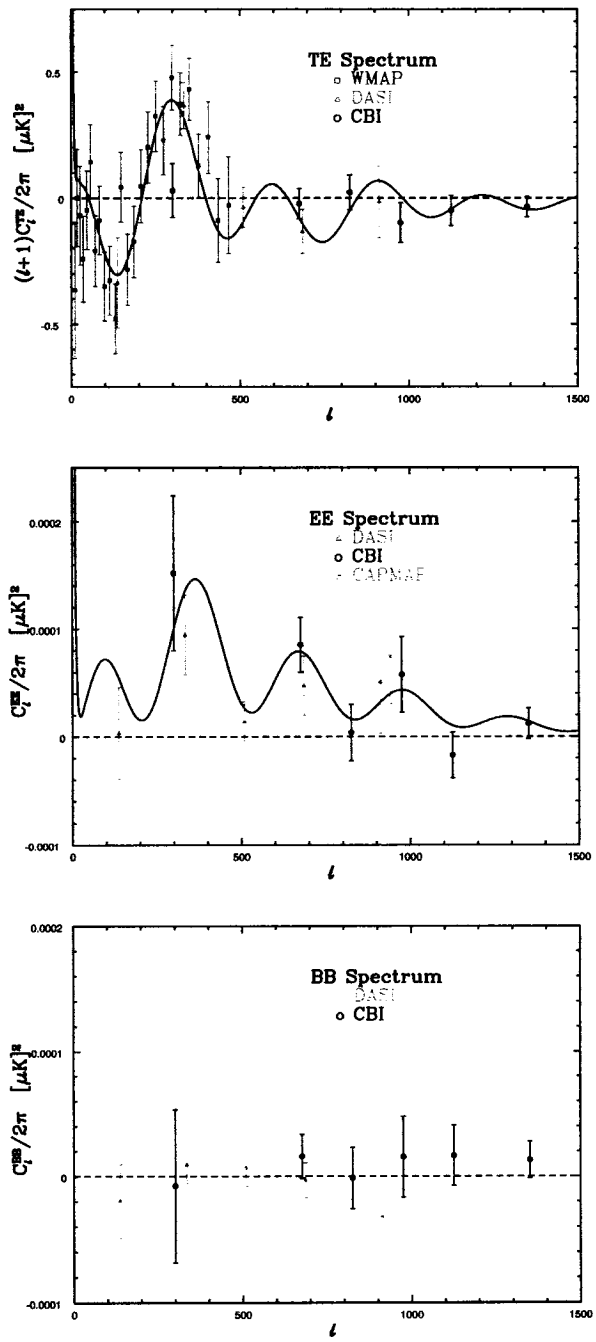

Figure 1.2: Polarization power spectrum measurements from the WMAP (satellite), DASI (ground based), CBI (ground based) and CAPMAP (ground based) experiments. Model plotted (solid curve) is the previous concordance model, a best fit to WMAP(first-year)+CBI+ACBAR data from `http://lambda.gsfc.nasa.gov/product/map/`.

the CMB is indeed polarized. Figure 1.2 illustrates the CMB polarization and cross-polarization spectral measurements of these experiements. The precision of the CMB polarization measurements are not yet at the level of the CMB temperature measurements. This is not too surprising given that the CMB polarization anisotropy is an order of magnitude smaller than the temperature anisotropy, making it a much more difficult signal to detect. The models plotted in Figure 1.2 are predominantly derived from TT data. Polarization measurements provide an independent means for testing this underlying model.

Both CBI and DASI are ground based experiments and as such are limited (in both sensitivity and observing bandwidth) by the degradation of signal by the Earth's atmosphere. On a satellite WMAP avoids this issue but the angular resolution of the experiment is limited to larger angular scales. In addition these experiments all use high electron mobility transistor (HEMT) amplifiers to detect the polarized anisotropy. At frequencies above ~100 GHz the sensitivity of HEMTs is limited by the noise temperature of the detector (see for example [80]). BOOMERANG uses sensitive bolometric detectors which allow higher frequency, thus higher resolution observations and by observing from balloon altitude (~35 km) BOOMERANG is above much of the Earth's atmosphere. Higher frequency measurements also enable the instrument to probe foregound dust. In addition BOOMERANG provides the testbed for the polarization sensitive bolometers (PSBs) to be used in the High Frequency Instrument (HFI) on the Planck Surveyor satellite. The B03 sky coverage is comprised of ~195 hours of data over ~1.8% of the sky, with an effective beam 11.5 ± 0.23 arcminutes. Instrument calibration is based on the 90 GHz and 60 GHz WMAP data and the resulting amplitude uncertainty in calibration is $\sim 2\%$.

This thesis begins with an introduction to Big Bang theory and a discussion of CMB anisotropy in Chapter 2. Chapter 3 gives an overview of the BOOMERANG instrument. My experimental contribution predominantly involved the integration and testing of the

pointing system, with considerable focus on the star camera star-tracking algorithm and testing. Chapter 4 describes in some detail the LDB environment and flight performance. Chapter 5 describes the instrument characterization derived from various tests performed before and during the flight. While (for completeness) a general overview of test results is given, I was responsible for the alignment of the instrument pointing sensors as well as, the tracking aspect of the beam measurements. Chapter 6 gives the details of the analysis pipeline, from raw data to power spectra, and presents the resulting maps and power spectra for the B03 flight. Aside from the cleaning of the bolometer data, I was involved in all aspect of the data analysis. This includes (but is not limited to): the production of the cleaned calibrated pointing fields; the overall strategy for the pointing solution; the determination of the pointing rotation matricies; the inclusion of noise correlation code for more accurate noise estimation; running and debugging of the Monte Carlo pipeline; the production of the final angular power spectra and jackknife systematic tests. Chapter 7 discusses the parameter extraction technique and tests the B03 data set against the standard model. Constraints from a multi-experiment combined CMB data set (hereafter CMBall) are also explored. Several extensions to the standard model are tested using both the CMBall data set and a combined CMBall + Large Scale Structure (LSS) data set. The resulting constraints from the CMBall+LSS data set represent the most up-to-date parameter analysis. I performed all of the analysis for Chapter 7. Finally, a summary of the results and their implications are given in Chapter 8.

Chapter 2

Big Bang Theory

This thesis tests Big Bang theory against the B03 CMB anisotropy measurements. Big Bang theory is reviewed in several cosmology texts and the contents of this chapter are not new. This chapter is intended to provide an overview of the theory involved and some of the terminology used in the cosmology today. The author found [22] and [53] particularly useful as references.

In the most generic scenario the Big Bang theory predicts that the Universe is expanding and that in the past the Universe was hotter and denser than it is now. When the Universe was less than ~300,000 years old there was a period when the scattering rates of matter and radiation exceeded the expansion rate resulting in near equilibrium conditions for the Universe's constituents. Assuming for the moment that this equilibrium applies to all scales this scenario paints a picture of a smooth, expanding Universe. This simple picture is supported by two classes of observables. The first, is the observation that distant objects in the Universe are receding at a rate proportional to their distance. This was first reported by Hubble [39], in 1929, for galaxies. The second, was the discovery of the Cosmic Microwave Background (CMB) in 1965 by Penzias and Wilson [64]. At some point after the first few hundred thousand years, the Universe expanded and cooled enough so that matter and radiation eventually decoupled. At this time, deemed the

Recombination Era, protons and electrons combined to form neutral hydrogen and the photons were allowed to travel freely throughout the Universe. The surface from which CMB photons last scattered is often referred to as the last scattering or decoupling surface. The CMB photons observed today offer a snapshot of the time of recombination. In 1991, the Far InfraRed Absolute Spectrophotometer (FIRAS) instrument on the Cosmic Background Explorer (COBE) satellite measured the near perfect blackbody spectrum of the CMB providing compelling evidence for the early equilibrium picture. As shown in Figure 2.1 the FIRAS measurement [58] and the theoretical blackbody curve are in such remarkable agreement that data points are not discernible from the model.

The simple picture of the smooth expanding Universe cannot account for the existence of galaxies and other structure that is apparent in the sky today. In order to generate the inhomogeneity observed now, the equilibrium scenario of the early Universe must be perturbed. That is, one must allow for the possibility of slight out-of-equilibrium conditions at early times in the form of tiny perturbations to the energy density (or entropy density). The fluctuations in the matter density will be the seeds from which the structures of today grow. The fluctuations in the photon density appear as anisotropies in the CMB radiation field. The deviations from the mean temperature in the primordial plasma are on the order of 10^{-5} and for polarization the deviations are an order of magnitude smaller.

Figure 2.2 illustrates a timeline for the history of the Universe. The time of recombination marks the moment when photons decoupled from the rest of matter, free-streaming throughout the Universe. Today the Universe appears to be dominated by some form of *dark energy* of which little is known. The most popular theory for the very earliest times is described by inflation, a period when the Universe expanded nearly exponentially. Inflation has the attractive feature of setting up the required initial conditions for structure formation, as well as putting regions of the Universe which are widely separated today into causal contact in the past.

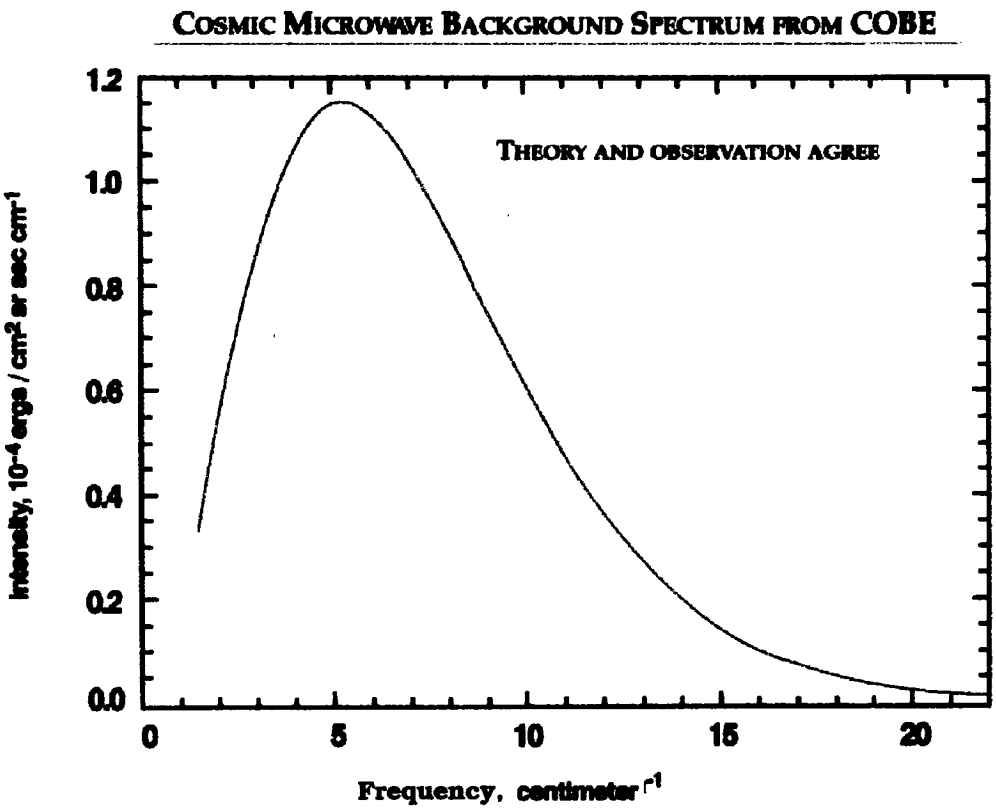

Figure 2.1: Measurement of the intensity of the CMB radiation versus frequency from the FIRAS instrument [58] on the COBE satellite. The theoretical blackbody curve is in such remarkable agreement with the data points that the two are indistinguishable. Figure taken from `http://lambda.gsfc.nasa.gov/product/cobe/firas_image.cfm`.

The cosmological models are functions of several cosmological parameters such as the age, expansion rate and content of the Universe. This chapter introduces the cosmological parameters by briefly outlining the physics that goes into the models. In Section 2.1 the theoretical framework for describing a simple picture of the smooth, expanding Universe, sometimes referred to as the "Zeroth Order Universe", is outlined, allowing introduction of many of the cosmological parameters. Section 2.2 gives a basic overview of how the initial perturbations are generated in the theory and how these perturbations evolve into the anisotropies in the CMB, described statistically by the CMB angular power spectra.

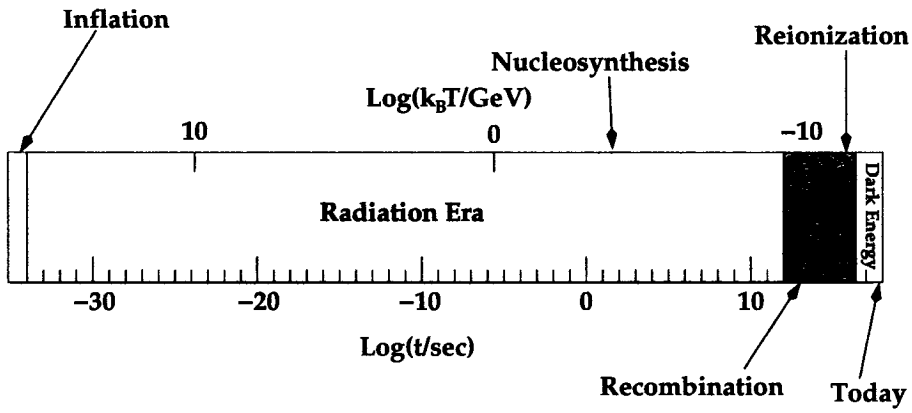

Figure 2.2: Timeline for the history of the Universe adopted from [22].

2.1 The Zeroth Order Universe

The construction of a mathematical description of the entire Universe begins with a theoretical framework for describing the expansion of four space-time dimensions. This framework is provided by the metric, which relates the coordinate distance between points on a grid to physical distance, which takes into account geometry and expansion. In its most general form the metric can be written,

$$ds^2 = \sum_{\mu,\nu=0}^{3} g_{\mu\nu} dx^\mu dx^\nu = g_{\mu\nu} dx^\mu dx^\nu \tag{2.1}$$

where in the last step the summation sign is eliminated following the convention of implicit summing over repeated indices. Also, the convention of using Greek indices (μ and ν) for space+time and Roman indices (i and j) for space only is followed. The term $g_{\mu\nu}$ is the metric tensor which characterizes the the expansion rate, the geometry and (as will be shown later) the effect of space-time perturbations.

The metric describing a homogeneous (uniform at all points in space) and isotropic (looks identical in every direction), expanding Universe is the Robertson-Walker (RW)

metric which expanded and in spherical polar coordinates takes the form[1],

$$ds^2 = -dt^2 + a(t)^2 \left(\frac{dr^2}{1 - kr^2} + r^2(d\theta^2 + \sin^2\theta \, d\phi^2) \right) \tag{2.2}$$

where $a(t)$ is the scale factor which describes the expansion of the Universe which is set to one today and decreases going into the past. The curvature parameter k characterizes the geometry of the Universe. Flat space (Euclidean geometry) has $k = 0$, while $k > 0$ corresponds to positive spatial curvature (a closed Universe) and $k < 0$ corresponds to negative spatial curvature (an open Universe).

The time variable in Equation 2.2 is often called the *comoving time* and is the time measured by an observer at rest with respect to the local matter distribution (in the language of General Relativity, a *fundamental observer*). Another time variable that is often used is the *conformal time* variable which is the total comoving time that light could have traveled since $t = 0$. The expression for this variable is,

$$\eta = \int_0^t \frac{dt'}{a(t')}. \tag{2.3}$$

Regions of space-time that are more widely separated than η are not causally connected. η is often called the comoving horizon, a concept which becomes important for motivation of inflation.

Armed with the framework defining how quantities of length, time and angle evolve in an expanding Universe, the next step is to relate the geometrical properties of space-time to the matter and energy from which the Universe is composed. This feat is realized through the application of Einstein's gravitational field equations which are,

$$G_{\mu\nu} = 8\pi G T_{\mu\nu} \tag{2.4}$$

[1]Here and throughout the speed of light $c = 1$

where G is Newton's constant. The term, $G_{\mu\nu}$ is the Einstein tensor and $T_{\mu\nu}$ is the energy-momentum tensor.

The Einstein tensor is a function of the metric tensor and its first and second derivatives. More explicitly,

$$G_{\mu\nu} \equiv R_{\mu\nu} - \frac{1}{2} g_{\mu\nu} \mathcal{R} \tag{2.5}$$

where $R_{\mu\nu}$ and $\mathcal{R}$ are the *Ricci tensor* and *Ricci scalar* respectively. The Ricci tensor is given by,

$$R_{\mu\nu} = \Gamma^{\alpha}_{\mu\nu,\alpha} - \Gamma^{\alpha}_{\mu\alpha,\nu} + \Gamma^{\alpha}_{\beta\alpha}\Gamma^{\beta}_{\mu\nu} - \Gamma^{\alpha}_{\beta\nu}\Gamma^{\beta}_{\mu\alpha} \tag{2.6}$$

where

$$\Gamma^{\mu}_{\beta\alpha} = \frac{g^{\mu\nu}}{2}\left[\frac{\partial g_{\alpha\nu}}{\partial x^{\beta}} + \frac{\partial g_{\beta\nu}}{\partial x^{\alpha}} - \frac{\partial g_{\alpha\beta}}{\partial x^{\nu}}\right] \tag{2.7}$$

are the *Christoffel symbols*. The Ricci scalar is the contraction of the Ricci tensor or $\mathcal{R} \equiv g^{\mu\nu} R_{\mu\nu}$. For the (flat) RW metric only the time-time (R_{00}) and space-space (R_{ij}) components of the Ricci tensor are non-vanishing. The time-time component of the Einstein tensor works out to $G_{00} = 3\dot{a}^2/a^2$. The result for the space-space component is $G_{ij} = (2\ddot{a}/a + \dot{a}^2/a^2) g_{ij}$.

The energy momentum tensor, $T_{\mu\nu}$, for a perfect fluid (relevant to a homogeneous and isotropic Universe of this section) is given by,

$$T^{\mu\nu} = \begin{pmatrix} -\rho & 0 & 0 & 0 \\ 0 & \mathcal{P} & 0 & 0 \\ 0 & 0 & \mathcal{P} & 0 \\ 0 & 0 & 0 & \mathcal{P} \end{pmatrix} \tag{2.8}$$

where ρ and $\mathcal{P}$ are the fluid density and pressure. The time-time component of the Einstein equations for the smooth expanding Universe reduces to the Friedman equation,

$$H^2 = \frac{8\pi G}{3}\rho - \frac{k}{a^2} \tag{2.9}$$

where $H = \dot{a}/a$ is the Hubble rate parameter. Dividing Equation 2.9 by H^2, defining the critical density $\rho_{cr} = 3H^2/8\pi G$ and rearranging yields the expression,

$$1 + \Omega_k = \Omega_{\rm tot} \tag{2.10}$$

with $\Omega_{\rm tot} = \rho/\rho_{cr}$ and $\Omega_k = 3k/(8\pi G a^2)/\rho_{cr} = \rho_k/\rho_{cr}$. Note that total density, Ω_{tot}, can include contributions from all the possible constituents of the Universe including baryonic matter (Ω_b), photons (Ω_γ), neutrinos (Ω_ν) and two components with largely unknown properties, dark matter (Ω_c) and dark energy (Ω_Λ). In short,

$$\Omega_{\rm tot} = \Omega_m + \Omega_\gamma + \Omega_\nu + \Omega_\Lambda \tag{2.11}$$

where the matter density $\Omega_m = \Omega_b + \Omega_c$.

Equation 2.9 describes the evolution of the scale factor in a Universe which is comprised of various forms of matter and energy. The evolution of the constituents of the Universe is governed by the continuity and Euler equations. In General Relativity these conservation equations require the *covariant* derivative of the energy-momentum tensor or

$$T^{\mu\nu}_{;\mu} \equiv \frac{\partial T^{\mu\nu}}{\partial x^\mu} + \Gamma^\mu_{\alpha\mu} T^{\alpha\nu} - \Gamma^\alpha_{\nu\mu} T^{\mu\alpha} = 0. \tag{2.12}$$

The $\nu = 0$ component of this equation is the equivalent of the continuity equation for a smooth, expanding Universe. This component works out to be,

$$\frac{\partial \rho}{\partial t} + 3\frac{\dot{a}}{a}(\rho + \mathcal{P}) = 0 \tag{2.13}$$

which can be written,

$$\frac{\partial \rho}{\partial t} + 3H\rho(1 + w) = 0. \tag{2.14}$$

Here $w = \mathcal{P}/\rho$ defines the equation of state for a particular constituent. For radiation

$w = 1/3$ with $\rho_r \propto a^{-4}$, and for matter $w = 0$ with $\rho_m \propto a^{-3}$. This scaling of matter or radiation density with scale factor indicates that at early times the Universe was radiation dominated but at some point matter became the dominant component. It appears, from the observational evidence of a variety of cosmological datasets (*e.g.* CMB, large scale structure and supernova data) that today $w < 0$, inconsistent with either matter or radiation domination. The dominant energy component of the Universe now is somewhat of an enigma, hence its descriptor *dark energy.* For dark energy in the form of a cosmological constant $w = -1$ and $\rho_\Lambda = constant.$ Section 7.3.2 explores the effect of alternate forms of dark energy, allowing the equation of state for the dark energy component to differ from -1.

2.2 Generating Anisotropies

Describing the initial perturbations to the equilibrium scenario and how these perturbations evolve with time is complicated by the fact that perturbing one constituent of the Universe will have an impact on another. For instance, electrons and protons are coupled through Coulomb scattering. Perturbing the electron density will have an affect on the protons and vice-versa. Similarly for the coupling of photons and electrons through Compton scattering. In addition the metric itself is also, in general, perturbed which affects all the constituents and which will in turn be affected by perturbations to all of the other constituents. The solution to describing all of these perturbed components lies in a set of linear, coupled Boltzmann-Einstein equations which (fortunately for the experimental cosmologist) can be solved using such codes as CMBFAST [74] or one of its successors, CAMB [52]. These equations are not solved here, instead an overview of some of the relevant details is given in order to introduce the remaining cosmological parameters and the dependence of the angular power spectra on these parameters. This text largely follows the derivation for the anisotropies found in Dodleson's *Modern*

Cosmology [22].

The equations which describe the evolution of the perturbations for electrons, protons, photons, dark matter and neutrinos are derived from the Boltzmann equation,

$$\frac{df(\vec{x},\vec{p},t)}{dt} = C[f(\vec{x},\vec{p},t)] \tag{2.15}$$

where f is the distribution function for a particular species (recall for example that photons in equilibrium have a Bose-Einstein distribution) which describes the probability of finding a particle in a particular region of phase space (that is with momentum, $\vec{p}$, at position $\vec{x}$, at time t). Derivatives of f depend on the metric, which must also be perturbed. $C(f)$ is the collision term which characterizes all of the interactions that the perturbed species might have with other particles.

Perturbations to the matter density are parameterized by the fractional overdensities, $\delta_c(\vec{x},t) = \delta\rho_c/\rho_c$ for the dark matter and $\delta_b(\vec{x},t) = \delta\rho_b/\rho_b$ for baryons [2]. In addition, these overdensities induce velocities in the matter which are written, $\vec{v_c}(\vec{x},t)$ for the dark matter flow and and $\vec{v_b}(\vec{x},t)$ for the flow in the baryons. It is conventional to work with these quantities in the Fourier domain, since modes in Fourier space evolve independently in the linear regime (the case considered here because perturbations are small). So the set of perturbation variables for matter are given by: $\delta_c(\mathrm{k},\eta)$, $\delta_b(\mathrm{k},\eta)$, $v_c(\mathrm{k},\eta)$ and $v_b(\mathrm{k},\eta)$[3]. In addition to switching to the Fourier domain the switch has been made from comoving to conformal time.

Because of their relativistic nature, the photons perturbation variable is slightly more complicated and is given the fractional temperature variable $\Theta(\vec{x},\hat{p},t) = \delta T/T$. In the Fourier domain the fractional temperature perturbation can be expanded in spherical

[2]Note that electrons, which are actually leptons, are conventionally included as a baryonic component in cosmology.

[3]The wavenumber is described by the variable k while the curvature parameter, defined previously, is given by the script variable k.

harmonics to give a hierarchy of moments,

$$\Theta_\ell(\mathrm{k},\eta) = \frac{1}{(-i)^\ell}\int_{-1}^{1}\frac{d\mu}{2}\mathcal{P}_\ell(\mu)\Theta(\mathrm{k},\mu,\eta) \tag{2.16}$$

where $\mu = \hat{p}\cdot\hat{\mathrm{k}}$ and $\mathcal{P}_\ell$ is a Legendre polynomial of order ℓ. So when describing perturbations in the photon distribution one must consider not only the monopole, Θ_0 (analogous to the density perturbation to matter), and the dipole, Θ_1 (equivalent to the matter velocity perturbation), perturbations but also the higher order moments such as the quadrupole, Θ_2. Similar arguments can be made for the polarization moments, $\Theta_{\ell,P}(\mathrm{k},\eta)$, as well as for the characterization of the perturbations for massless neutrinos, $\mathcal{N}_\ell(\mathrm{k},\eta)$.

Adding small perturbations to the RW metric can be parameterized by,

$$ds^2 = [g^{(0)}_{\mu\nu} + g^{(1)}_{\mu\nu}]dx^\mu dx^\nu \tag{2.17}$$

where $g^{(0)}_{\mu\nu}$ is the unperturbed RW metric tensor and $g^{(1)}_{\mu\nu}$ is the perturbed metric tensor which in the conformal Newtonian gauge[4] can be written,

$$g^{(1)}_{\mu\nu} = \begin{pmatrix} -1-2\Psi(\vec{x},t) & 0 & 0 & 0 \\ 0 & a^2(1+2\Phi(\vec{x},t)) & 0 & 0 \\ 0 & 0 & a^2(1+2\Phi(\vec{x},t)) & 0 \\ 0 & 0 & 0 & a^2(1+2\Phi(\vec{x},t)) \end{pmatrix} \tag{2.18}$$

The two functions, Ψ and Φ describe scalar perturbations to the gravitational potential and scalar curvature respectively. Again these are described in the Fourier domain as, $\Psi(\mathrm{k},\eta)$ and $\Phi(\mathrm{k},\eta)$. With all of these perturbation variables in hand (and skipping

[4] The *gauge choice* is the choice of coordinates used to describe the metric perturbations. A number of gauge choices–the synchronous gauge and the covariant gauge are two others–are possible for describing the perturbations to the metric and some of the physics is easier to describe in one gauge than in another. The final observables, however, are the same despite the choice of gauge.

all of the math) the resulting Boltzmann equations for the various constituents are:

Photon temperature and polarization

$$\dot{\Theta} + ik\mu\Theta = -\dot{\Phi} - ik\mu\Psi - \dot{\tau}\left[\Theta_0 - \Theta + \mu v_b - \frac{1}{2}\mathcal{P}_2(\mu)\Pi\right] \tag{2.19}$$

$$\Pi = \Theta_2 + \Theta_{P2} + \Theta_{P0} \tag{2.20}$$

$$\dot{\Theta}_P + ik\mu\Theta_P = -\dot{\tau}\left[-\Theta_P + \frac{1}{2}(1 - \mathcal{P}_2(\mu))\Pi\right] \tag{2.21}$$

Dark matter density and velocity

$$\dot{\delta} + ikv = -3\dot{\Phi} \tag{2.22}$$

$$\dot{v} + \frac{\dot{a}}{a}v = -ik\Psi \tag{2.23}$$

Baryon density and velocity

$$\dot{\delta}_b + ikv_b = -3\dot{\Phi} \tag{2.24}$$

$$\dot{v}_b + \frac{\dot{a}}{a}v_b = -ik\Psi + \dot{\tau}\frac{4\rho_\gamma^{(0)}}{3\rho_b^{(0)}}[v_b + 3i\Theta_1] \tag{2.25}$$

Massless neutrino distribution

$$\dot{\mathcal{N}} + ik\mu\mathcal{N} = -\dot{\Phi} - ik\mu\Psi \tag{2.26}$$

The term Π is the scalar part of the anisotropic stress tensor. More explicitly, the spatial part of the perturbed stress-energy tensor is $T_{ij} = \mathcal{P}\delta_{ij} + \mathcal{P}\Pi$. The equations which govern the evolution of the CMB anisotropies are Equation 2.19 and Equation 2.21. These are coupled to the other equations through the metric perturbations and the velocity of the

baryon fluid. Note that the optical depth, τ, has been introduced which is is given by,

$$\tau(\eta) = \int_{\eta}^{\eta_0} d\eta n_e \sigma_T a \tag{2.27}$$

where n_e is the free electron density and σ_T is the Thompson cross section. It should also be noted that the polarization strength (Equation 2.21) depends only the quadrupole, Θ_2, of the temperature perturbation and not on any of the other temperature moments. All derivatives are in terms of conformal time and all components are in the Fourier domain.

In addition to the above linear coupled equations, the matter and radiation perturbations will have an impact on the gravitational field. The perturbed Einstein equations describe this effect. The Einstein tensor, $G_{\mu\nu}$ will now depend on the first and second derivatives of the perturbed RW metric. Also required is a perturbed energy-momentum tensor,

$$T_{\mu\nu} = T^{(0)}_{\mu\nu} + \delta T_{\mu\nu} \tag{2.28}$$

The resulting time-time and spatial components of the Einstein equations give two more relationships:

Time-time perturbed Einstein equation

$$\mathrm{k}^2\Phi + 3\frac{\dot{a}}{a}\left(\dot{\Phi} - \Psi\frac{\dot{a}}{a}\right) = 4\pi G a^2 \left[\rho_m \delta_m + 4\rho_r \Theta_{r,0}\right] \tag{2.29}$$

Spatial perturbed Einstein equation

$$\mathrm{k}^2(\Phi + \Psi) = -32\pi G a^2 \rho_r \Theta_{r,2} \tag{2.30}$$

where here δ_r includes both the neutrino and photon contributions.

The above equations describe the evolution of the perturbations around the smooth, expanding Universe. However, several simplifications have been made. For instance, the

perturbations to the metric are scalar in nature when in fact there could also be a tensor perturbation, representing gravitational waves, and vector like perturbations, representing vortices (although vector modes are heavily suppressed in an expanding background and are usually not considered unless they are actively generated). In addition the neutrinos are assumed to be massless and the equation describing the perturbation of the dark energy has been neglected. The curvature, k, has also been excluded from this treatment. Regardless, this set of nine coupled linear equations provide an overview of the perturbed components of the Universe and how they are coupled to one another and to the scalar metric perturbations. Solving these equations, however, requires a set of initial conditions.

2.2.1 Initial conditions

Equations 2.19-2.26, 2.29 and 2.30 describe the evolution of nine perturbation variables. At early times it can be shown that all of these variables depend on the curvature potential, Φ. Therefore if the initial conditions for Φ are determined the initial conditions for the eight other variables follow. Taking the limit $k\eta << 1$, appropriate for the earliest times, the relationships between perturbation variables become

$$\Psi = -\Phi \tag{2.31}$$

$$\mathcal{N}_0 = \Theta_0 = \frac{\Phi}{2} \tag{2.32}$$

$$N_1 = \Theta_1 = \frac{iv_b}{3} = \frac{iv_c}{3} = \frac{-k\Phi}{6aH} \tag{2.33}$$

$$\delta_c = \delta_b = 3\Theta_0 + constant. \tag{2.34}$$

Note that all multipoles higher than the dipole are assumed to be negligible. Also, in the $k\eta << 1$ limit, the wavelengths of the perturbation modes ($\sim k^{-1}$) are all much larger than the horizon and cannot be affected by causal physics. For the constant in

Equation 2.34 describing the initial conditions for the dark matter and baryons, there are two possibilities which characterize two different modes of the primordial perturbation. These are the adiabatic initial condition and the isocurvature initial condition. In the adiabatic case, the value of the constant in Equation 2.34 is zero. This corresponds to a system which has no spatial variation in the relative number densities of different particles; otherwise put, adiabatic modes have no spatial variation in entropy. The other option has a non-zero constant term in Equation 2.34, corresponding to the isocurvature initial perturbation for which the entropy varies in space. Most conventional models have adiabatic initial conditions. In Section 7.4 models which have a sub-dominant isocurvature component (which evolves independently from the adiabatic component) are explored.

Equations 2.31-2.34 describe the initial conditions for each of the perturbation variables in terms of the curvature potential Φ. In this analysis the initial conditions for Φ are prescribed by inflation; a period at the earliest of times when the Universe went through a phase of nearly exponential expansion. While difficult to test experimentally (energy levels required to generate inflation are $\sim 10^{15} GeV$) inflation has become an appealing mechanism for describing the generation of the initial perturbations and also explains the seemingly acausal nature of the smooth CMB sky. Inflation predicts that scales which today appear outside of the comoving horizon were, before the rapid expansion of inflation, in causal contact (inside the horizon) in the past, accounting for the highly correlated temperature of the CMB field today. After inflation Fourier modes re-enter the horizon and serve as the initial conditions for the matter, radiation and metric perturbations.

In most models the inflation mechanism is driven by a single scalar field, $\phi(\vec{x}, t)$ with potential $V[\phi(\vec{x}, t)]$. In first order linear perturbation theory, this field can be decomposed into a zero-order part and a perturbed part as $\phi(\vec{x}, t) = \phi^{(0)}(t) + \delta\phi(\vec{x}, t)$. The perturbed part, $\delta\phi(\vec{x}, t)$ represents the quantum fluctuations in the scalar field before the rapid expansion which will become the initial conditions for the metric perturbations. The

approach taken is to solve for the initial power spectrum of the scalar field which is coupled to the initial power spectrum for the scalar metric perturbations which in turn can be related to the initial power spectrum for the CMB anisotropies.

Another prediction of inflation is that the quantum fluctuations and subsequent perturbations to matter and radiation are all Gaussian. This allows one to write the variance of the perturbations to the curvature potential as,

$$\langle \Phi(\vec{\mathrm{k}})\Phi^{\star}(\vec{\mathrm{k}})\rangle = (2\pi)^3 \mathcal{P}_{\mathrm{s}}(\mathrm{k})\delta^3(\vec{\mathrm{k}} - \vec{\mathrm{k}}') \tag{2.35}$$

where the $\mathcal{P}_{\mathrm{s}}$ is the power spectrum of the primordial scalar curvature perturbations to the metric. Initial conditions for the primordial curvature spectrum are described by a power law and for adiabatic, single field inflation models take the form,

$$\mathcal{P}_{\mathrm{s}} = A_{\mathrm{s}}(\mathrm{k}/\mathrm{k}_{\star})^{(n_{\mathrm{s}}-1)} \tag{2.36}$$

where the n_s is the scalar spectral spectral index and A_s is the scalar amplitude (a pivot point $\mathrm{k}_{\star} = 0.05\mathrm{Mpc}^{-1}$ is chosen).

2.2.2 The Angular Power Spectra

Given the initial conditions of the appropriate type (adiabatic or isocurvature), the next step is to evolve the system of equations from early times (in the radiation dominated era) through to the present day. The final step required to obtain the CMB angular power spectra involves the integration of the product of the initial power spectrum for the metric perturbation (scalar or tensor) and the CMB anisotropies at the present epoch. The expression for the temperature angular power spectrum may be written,

$$C_{\ell}^{TT(s)} = (4\pi)^2 \int \mathrm{k}^2 \, d\mathrm{k} \, \mathcal{P}_{\mathrm{s}}(\mathrm{k}) |\Theta_{\ell}^{(s)}(\mathrm{k}, \eta = \eta_0)|^2 \tag{2.37}$$

where η_0 denotes the present day conformal time and the superscript (s) indicates that this spectrum is derived from the scalar (as opposed to tensor) perturbations to the metric. The equivalent expression for the E-mode polarization (Section 6.5 discusses the relationship between the Stokes Q and U parameters and E and B-mode polarization) is

$$C_\ell^{EE(s)} = (4\pi)^2 \int \mathrm{k}^2 \, d\mathrm{k} \, \mathcal{P}_\mathrm{s}(\mathrm{k}) |\Theta_{P\ell}^{(s)}(\mathrm{k}, \eta = \eta_0)|^2 \tag{2.38}$$

For the cross-correlation power spectrum the expression is

$$C_\ell^{TE(s)} = (4\pi)^2 \int \mathrm{k}^2 \, d\mathrm{k} \, \mathcal{P}_\mathrm{s}(\mathrm{k}) \Theta_\ell^{(s)}(\mathrm{k}, \eta = \eta_0) \Theta_{P\ell}^{(s)}(\mathrm{k}, \eta = \eta_0). \tag{2.39}$$

Note that the scalar metric perturbations produce only E-mode polarization. The CMB B-mode (as well additional E-mode) polarization is induced by tensor perturbations. The tensor perturbation equations are not given here but in Section 7.3.2 models which include an additional tensor mode are explored.

Features in the Angular Power Spectra

On the largest scales the modes of the photon anisotropy generally evolve very little from last scattering to present day and the temperature angular power spectrum is fairly flat. This is expected since these correspond to super-horizon modes, with wavelengths larger than the horizon which causal physics cannot affect. This flat portion of the power spectrum, deemed the Sachs-Wolfe plateau, covers scales up to $\ell \sim 100$.

Analytical solutions which describe the physics of the evolution of CMB fluctuations on smaller scales have been worked out by [63, 92, 90, 10, 6] and more recently by [37]. The small scale regions of the spectra represent modes within the horizon which are effected by causal physics. In the tightly coupled limit, appropriate immediately before the recombination era, the electrons, photons and protons all behaved as a single fluid. In this limit, the photon perturbation equations can be modeled as a forced harmonic

oscillator. A driving gravitational force and opposing photon pressure cause the fluid to oscillate. These oscillations in the primordial plasma are responsible for the series of acoustic peaks in the small scales of the angular power spectra. These peaks are apparent in the solid curves in Figures 1.1 and 1.2 which represent the best fit model power spectra to the WMAP(first-year)+CBI+ACBAR data. The photon-baryon fluid density field is predicted to be out of phase with the velocity field, ultimately leading to a phase difference between the peaks in the temperature and polarization power spectra.

In general the position of the peaks can be characterized by the parameter θ [45] which is defined as

$$\theta = \frac{100\, r_s(a_\star)}{D_A(a_\star)} \tag{2.40}$$

where $r_s(a_\star)$ is the sound horizon at recombination given by,

$$r_s(a_\star) = a_\star \int_0^t \frac{c_s(t')}{a(t')} dt' \tag{2.41}$$

describing the distance traveled by a sound wave in comoving time t. The sound speed of waves in the photon-baryon fluid is given by term c_s which, for adiabatic initial conditions, is

$$c_s^2 = \frac{1}{3}(1 + 3\rho_b/4\rho_\gamma)^{-1}. \tag{2.42}$$

Finally, the $D_A(a_\star)$ term in equation 2.43 is the angular diameter distance to the decoupling surface given by,

$$D_A(a_\star) = a_\star \int_1^{a_\star} \frac{da'}{a'^2 H(a')} \tag{2.43}$$

in a flat Universe. Cosmological models which have the same value for θ will have peaks which (may) differ only in height and not in position.

The damping of peaks of the temperature anisotropy spectrum at high ℓ arises from the fact that the coupling of matter and radiation pre-recombination is imperfect. In between scatters with electrons, photons can travel a finite distance. Since the photons

provide the restoring force for the acoustic oscillations, a perturbation is damped out if the photons have time to diffuse out of it. This effect is termed *Silk Damping* and it effectively damps out the temperature fluctuations on scales of a few arcminutes.

The peaks in the E-mode polarization power spectrum are also generated by acoustic oscillations in the pre-recombination photon-baryon fluid. As mentioned earlier, these peaks are predicted to be out of phase with the temperature peaks. A radiation quadrupole arises from the velocity gradients of the photon-baryon fluid. Quadrupole radiation which scatters off of an electron will be linearly polarized. This effect is taken into account in Equation 2.21 by the inclusion of the Θ_2 term.

One final important detail is the effect of reionization on the CMB power spectra. At some point the neutral hydrogen was reionized as a result of the onset of star and galaxy formation. The impact of reionization is that the CMB photons are able to once again interact with free electrons. The effect on the temperature power spectrum is a suppression of power on the order of $\Theta e^{-\tau}$ for scales within the horizon size at the reionization era. On the other hand, the power in the E-mode polarization spectrum is augmented (at large scales) since quadrupole anisotropy present at reionization times induce additional linear polarization.

2.3 Outstanding Questions

It is only within the past ~10 years that the temperature anisotropy data have become precise enough to resolve the acoustic peaks of the ΛCDM model plotted in Figure 1.1. The goal is to achieve the same precision with polarization anisotropy measurements. A detection of the polarization peaks predicted by the temperature anisotropy data would be a powerful consistency check of the standard model. In addition using data from four (TE, EE, TT, BB) power spectra instead of just one (TT) to constrain models should reduce the uncertainties in the cosmological parameters used to describe the Universe.

The additional data from polarization power spectra can also be used to constrain modified version of the standard model. In Section 7.3 the impact of adding in turn one parameter to the baseline, six-parameter, standard model is explored and the constraints from the most up-to-date CMB and LSS data are given. More specifically this section of the thesis will address such questions as: does the current data prefer the spectral index, n_s to vary with scale?; to what degree is a non-flat geometry is allowed?; what are the upper limits on tensor modes?; is a massive neutrino dark matter component allowed?; and finally does the data what allow the dark energy to take on some form other than a cosmological constant?

Another outstanding issue is whether or not an isocurvature component can be allowed when prescribing the initial conditions of the Universe. It has been shown that a mix of adiabatic and isocurvature modes give acceptable fits to the current CMB anisotropy data [15]. The question of how much isocurvature is allowed may only be answered with the removal of parameter degeneracies broken with the addition of high precision polarization data.

While upper limits on a tensor component are given here, as of yet the B-mode polarization indicative of tensors has not been detected. This is perhaps the most pressing question in modern cosmology: Do the tensor perturbations from gravity waves exists? Answering this question is the primary (both direct and indirect) motivation for current CMB experiments. B03 addresses this question by testing new technology to measure polarization, as well as probing the level of polarized foregrounds.

Chapter 3

The Instrument

BOOMERANG is a balloon-borne telescope which measures light at 145 GHz, 245 GHz and 345 GHz. The instrument is mounted on a $\sim$5 m tall aluminum gondola and the entire flight-ready payload is $\sim$1650 kg. The gondola has an inner frame which can be driven in elevation and an outer frame which scans in azimuth. The Attitude Control System (ACS)–which includes computer controlled motors and pointing sensors–enables the in-flight azimuth scanning and elevation changes of the gondola. BOOMERANG uses bolometric detectors which are cooled to $<$0.3 K in a LHe/LN cryostat. Both the cryostat and the telescope, with its 1.3 m mirror, are mounted on the gondola's inner frame. Pointing sensors provide both coarse in-flight pointing and fine post-flight reconstructed pointing. Figures 3.1 and 3.2 show the instrument at two times during the Antarctic campaign. For the flight much of the instrument is covered with sun shielding which prevents stray light reflected from the balloon and from the Earth from entering the telescope optics. Power is provided by two large solar panel arrays that are connected to lead acid batteries. Since communication to and from the payload is very limited once the telescope is out of line of sight communication, the instrument has been designed to run autonomously. In addition to being stored on-board, the flight data are compressed and transmitted via satellite to the ground. All in-flight communication is provided by

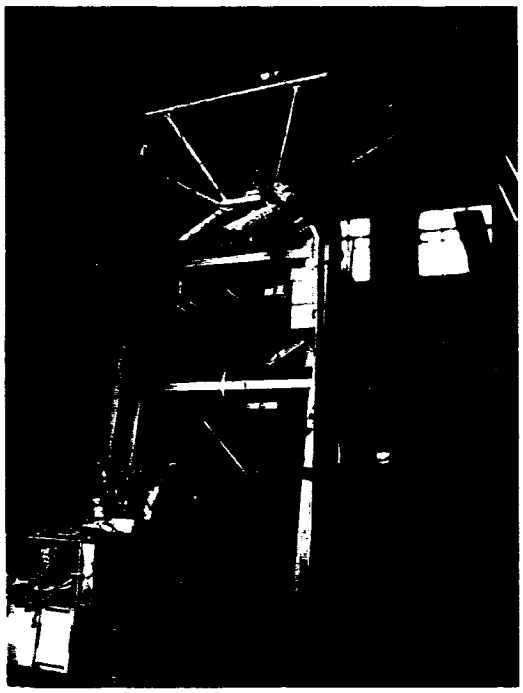

Figure 3.1: Hard at work early in the Antarctic campaign.

Figure 3.2: Flight ready payload.

the NASA National Scientific Balloon Facility (NSBF).

The entire payload is hung on steel cables from a ~800,000 cubic meter, helium-filled NSBF-provided balloon. Ideally payloads reach altitudes of 35 km which has the advantage of being above about 99.5% of the Earth's noisy atmosphere. The Antarctic vortex winds can carry an instrument in a circular path around the continent at a latitude of $\sim$ 78° south in about 10 to 24 days time. Float temperature can vary from -50° in the shade up to 50° in the sun.

This chapter gives an outline of the various components of BOOMERANG. The instrument has been described in great detail in [19, 59, 66, 41].

3.1 The Telescope

B03 is an off-axis Gregorian type telescope. The optics include three mirrors which are depicted in Figure 3.3. The optical system is designed to minimize the telescope response

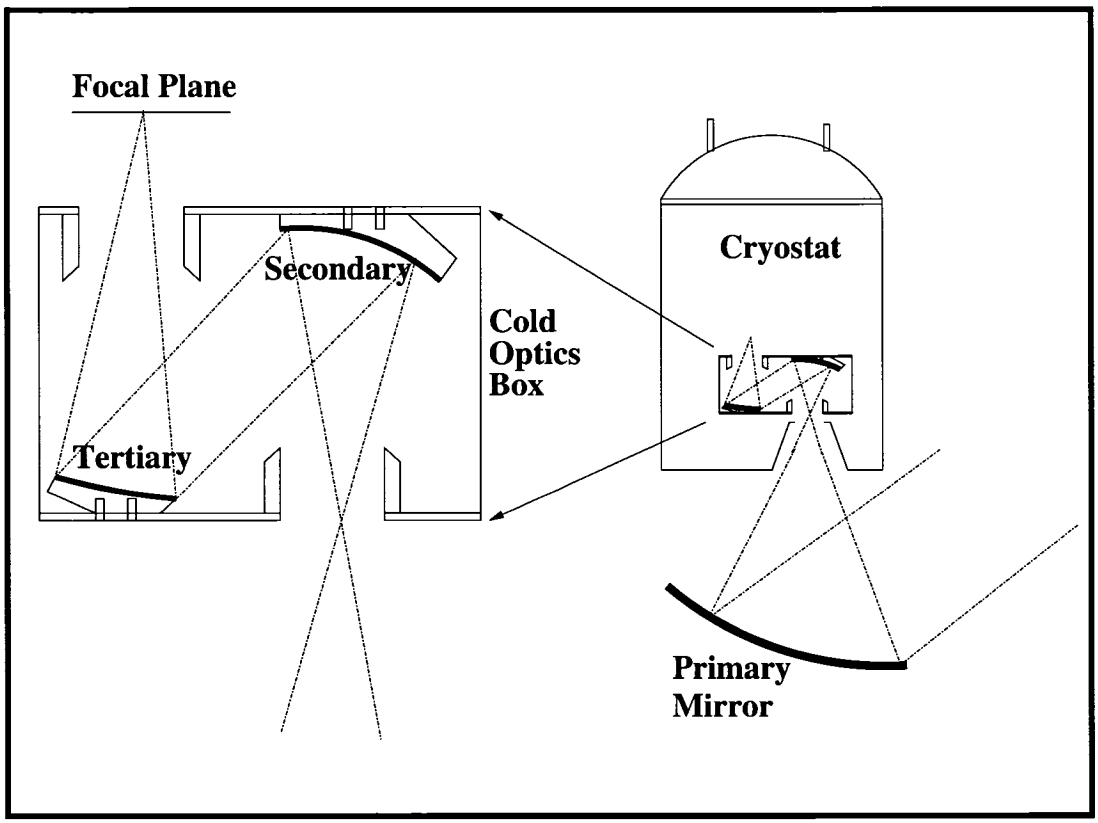

Figure 3.3: Schematic of the B03 optics. The 1.3 m primary mirror is mounted on the gondola inner frame. The secondary and tertiary mirrors are contained inside the cryostat and are kept at 1.65 K.

to sidelobes. The 1.3 m primary mirror is a 45° off-axis paraboloid with a focal length of 1280 mm. The secondary mirror is an ellipsoid and has an effective focal length of 20 cm. The tertiary is a 10 cm diameter paraboloid and has an effective focal length of 33 cm. In the shade (which is the case for most of the flight) the primary is at an average temperature of -20°C. The secondary and the tertiary are contained inside the cryostat and are kept at a temperature of about 1.65 K. By tipping the inner frame the primary can see an elevation from 33° up to 55° above the horizon.

The radiation from the sky is reflected at 45° from the primary, through the thin polypropylene window of at the bottom of the cryostat. Before hitting the secondary the light passes though a series of low pass filters which eliminate any radiation above a

frequency of 15 cm^{-1}. This filtering helps to reduce unnecessary thermal loading in the cryostat. The radiation then passes into the cold optics box where it is reflected from the secondary, onto the tertiary and then out to the focal plane. To provide stray light control the optics box is coated with an absorbing material and both of the mirrors are baffled. The tertiary is an image of the primary, and acts as a Lyot stop to reducing the amount of flare in the optical system. This is in part achieved by sizing the tertiary so that only rays from the central 50% of the primary are accepted.

3.2 The Receiver

3.2.1 The Focal Plane

After traveling through the optics box a ray of radiation passes though one of a set of feeds before arriving at the focal plane. The focal plane houses a total of sixteen detectors. The detectors are arranged in eight pixels with two detectors in each pixel. Four of the pixels measure light in a band centred at 145 GHz, while the other four two-colour pixels measure radiation in bands centered at 245 GHz and 345 GHz. All of the channels are sensitive to polarization. The choice of 145 GHz for the CMB observing frequency represents a trade-off between sensitivity to CMB radiation (relative to thermal dust foregrounds) and resolution. The 245 GHz and 345 GHz channels provide instrument sensitivity to the dust foreground.

Figure 3.4 illustrates the arrangement of the detectors in the focal plane. The smaller circles in the top row represent the 245 GHz and 345 GHz detectors which have $\sim 7'$ beams with channels sensitive to one polarization orientation. The bottom row represents the 145 GHz channels which are sensitive to two orthogonal polarizations and have larger $\sim 9.5'$ beams. The labels at the top and bottom of the figure indicate the naming convention for the detectors used in B03.

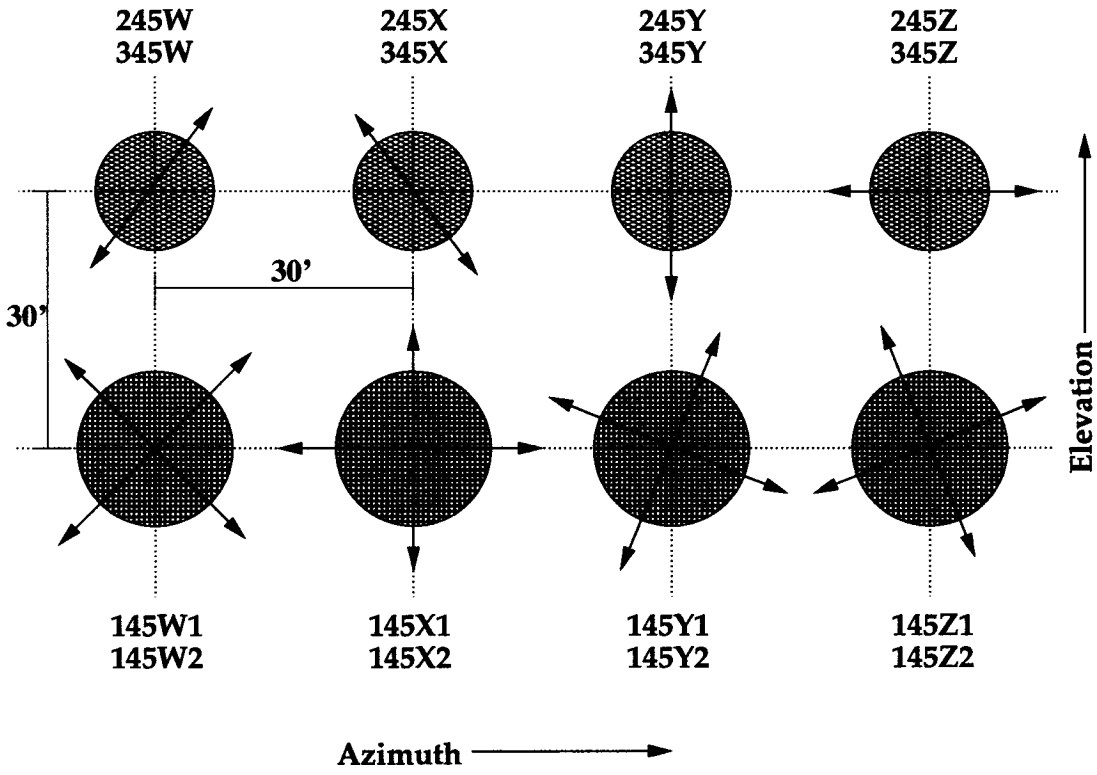

Figure 3.4: Arrangement of the B03 detectors in the focal plane. The top row represents the 245 GHz and 345 GHz detectors which are sensitive to one polarization orientation. The bottom row represents the 145 GHz channels which are sensitive to two orthogonal polarizations. Photometers (245 GHz and 345 GHz channels) have $\sim 7'$ beams and the 145 GHz PSBs have $\sim 9.5'$ beams. Labels indicate the naming convention for the detectors used in B03.

3.2.2 The Detectors and Feeds

In the past, experiments such as WMAP, CBI and DASI have used coherent receivers, employing high electron mobility transistor (HEMT) amplifiers to detect the polarized anisotropy. While this technique has the desirable feature of being inherently sensitive to polarization, above $\sim$100 GHz the sensitivity of HEMTs is limited by the noise temperature of the detector (see for example [80]). An alternate detection approach, taken by several temperature anisotropy experiments (for example both BOOMERANG and MAXIMA), has been to use incoherent bolometric receivers. Bolometers offer wideband frequency coverage and higher intrinsic sensitivity and are made polarization sensitive by placing the detectors behind a polarizing grid. This strategy is used for the 245 GHz

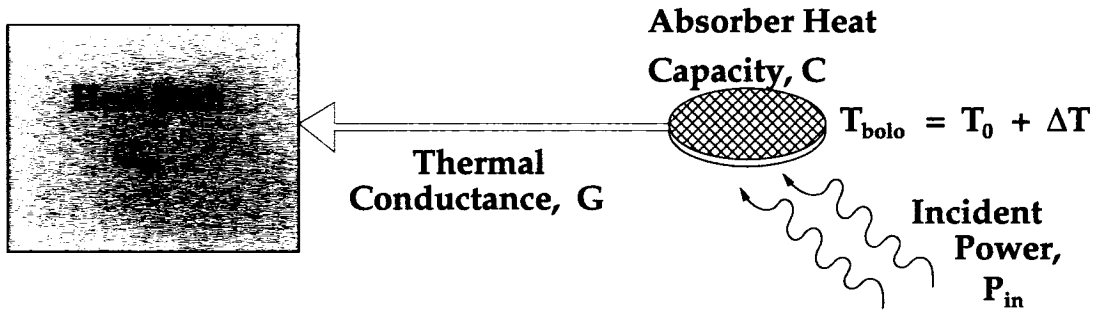

Figure 3.5: Schematic of a bolometric detector consisting of an absorbing material of heat capacity, C, and a thermometer. The absorber is connected by a weak thermal conductance, G, to a heat bath at temperature T_0. Incident radiation of power, P_{in}, causes a temperature change, ΔT, in the absorber.

and 345 GHz foreground channels for B03. In addition B03 tests for the first time Polarization Sensitive Bolometers used in the CMB 145 GHz channels, offering a test-bed for this new technology which is to be used in the High Frequency Instrument (HFI) on the Planck Surveyor satellite in 2009.

A bolometer consists of an absorbing material and a thermometer. The absorber of heat capacity, C, is connected by a weak thermal conductance, G, to a heat sink at temperature T_0. Incident radiation of power, P_{in}, hits the bolometer and is converted into thermal agitation of the detector absorber. The temperature change, ΔT, in the absorber is measured with a current biased thermistor. A schematic of bolometer operation is shown in Figure 3.5. The energy balance equation for this system is,

$$C\frac{d\Delta T}{dT} = P_{in} - G\Delta T. \tag{3.1}$$

Integration of this equation yields the response time of the bolometer to incoming radiation or the time constant given by $\tau = C/G$.

The absorber for the B03 bolometers consists of a silicon nitride micromesh grid covered in a layer of gold. A Neutron Transmutation Doped (NTD) germanium thermistor measures the temperature change and is located at the edge of the absorber. The B03

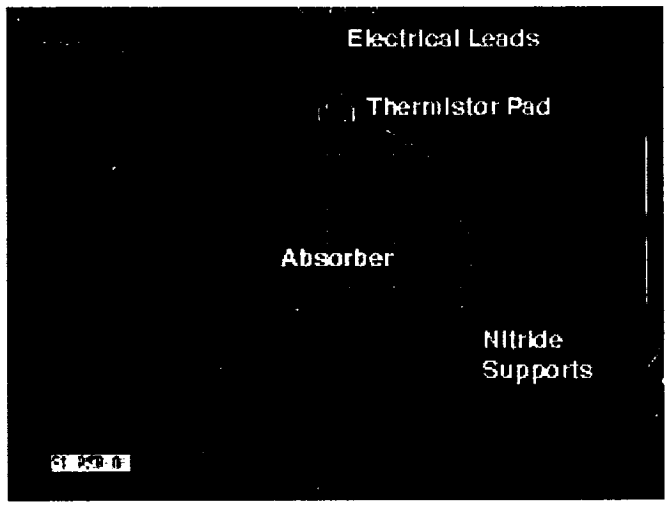

Figure 3.6: Photograph of a 145 GHz polarization sensitive bolometer (PSB). The absorbing grid is metalized only in one direction, making the detector polarization sensitive. Grid diameter is 2.6 mm. Photo courtesy of Bill Jones.

detectors consist of two types of bolometers. "Spider web" bolometers, designed to have a low cosmic ray cross section, are used in the 245 GHz and 345 GHz channels. These detectors are identical to those used in the B98 experiment. These channels are made polarization sensitive by placing a polarizing grid at the entrance of the photometer feed structure. The 145 GHz channels employ polarization sensitive bolometers (PSBs) which are made polarization sensitive by metalizing the micromesh grid in only one direction. Figure 3.6 is a picture of a PSB. The PSBs are organized in pairs which are oriented to be sensitive to orthogonal polarizations. The PSBs in a pair are separated 65 μm apart at the end of the PSB feed structure.

The detector feeds are depicted in Figures 3.7 and 3.8. The feed structures have been optimized to control sidelobes and help to reduce thermal load inside the cryostat, in addition to providing the desired frequency response. Both the photometer and PSB feeds use a back-to-back horn pair, followed by a re-concentrating feed. This configuration effectively rejects out-of-band radiation, providing an RF-tight box for the bolometers.

In the two colour photometers (245 GHz and 345 GHz channels) the radiation enters

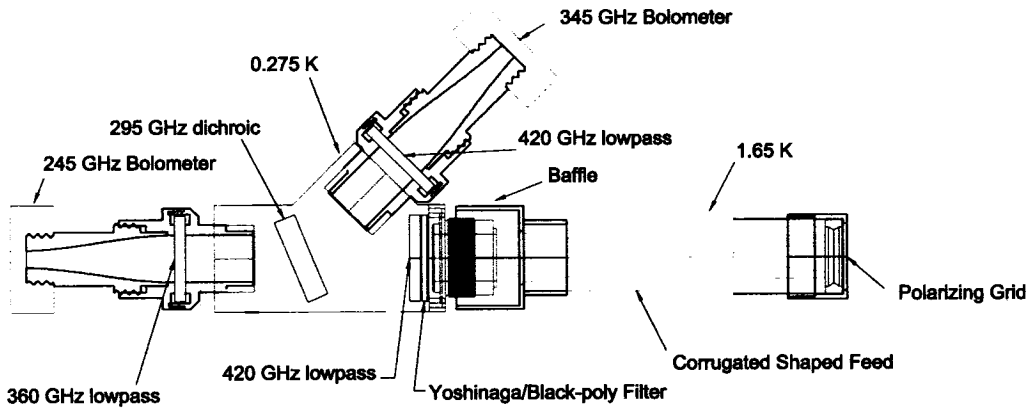

Figure 3.7: A 2-colour photometer feed structure. A polarizing grid at the feed entrance makes the 245 GHz and 345 GHz channels polarization sensitive. Feed structures are designed to optimally reject out-of-band and out-of-beam contamination.

from the right, travels through a polarizing grid into a corrugated shaped feed. After passing though a series of filters, the radiation enters the photometer body where it hits a dichroic filter which reflects radiation above 295 GHz into the 345 GHz channel and transmits the lower frequency radiation into the 245 GHz channel.

In the PSB feed, radiation enters the corrugated back-to-back horn, passes through the filter stack and then into a re-concentrating feed and onto the PSB pair, which measures simultaneously orthogonal polarization components.

3.2.3 Detector Readout Electronics

A schematic of the bolometer readout electronics is shown in Figure 3.9. The bolometers are biased with an AC current at 140 GHz. The AC bias modulation serves to move the signal information to a frequencies well above the 1/f knee of the bolometers and electronics. Each bolometer signal is buffered by a pair of low noise JFETS inside the cryostat which reduce signal impedance and provide gain to the bolometer signal power. The JFET output is then amplified in a pre-amplifier and subsequently bandpass filtered to remove noise outside the signal bandwidth. The signal is demodulated in the lock-

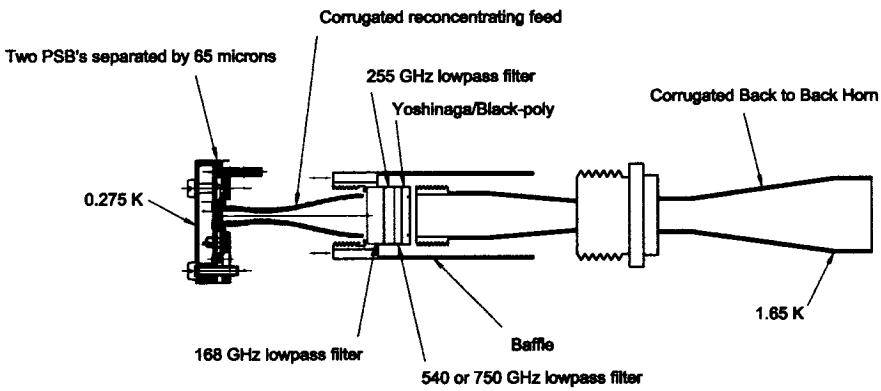

Figure 3.8: A 145 GHz PSB feed structure. Each PSB channel is sensitive to two orthogonal polarization modes. Feeds are optimally designed to preserve the polarization of the incoming radiation.

in amplifier by multiplication with the bias reference. The demodulated signal travels through a 10 Hz low pass filter, followed by a 10 mHz high pass filter before being digitized by a 16 bit analog-to-digital converter in the DAS.

3.3 The Cryostat

The B03 cryogenics system can keep detectors at < 0.3 K for up to two weeks. A schematic of the cyrostat is shown in Figure 3.10. It consists of toroidal shaped tanks suspended inside one another by Kevlar cords. Kevlar has the advantage of low thermal conductivity while providing mechanical support. The outermost tank is filled with 65 litres of nitrogen. To reduce the thermal input from the 300 K environment the nitrogen tank is wrapped in 30 layers of superinsulation aluminized mylar. Suspended inside the nitrogen tank is a 60 litre liquid ^{4}He tank. Radiative thermal loading on the ^{4}He tank is reduced by way of a vapour cooled shield. This copper shield surrounds the helium tank and is cooled by the cold gas which has evaporated from the ^{4}He tank.

The cold optics box and the focal plane are contained inside the ^{4}He tank. At the

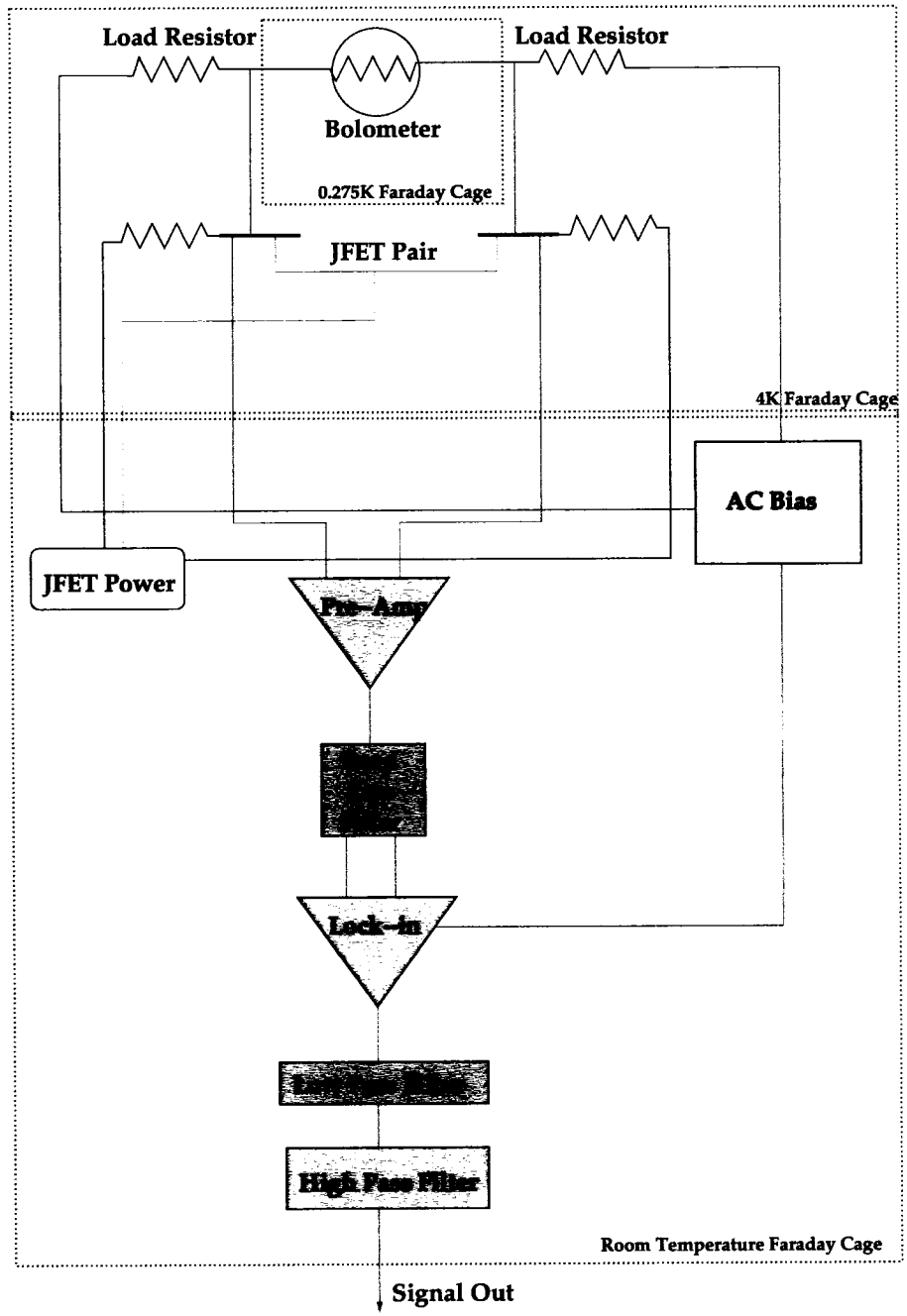

Figure 3.9: A schematic of the bolometer readout electronics. The bolometers are biased with 140 GHz AC current. The bolometer signal is buffered by a pair of low noise JFETS. The JFET output is amplified in the pre-amplifier and then bandpass filtered. The lock-in demodulates the signal which then travels through a 10 Hz low-pass filter, followed by a 10 mHz high-pass filter.

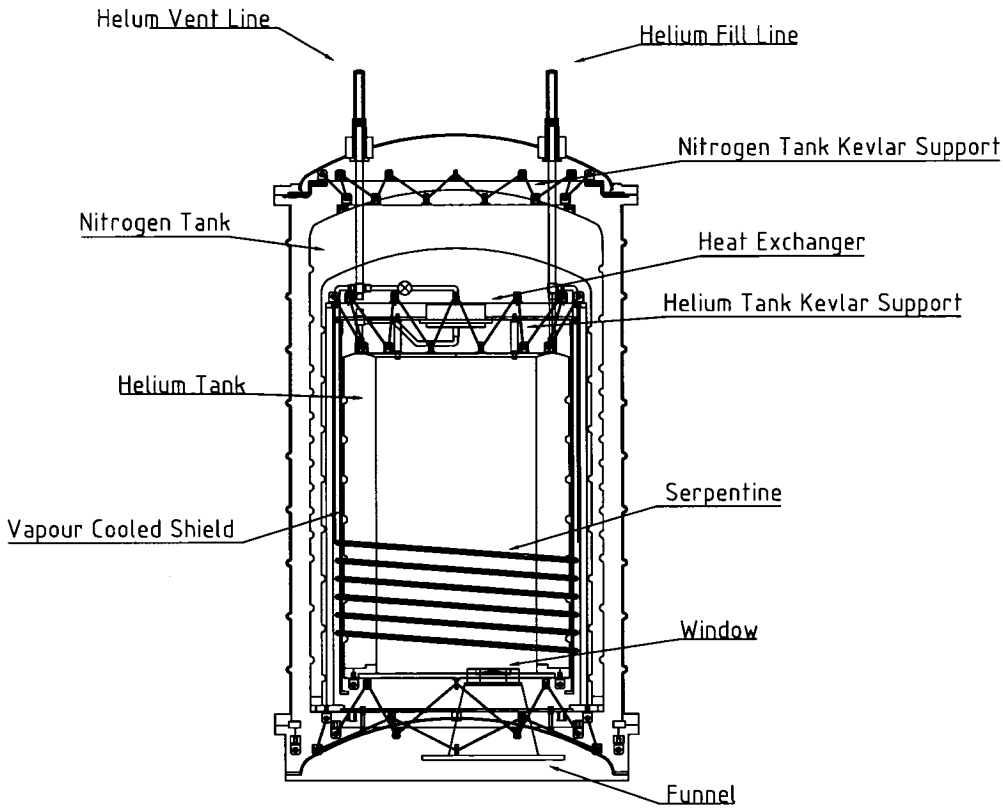

Figure 3.10: A schematic of the BOOMERANG cryostat. The B03 cryogenics system can keep detectors at < 0.3 K for up to two weeks. Toroidal shaped tanks are suspended inside one another by Kevlar cords. The outermost tank is filled with 65 litres of nitrogen. Suspended inside the nitrogen tank is a 60 litre liquid ^{4}He tank. Figure courtesy of Francesco Piacentini.

focal plane the detectors are kept at sub-Kelvin temperatures by a ^{3}He refrigerator. The refrigerator holds $\sim$ 48 litres STP of ^{3}He and is a closed-cycle, sorption pumped system. The cool down begins with the addition of the liquids to the cryostat which lower the temperature of the focal plane to about 4 K. Pumping on the ^{4}He bath lowers the temperature to 1.65 K. At float, the bath is opened to space. A slow pump down ($\sim$14 hours) is required to prevent the production of thermo-acoustical oscillations in the system. The next step in the cooling process is the heating of the cryopump to 40 K which expels the ^{3}He which subsequently condenses in the evaporator. Once all of the

^{3}He gas has been collected in the evaporator a mechanical heat switch is closed which connects the cryopump to 1.65 K. Finally, the cryopump cooling causes pumping on the liquid ^{3}He in the evaporator which reduces the evaporator temperature to the desired 0.275 K. The cryogenics system for BOOMERANG was designed and built in Italy and is described in greater detail in [55] and [56].

3.4 The Attitude Control System

The Attitude Control System (ACS) consists of three motors, an elevation encoder, three gyroscopes, a differential Global Positioning System (GPS), a Pointed-Sun Sensor(PSS), a Fixed Sun Sensor (FSS), a Star Camera (SC) and six computers. Two of the computers, a pair of redundant 386 CPUs, make up the Flight Logic Computer (FLC) which controls in-flight pointing. Two others, contained in the Pressure Vessel (PV), are responsible for data storage. In addition to data storage, one of the PV computers also runs the program which controls the SC motion. Finally, two (Z80) computers are relegated to the readout (and control for case of the PSS) of the sun sensors.

The task of the ACS is two-fold. First, it must provide the coarse in-flight pointing. While the overall trajectory is determined by the Antarctic winds, the gondola azimuth and inner frame elevation are controlled in-flight by the ACS. The second task of the ACS is to record data which will be used post-flight to reconstruct the fine pointing. One of the greatest challenges facing balloon-borne cosmology experiments is the attainment of the precise pointing required by the experiment scientific goals.

The coarse in-flight pointing ($\sim$several arcminutes) controlled by the FLC is provided by the combined efforts of three motors, an elevation encoder, the azimuth gyroscope, the FSS and the GPS. Azimuth scanning is facilitated by two torque motors and the speed of the scan is regulated by azimuth gyroscope feedback. The azimuth motors apply torque to a large flywheel in one direction and to the flight train in the opposite direction. A

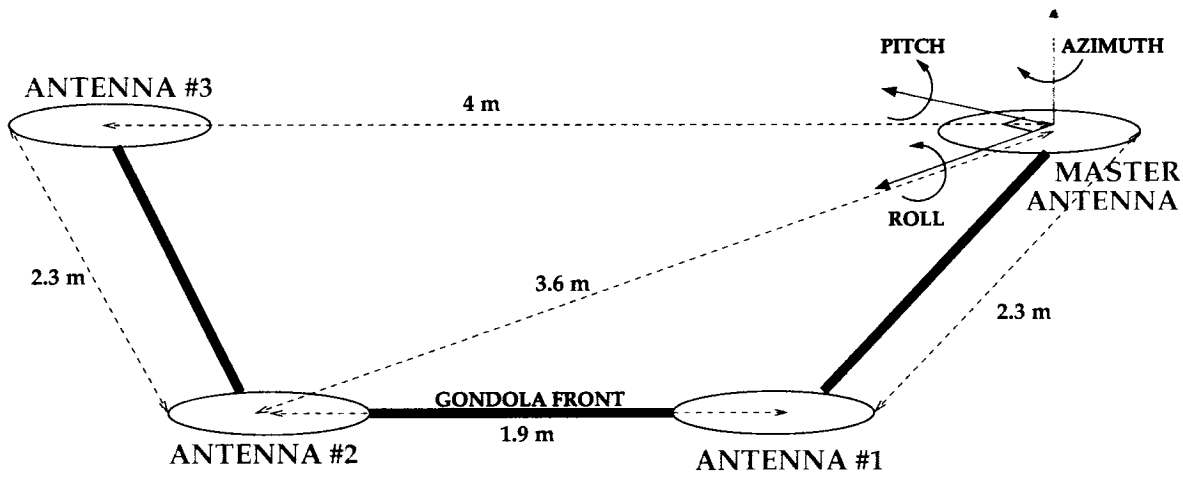

Figure 3.11: A schematic of the GPS array indicating the orientation of the array axes with respect to the front of the gondola. Accuracy of the attitude information is inversely proportional to antenna separation (with a recommended maximum baseline length of 4 m).

more complete description of the azimuth motor control is given in [14]. Absolute azimuth position information is determined by either the GPS or the FSS. Telescope elevation changes are provided by the elevation motor and encoder which enable steering of the inner frame through a range of 33 to 55 degrees above the horizon. Both azimuth and elevation motors are controlled using PWM (pulse width modulated) controlled current driven by software Proportional-Integral-Derivative (PID) control algorithms in the FLC.

Fine reconstructed pointing is derived from the combination of data from the SC, PSS, FSS as well the gyroscopes and the GPS. The azimuth, pitch and roll gyroscopes are *KVH E-Core 2030* series which use fiber optic technology to measure the phase difference in a light source which is split and fed into opposite paths around a sensing coil. If the coil is rotating (the gondola is rotating around one of the azimuth, pitch or roll axes) the phase difference in the two paths is sensed as an amplitude change in the recombined light, which in turn is proportional to the velocity around that particular axis of rotation. The gyroscopes have an angle random walk or noise level of 5 degrees/hour/$Hz^{1/2}$. The gyroscopes are anti-alias filtered by Bessel low pass filters each with a 5 Hz cutoff.

The differential *TANS Vector* GPS attitude determination system consists of four

antennas and a receiver processing unit. It provides azimuth, pitch, roll, as well as velocity and time data. Figure 3.11 illustrates the GPS array highlighting antenna distances and the locations of the azimuth, pitch and roll axes. The accuracy of the azimuth, pitch and roll data is roughly ~6 arcminutes which is too coarse to be used in the reconstructed-pointing solution. However, the GPS-supplied east, north and up velocity data, with an accuracy of 0.1 m/s, can be used to derive the gondola pitch and roll. In the stable LDB environment the gondola can be modeled as a pendulum. The arcsine of the acceleration of the gondola (determined from the derivative of the GPS velocity fields) is proportional to the pitch or roll. The resulting derived pitch and roll are accurate to about $\sim$ 2 arcminutes.

The FSS provides sun azimuth, while the PSS provides both sun azimuth and elevation. The sun sensors are described in greater detail in [66].

3.4.1 The Star Camera

The simplest approach to acquiring star positions is to use a fixed bore-sight sensor. For B03 image smearing while scanning at rates up to 1 degree/sec would be too high to for this approach to work. The alternate strategy is to acquire star position data with a camera on a pointable mount.

The B03 star camera shown in Figure 3.12 consists of a video, COHU brand (4920 series), monochrome, Peltier cooled, CCD camera equipped with a Maksutov 500 mm focal length, f/5.6 telephoto lens. This setup yields approximately 4 arcsecond per pixel resolution and ~30 arcminute field of view. Affixed to the lens is a seven ring baffle which is covered in aluminized mylar. The interior of the baffle is painted with black water-based theater paint to prevent any light scatter from entering the SC optics. For the flight a 715 nm high pass filter was installed and the camera gain was set at a minimum in order to optimize star recognition and minimize the risk of saturation from the glow of the daytime Antarctic sky.

Figure 3.12: Flight ready star camera. The stepper motor drivers and encoders are covered in foam in an effort to prevent freezing at float altitude.

The star camera is fixed on a yoke-type equatorial mount. Motion control of the two-axis system (arbitrarily named the ρ and θ axes) is provided by two Applied Motion Products high torque stepper motors. An encoder on each axis provides position feedback for controlling the motion of the mount. Two clock cards (one for each axis) provide pulses to the stepper motors. The stepper motors move one step per pulse. Speed is changed by altering the pulse frequency. Since B03 is a scanning telescope additional feedback from the azimuth gyroscope is required so that the star camera can remain locked onto a star

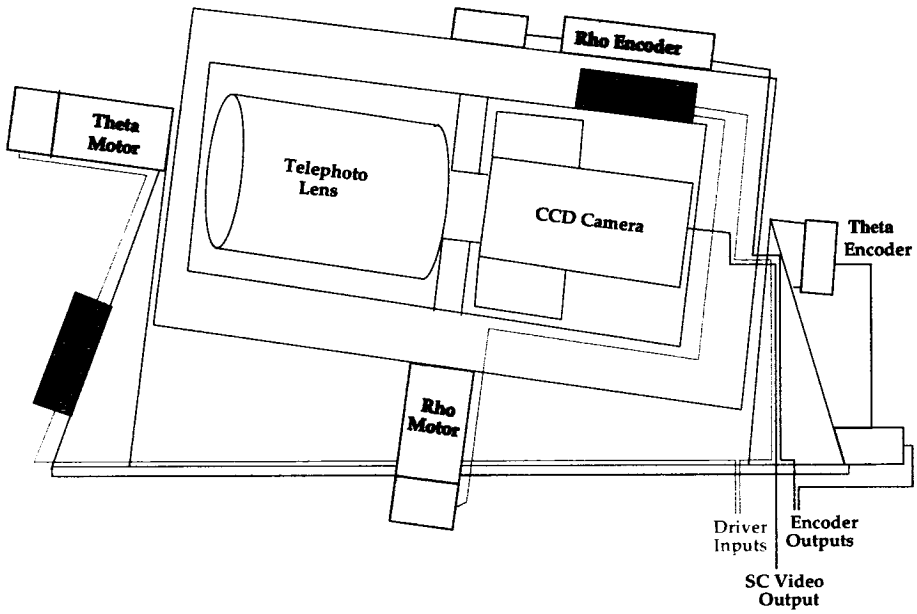

Figure 3.13: Schematic of star camera hardware and electronics. Video signal and encoder readouts are output to one of the PV computers. The motor driver commands are returned to the SC.

while the telescope is scanning. Video images are captured with a MATROX METEOR frame grabber at a rate of 10 Hz. Figure 3.13 is a schematic of the SC electronics and hardware.

Outputs from the SC are fed into the flight computer which is contained in a pressurized vessel (PV). In addition to data storage, this computer also runs the program which controls the SC motion. The algorithm inputs are video images, encoder readouts and ACS data and the output is the motor position control. The first step in the star capture algorithm is checking the mode of the telescope (ascent, scanning, etc.). Next the time, latitude and longitude of the payload are obtained. This is followed by a search of a list of stars to determine which is the the brightest, optimally positioned (in the scan centre) star to grab. The star camera then scans over to the vicinity of the star location and rasters until the desired star is in the field of view. The star camera remains locked onto the star until the telescope mode changes or the star goes out of range. Figure 3.14 outlines the logic of SC star tracking program.

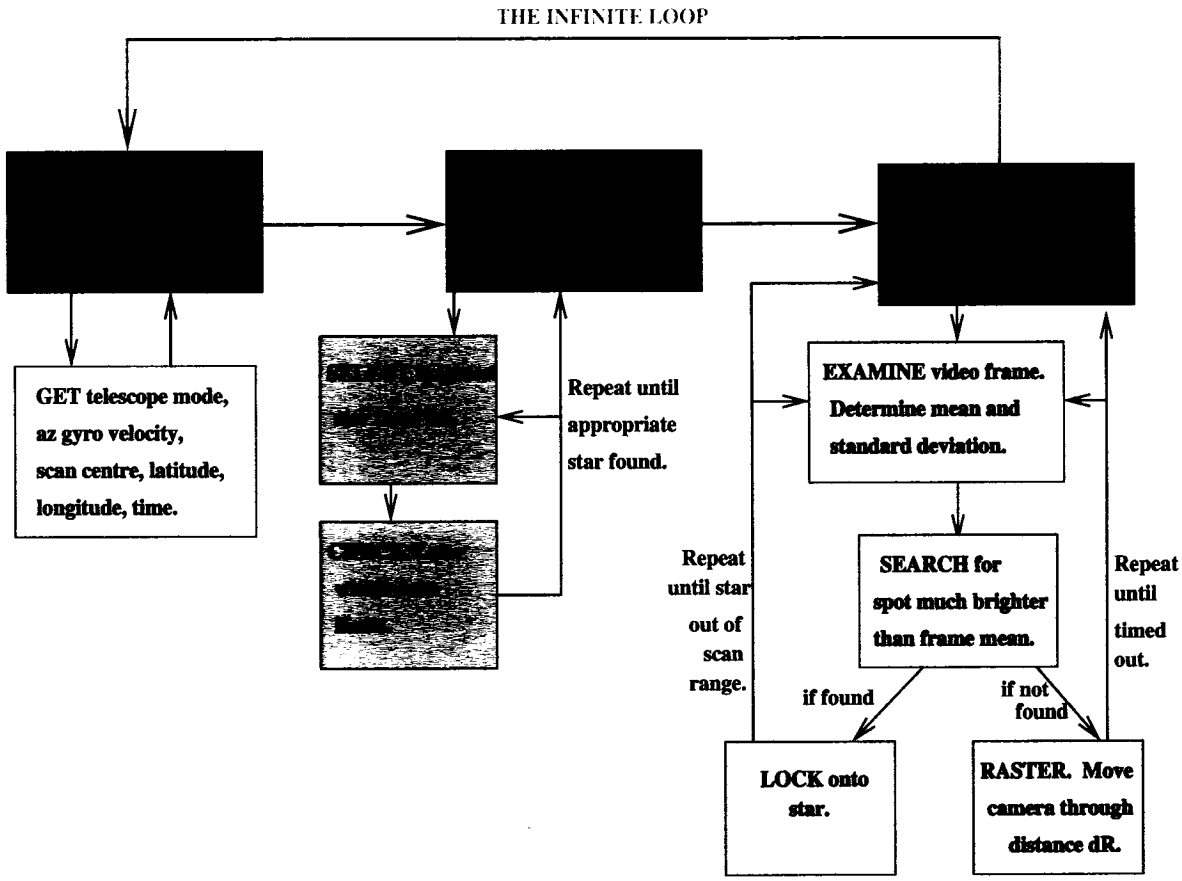

Figure 3.14: Block diagram of the SC star capture algorithm.

Chapter 4

The LDB Flight

After over two months of instrument integration and testing B03 was launched on January 6^{th}, 2003 from McMurdo Station, Antarctica. The flight path is depicted in Figure 4.1. The B03 flight suffered from a daily loss of altitude. Despite dropping 171 kg of ballast, the payload altitude continued to drop throughout the flight. The path was further complicated by the lower altitude winds which kept the balloon in the same spot for nearly 5 days. After 15 days in the air the flight was terminated on January 21^{st}. The payload landed near the Japanese base, Dome Fuji, located at 3810 m elevation on the Antarctic plateau. Thankfully, in spite of the rather inconvenient final location of the telescope, the data vessel was obtained within a week. The remainder of the instrument was salvaged the following year. This chapter outlines the environment at float, as well as telescope performance during the fight.

4.1 Altitude and Temperature

The altitude of the payload over the flight is show in Figure 4.2. The payload dropped in altitude by about 2 km each day, as a results of a suspected leak in the balloon. Generally speaking, the lower altitude environment is less stable, and can complicate telescope systematics. The loading on the bolometric detectors increases as the payload

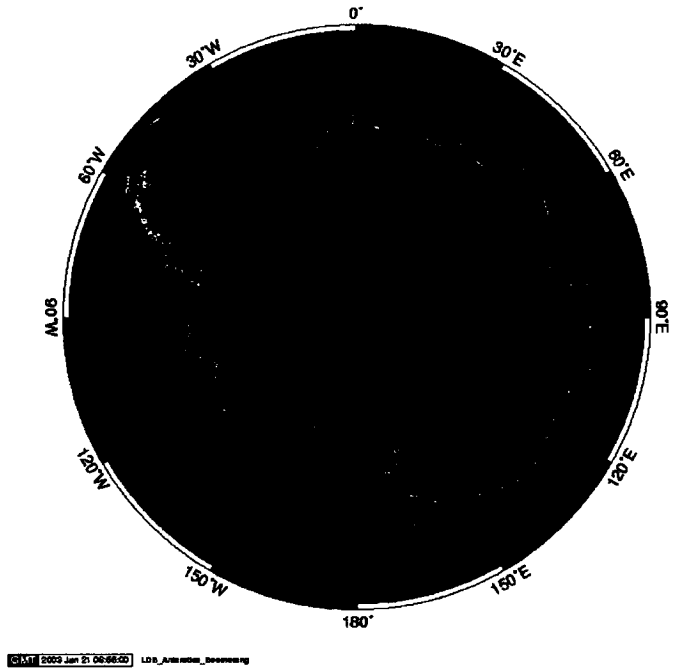

Figure 4.1: The B03 flight path. The flight began on January 6^{th}, 2003 and was terminated 15 days later on January 21^{st}. Late in the flight the payload moved very little as a result of low altitude winds. Figure provided by NSBF.

drops further into the Earth's atmosphere. In addition at lower altitude the ambient temperature decreases which has an effect on sensor performance.

Figure 4.3 illustrates the temperature of various sensors and locations on the gondola over duration the flight. The diurnal temperature cycle, as well as the long term temperature decrease with altitude loss are both apparent. Temperature data from two of the temperature sensors versus altitude are shown in Figure 4.4. The scoop temperature sensor was located on the front of the instrument and is a good indicator of the ambient temperature in the shade at float. The FSS temperature sensor was fixed to the sun-facing FSS. Averages for both altitude and temperature over daily periods where the sun is above (or below) an elevation threshold are given in Figure 4.4. Errors represent the standard deviation of the mean temperature (or mean altitude) for a given sun elevation

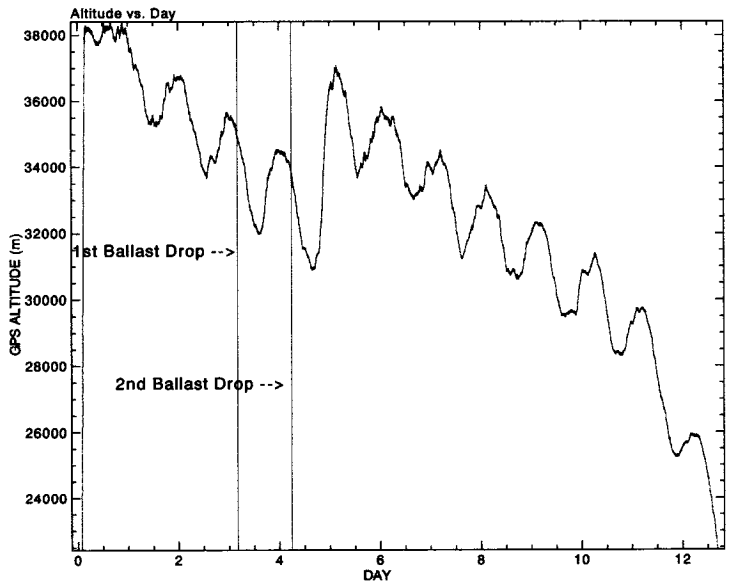

Figure 4.2: Gondola altitude during the flight. Sand ballast was dropped twice during the flight in an effort to increase payload altitude.

bin. Results of Figure 4.4 indicate that the temperature, for a given sun elevation and gondola location, increases by $\sim 5°C$ over the 26 km to 37 km altitude range. The back (sun facing side) of the gondola ranged from 19°C up to about 52°C. The shaded side of the gondola ranged from $-50°C$ up to a maximum of $-18°C$.

4.2 Ballast Drop

Sand ballast was dropped twice during the flight in an attempt to ameliorate the altitude loss problem. The first ballast drop of ~ 35 kg was performed on the fourth day of the flight. Figure 4.2 shows that this first ballast drop had negligible impact on the payload altitude. Thus, on the fifth day of the flight the remaining ballast, ~ 136 kg, was released. As can be seen in Figure 4.2 the second ballast drop had the desired effect of increasing the payload altitude. However, dropping this much ballast upset the balance of the gondola, causing the gondola to tilt, primarily in pitch. This tilt is evident in Figure 4.5

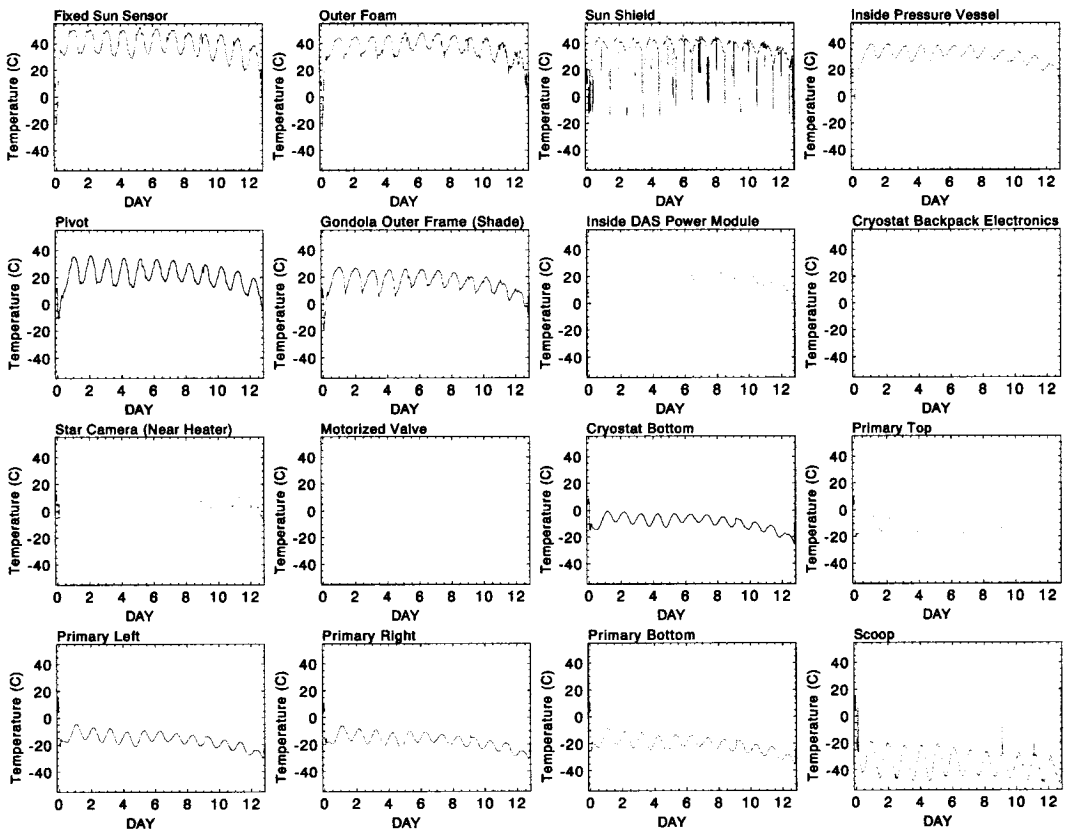

Figure 4.3: The temperature at various locations on the gondola during the flight. The diurnal temperature cycle and the long-term temperature decrease (with altitude loss) are apparent.

which shows the gondola pitch as measured by the star camera both before and after the ballast drop. The horizontal lines indicate the mean pitch which changes by roughly 0.1 degrees after the ballast is dropped.

4.3 Sky Brightness

During the flight the SC captured images which were stored to disk on the PV flight computer. These images are used in the determination of the sky brightness at float

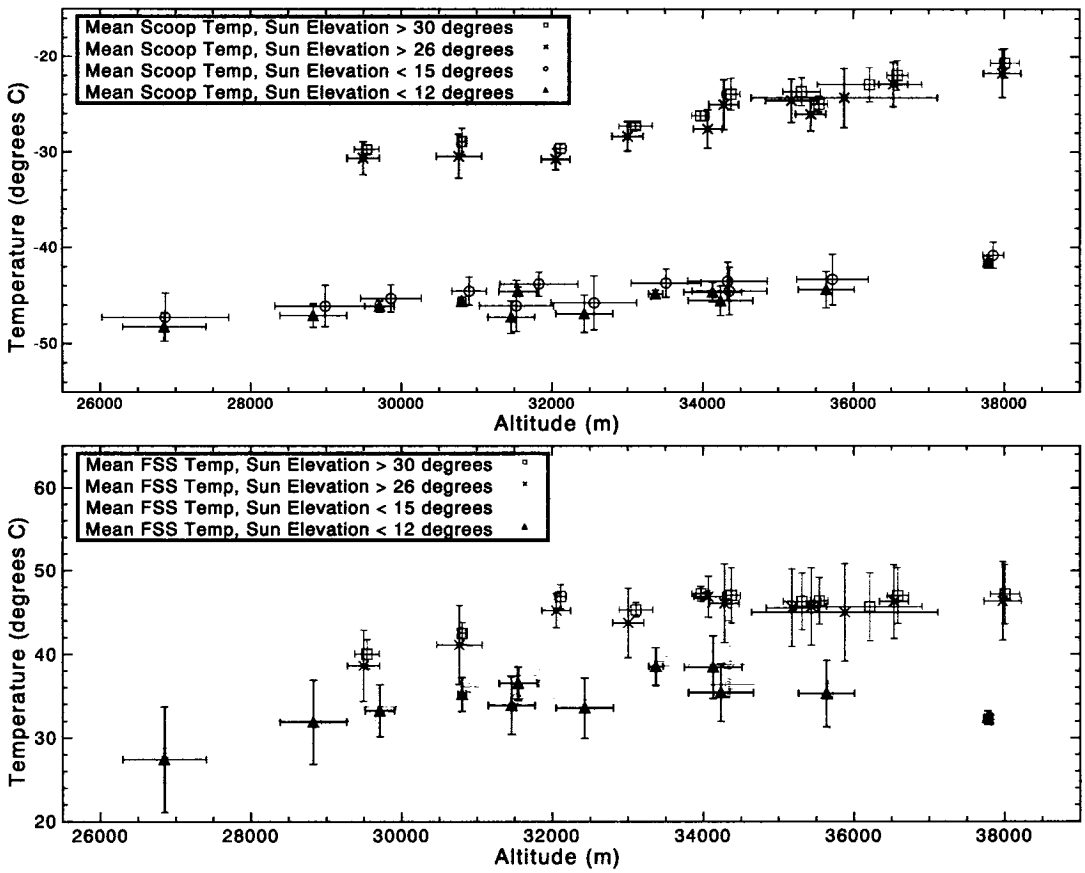

Figure 4.4: Temperature data from two of the temperature sensors versus altitude. The scoop temperature sensor was in the shade at float and the FSS temperature sensor was fixed to the sun-facing FSS. Averages for both altitude and temperature over daily periods where the sun is above (or below) an elevation threshold are given. Errors represent the standard deviation of the mean temperature (or mean altitude) for a given sun elevation bin.

altitude in the Antarctic daytime sky. This can be a useful figure when considering future pointing sensor strategies. In order to determine the sky brightness the SC was calibrated using images of Sirius. Additional information required includes the SC field of view and the integrated sensor response. The equation below describes the sky brightness which (for the anti-sun facing SC) depends predominantly on altitude but is also slightly

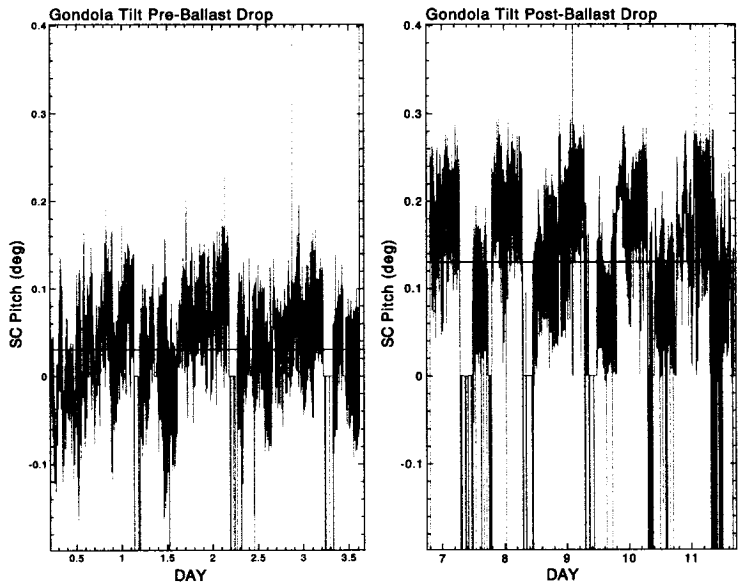

Figure 4.5: The gondola pitch before and after the ballast drop. The horizontal lines indicate the mean pitch which changes by roughly 0.1 degrees after the ballast is dropped.

correlated with sun elevation and SC line-of-sight.

$$R = \frac{[\frac{\int t(\lambda) S_{Sirius}(\lambda) d\lambda}{C_{Sirius}}] C_{Background}}{\Omega \int t(\lambda) d\lambda}$$

Here S_{Sirius} is the flux distribution of Sirius derived from data in [20], C_{Sirius} is the intensity of Sirius in CCD counts, integrated over the image, and $C_{Background}$ is the intensity of the sky background in CCD counts, integrated over the image. The function $t(\lambda)$ is the CCD sensor spectral response, taken from the COHU camera manual, and Ω is the camera field of view in steradians. The resulting values for sky brightness for various altitudes are shown in Figure 4.6. The error bars are dominated by the uncertainty in the camera noise offset which was not well determined before the flight. Figure 4.6 also shows theoretical sky brightness values generated by the MODTRAN [5] software model which is in good agreement with the data. The range for the sky brightness data is from

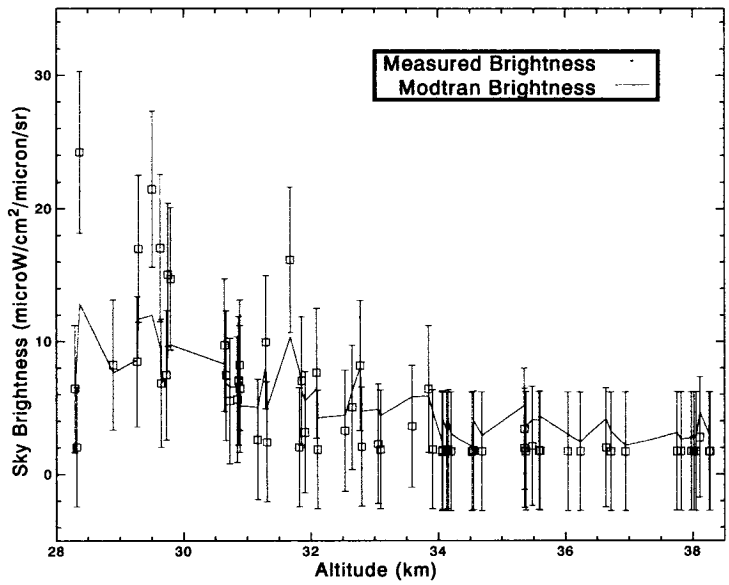

Figure 4.6: Sky brightness versus altitude. The error bars are dominated by the uncertainty in the camera noise offset. Theoretical sky brightness (solid curve) is generated by the MODTRAN [5] software model and is in good agreement with the data.

$\sim 2\ \mu W/cm^2/\mu m/sr$ at roughly 38 km altitude, up to $\sim 24\ \mu W/cm^2/\mu m/sr$ at 28 km.

Figure 4.7 show the sky brightness derived from background data taken during ascent. At low altitude the agreement between the data and the MODTRAN model is poor. This is likely due to the close proximity of Mount Erebus during ascent. Mount Erebus is the largest and most active volcano in Antarctica. As such, it is a major source of atmospheric aerosols and gases [77]. In fact, Erebus is one of the top ten known CO2 producing volcanos in the world [89]. Two model brightness profiles are show in Figure 4.7. The MODTRAN parameter IVULCN controls the choice of aerosol profile and the type of extinction for the stratospheric aerosols. Setting the variable IVULCN = 0 corresponds to the nominal background stratospheric vertical distribution and extinction model. The resulting nominal MODTRAN brightness curve is lower than the curve derived from the ascent data. Setting the variable IVULCN = 6, corresponds to changing the aerosol profile to *moderate volcanic*. This curve is in marginally better agreement with the data.

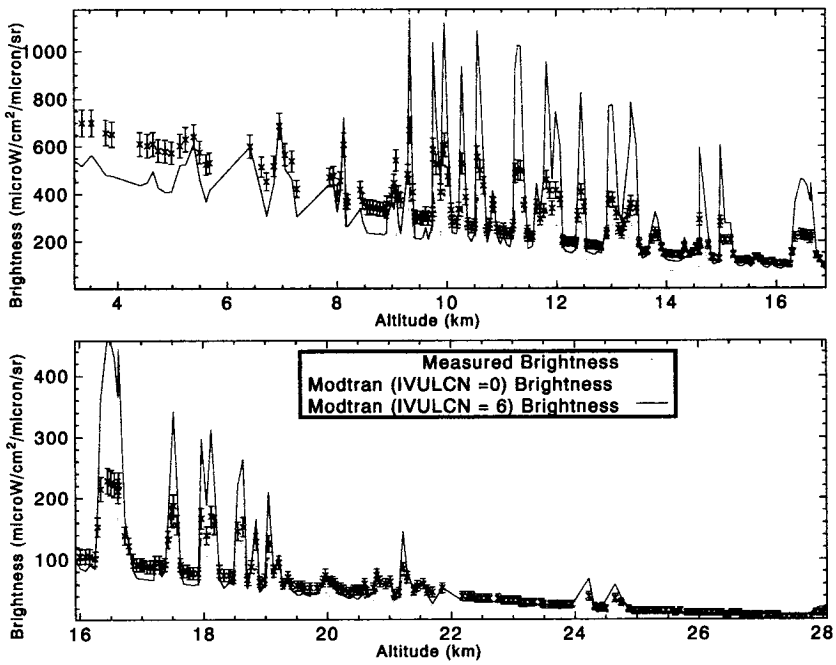

Figure 4.7: Sky brightness derived from background data taken during ascent. The poor agreement between model and data at low altitude is likely due to the close proximity of Mount Erebus during ascent, a known source of stratospheric aerosols. Two model brightness profiles are shown, varying the parameter IVULCN which controls the choice of aerosol profile and the type of extinction for the stratospheric aerosols. IVULC = 0 is the nominal case. IVULCN = 6 corresponds to a moderate volcanic aerosol profile. At high altitude the model profiles converge and are in good agreement with the data.

The two model curves illustrate the sensitivity of the model to aerosol profile. At high altitude the model profiles converge and are in good agreement with the data.

4.4 Flight Performance

The 15 day flight resulted in ~11.5 days of good science data. Data near the end of the flight was deemed unusable because of the low altitude wind shear which made pointing the telescope impossible. In addition erratic signals, caused by such events as elevation changes and the large ballast drop, had to be cut from analysis. A total of

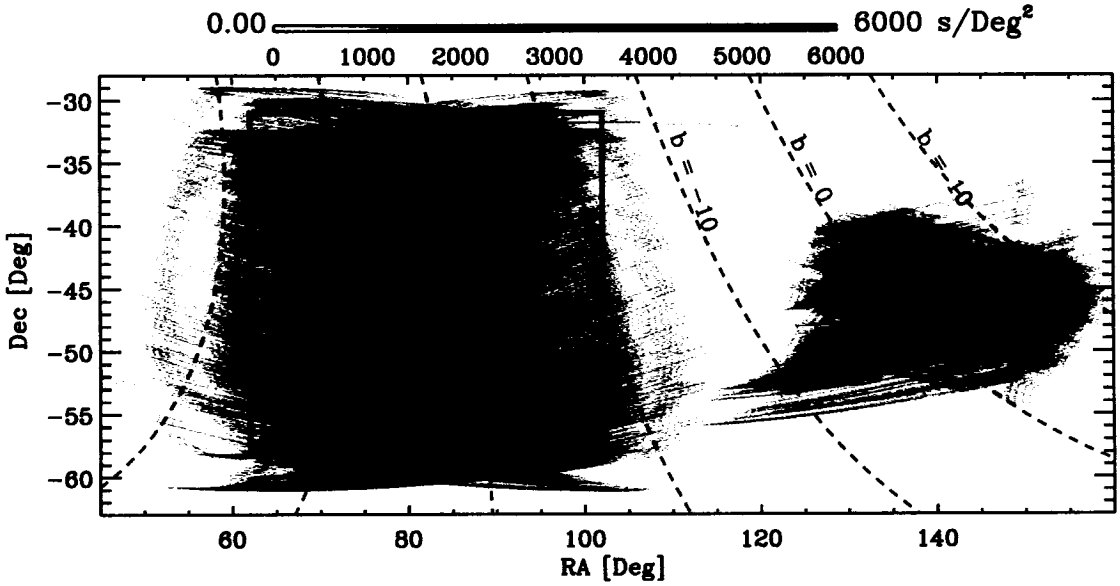

Figure 4.8: Map of B03 observation time taken from [57] for the "Shallow" and "Galaxy" survey regions. The CMB deep survey region corresponds to the smaller box.

228 hours of data covering three survey regions are obtained. The CMB deep survey region is comprised of 119 hours of data. The CMB shallow region accounts for 79 hours of observation. Finally, a Galactic plane region consists of 30 hours of observing time. The sky coverage is illustrated in Figure 4.8, with the three observation regions highlighted. The CMB deep and shallow region area and observation time were chosen in order to optimize the telescope's sensitivity to the polarization (deep) and cross-polarization (shallow) power spectra.

4.4.1 Cryostat and Receiver Performance

The receiver worked well throughout the flight. The cryostat kept the detectors cold for 11 days after which it began to warm up. The cryostat was then successfully re-cycled in-flight, and 19 additional hours of data were acquired. The payload diurnal altitude oscillations are correlated with the bolometer response. Changes in altitude have an

impact on the bolometer optical load, and the temperature of the cryostat, both of which may have an effect on the bolometer resistance. This drift in bolometer responsivity is monitored by the amplitude of the calibration lamp pulses throughout the flight and is at most a few percent.

The upper right panel of Figure 4.9 illustrates the calibration drift in B145W1 over the course of the flight. The drift is most correlated (a correlation coefficient of -0.67) with the readout of the ^{4}He cryopump temperature sensor, shown in the upper left panel of Figure 4.9[1]. At lower altitudes, corresponding to higher pressure, the cryostat operates at a warmer temperature causing a decrease in the detector calibration. The ^{4}He cryopump temperature data is linearly correlated with GPS altitude. This relationship is used to convert ^{4}He cryopump temperature into the corresponding gondola altitude. The lower panel in Figure 4.9 is a plot of gondola altitude versus calibration drift. The resulting empirical relationship between altitude and calibration drift derived from these data is,

$$Altitude[m] = 166769 Calibration - 132937 \tag{4.1}$$

Thus, the altitude change (and subsequent pressure change) from 30 km to 25 km causes a calibration drop of about 3%, from 0.98 at 30 km to 0.95 at 25 km. While optical loading from the atmosphere is higher at lower altitudes there is no evidence at all for an effect from the atmosphere directly.

4.4.2 ACS Performance

The ACS performed well throughout the flight. Motion control was virtually flawless in both the azimuth scanning and the drive of the inner frame elevation. The GPS and FSS provided the required coarse, ~10 arcminute in-flight azimuth pointing and the

[1]The calibration drift is also correlated with other temperature sensors and the GPS altitude but with a complicated phase shift.

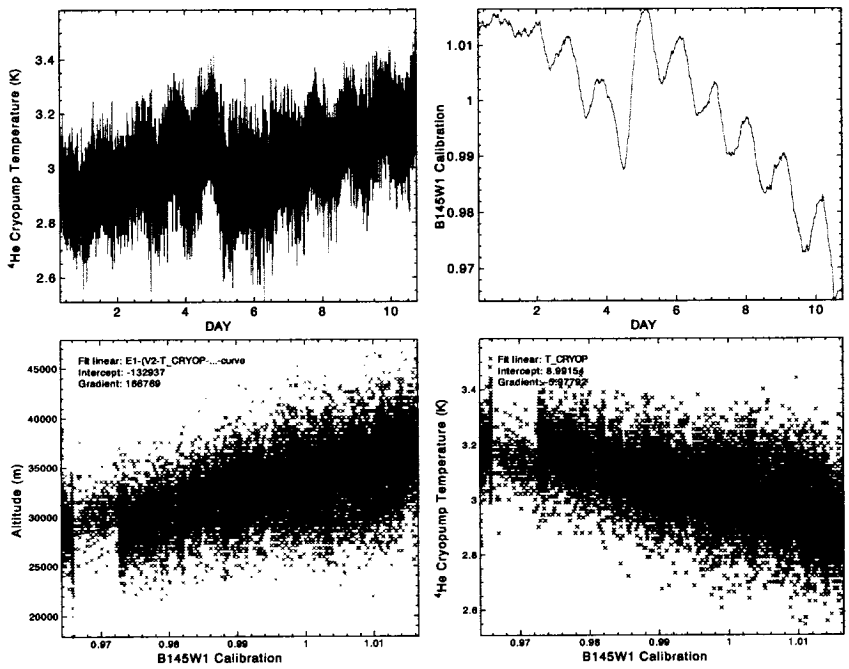

Figure 4.9: The upper right panel is a plot of the calibration drift in B145W1 over the flight. The drift is correlated with the ^{4}He cryopump temperature (upper left panel). At lower altitudes, corresponding to higher pressure, the cryostat operates at a warmer temperature causing a decrease in the detector calibration. The lower panels show plots of gondola altitude and cryopump temperature both versus calibration drift. The calibration changes by a few percent over a 5 km range.

gyroscopes functioned continuously. Near the end of the flight, once the payload altitude dropped below ~23 km, high winds made motion control unfeasible and the ACS was shut down.

Performance of the tracking sensors, the SC and the PSS, was marred by communication problems in the ACS flight logic computer. With both sensors operating at the same time the computer was unable to parse the large amounts of incoming and outgoing data. To resolve this issue the PSS was turned off early in the flight. The SC provided the fine pointing data for the first and last thirds of the flight. The cold temperature at low (pre-ballast drop) altitude on day 4 caused the SC to freeze up, at which point the PSS was turned back on, providing fine pointing for the middle third of the flight. Fig-

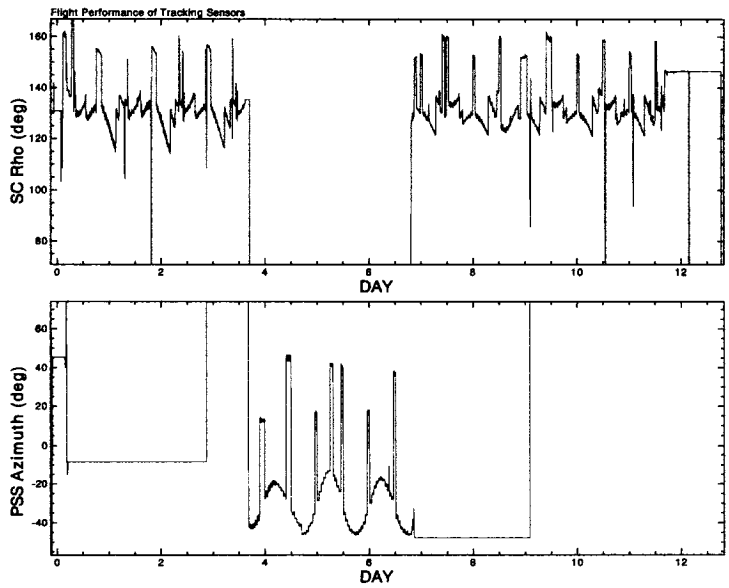

Figure 4.10: Raw data from the SC and PSS. The SC was operational for the first and final thirds of the flight. The PSS operated for the middle third of the flight.

ure 4.10 shows raw data from both the SC and PSS indicating when each of the sensors was operational. Unfortunately, the PSS data was determined to have large, long time scale drifts which could not be reconciled with the other pointing sensors and thus was not used in the final pointing solution.

Gondola Buffeting

The derivation of the final pointing solution is described in detail in Section 6.2. In Figure 4.11 the final solution for gondola pitch is compared with the pitch derived from the GPS velocities. This comparison is made for the first third and last third of the flight, when the SC was operational and is the dominant component in the final pitch solution. On short time scales the two pitch timestreams are generally in agreement. Buffeting or excess pendulations of ~ 0.1 degree amplitude are apparent on times scales greater than a few minutes in the final pitch solution. The pitch derived from the GPS velocities is not sensitive to pendulations at this frequency. The buffeting of the gondola against the

wind becomes more apparent near the end of the flight, at lower altitude. As mentioned previously once altitude dropped below ~23 km winds were too high to allow operation of the ACS.

Star Camera Performance

The star camera performance was complicated by two factors; an overflowing data buffer (PV to serial concentrator) and an overworked ACS CPU. Despite turning off the PSS, the raw SC data is complicated by repeated frames. The SC was unfrozen (literally) for ~65% of the flight. Throughout the flight (when it wasn't frozen) the SC performance can be characterized by three "modes".

The first mode is a "lock/unlock" mode. In this mode the star camera initially locks onto a star with the nominal ACS (10 Hz) operation. The star gradually drifts out of the field of view because of repeated SC feedback (out-dated star positions) arising from buffer overflow. Eventually star lock is lost, only to be regained moments later when the SC has received updated ACS parameters and is able to lock onto the same star again. This process is repeated every minute or so for this SC mode of operation and is corrected by removal of repeated frames and linear interpolation of gaps (see Section 6.2.1).

In the second mode the SC remains locked on a star. This happens ironically when the ACS is not operating at its nominal data processing rate. With the ACS running slow, the SC program seems to have enough time to to get updated parameters. Once the ACS is operating at full speed the SC eventually loses lock again.

The first and second modes alternate, each lasting for about 40 minutes. Of course when switching from one mode to the other the SC has a brief intermediate mode when it is completely not obvious what is going on and how it can be fixed. Thankfully these stretches of data are short and can be flagged and eventually filled with integrated gyroscope data. In conclusion, 40% of the SC azimuth and 70% of the SC elevation data were salvageable. The pointing reconstruction details are outlined in Chapter 6.

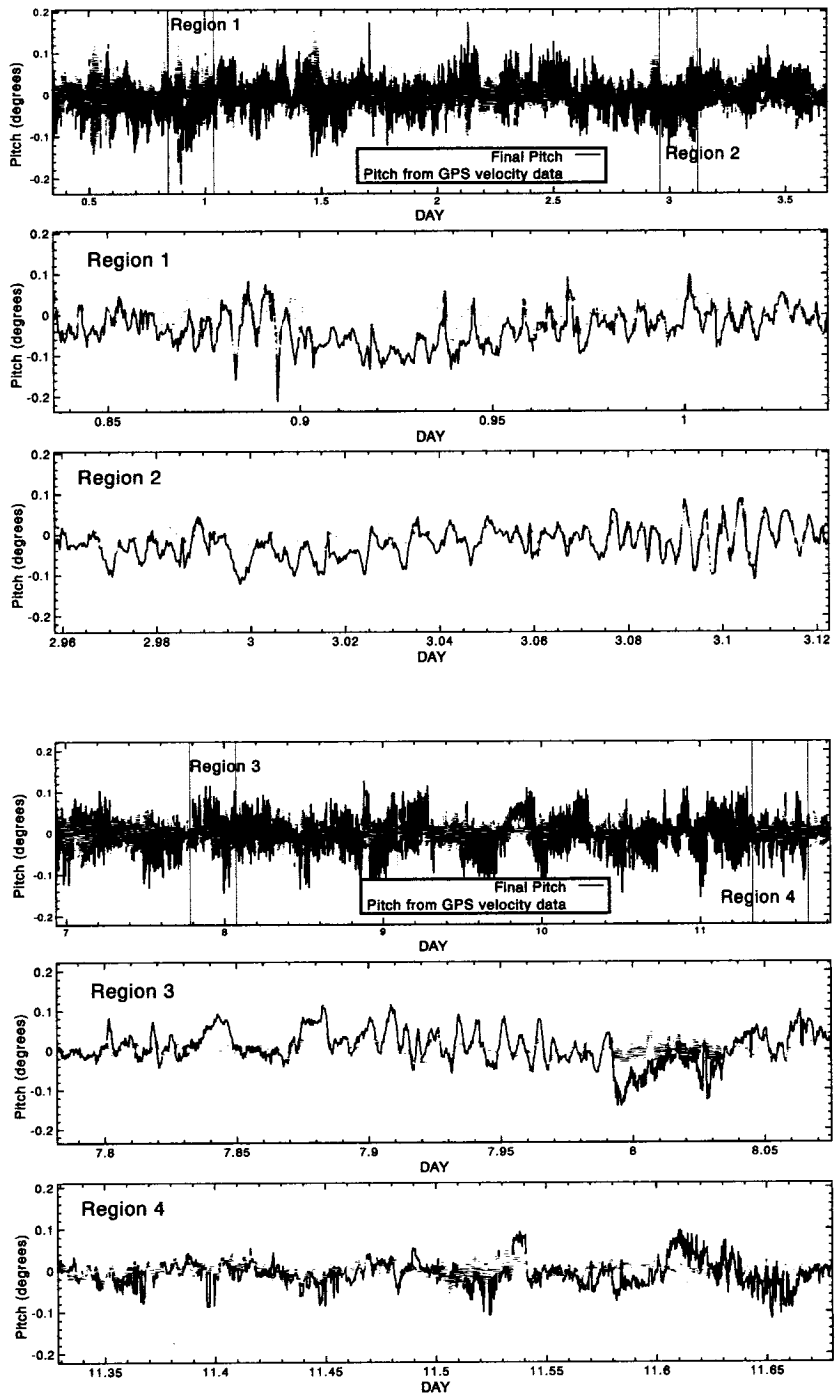

Figure 4.11: Comparison of the final pointing solution (see Section 6.2) for gondola pitch with the pitch derived from the GPS velocities, zooming in on four regions of the timestream. At high frequencies the two pitch timestreams are generally in agreement. Excess pendulations of $\sim$ 0.1 degree amplitude (detected by the SC) are apparent on times scales greater than a few minutes in the final pitch solution.

Chapter 5

Instrument Characterization

A number of tests were performed before and during the flight in an effort to obtain various instrument parameters such as calibration, channel beams, detector time constants and polarization parameters. Pre-flight tests for balloon-borne experiments must be extensive in order to ensure instrument operation during the flight. The summary here is by no means exhaustive, giving the results of only the most pertinent tests. Further discussion of receiver pre-flight testing can be found in [59, 41, 66].

5.1 Pointing Sensor Alignment

Precise alignment of the pointing sensors is crucial for in-flight motion control and post-flight pointing reconstruction. The pre-flight calibration of the differential GPS was performed, obtaining a baseline orientation accurate to $\sim$ 10 arcminutes. This self-survey calibration was run for no less than $\sim$ 8 hours, on a level platform (zero pitch and roll) as recommended in the *TANS VECTOR Specifications and Users's Manual.* Once GPS frame orientation was obtained, the azimuth offset angle between the FSS and the GPS was determined. The FSS gives the azimuth of the sun relative to the back gondola outer frame. This GPS to FSS offset angle is required to translate the GPS array azimuth (relative to north) into *gondola* azimuth. A schematic of the GPS array

Pointing Parameter	Measured Value
GPS to Gondola Azimuth	114.965 deg
SC Pixels to Arcseconds in x	3.79 arsec/pix
SC Pixels to Arcseconds in y	4.00 arcsec/pix
SC ρ/θ to SC az/el:	
'azimuth'	260.2 deg
'pitch'	139.0 deg
'roll'	-2.4 deg

Table 5.1: B03 pointing alignment parameters.

indicating the orientation of the array axes with respect to the front of the gondola is depicted in Figure 3.11. Once the GPS array alignment is determined it is important that that array remained fixed to ensure that the offset angle remain constant. Depending on which sensor is operational either the GPS or FSS (the FSS is the default) provide a continuous measure of the gondola azimuth throughout the flight.

The FSS is complicated to calibrate since the sensor response is not linear but has dependence on both sun elevation and azimuth. The FSS was first calibrated on the ground using a bright lamp. The sensor was then re-calibrated using flight data in the form of a lookup table with an azimuth element for each sun elevation. A full description of the FSS calibration for the B98 and B03 flight can be found in [19, 66].

The calibration and alignment of the star camera with the gondola was a two-step process. First the conversion factor from pixel to degrees on the sky was obtained by observing a white spot on a dark background sheet ~20 meters away. The spot was tracked to the edges of the field of view (in both x and y) and the ρ and θ encoder readouts were used to translate pixel position into degrees. Next, the angles which translate star position in the SC ρ and θ coordinates to star azimuth and elevation (relative to the SC frame) were determined. The process of surveying the star camera mount was initially approximated using an angle gauge to measure the tilt of the star camera mount relative to the gondola outer frame. The fine tuning of the calibration angles was done at night in the field in Palestine, Texas during pre-flight integration and testing during the summer

of 2001. A program which took input RA and DEC and translated this to star camera encoder counts was written, pointing the star camera to the desired (approximate at first) region on the sky. The angles were adjusted empirically using two widely separated guide stars on the sky. When the two stars, in turn, appeared in the centre of the field of view, the mount was properly aligned with the (level!) gondola. Upon arrival in Antarctica the survey of the star camera mount was repeated to ensure that (after > 1.0 years in a damp storage facility in New Zealand) the alignment was still in fact correct[1]. The various alignment angles and conversion factors are summarized in Table 5.1.

5.2 Beams

Two methods were used to characterize the beam profiles of B03. The first involved a pre-flight measurement of the beams by mapping a thermal source which is attached to a tethered dirigible. The source is made out of a microwave emitting material, eccosorb, and is positioned a distance $\sim$1.5 km away from and $\sim$1 km up from the B03 gondola. Two sources were used to characterize the beams. A small sphere ($\sim$45 cm diameter) was used to measure the main beam lobe and a larger cylindrical source ($\sim$76 cm diameter and $\sim$91 cm in height) was used to map out the beam sidelobes. The telescope scanned over the source while the star camera tracked the source position. A modified version of the star camera tracking code, which tracked dark rather than bright objects in the field of view, was developed in order to lock onto the source which, in the visible, appears dark on top of the bright Antarctic daytime sky. The resulting FWHM beam widths determined from fits to the small sphere source are given in column one of Table 5.2.

The second method of beam determination involves calculation of the physical beam using the BMAX physical optics model of the system. The resulting FWHM beams (azimuth and elevation) from the optics model calculation are presented in Table 5.2.

[1]And miracle of all miracles it was!

B03 Channel	Measured FWHM	Calculated $FWHM_{Az}$	Calculated $FWHM_{El}$
145W1	9.8	9.76	9.92
145W2	9.8	9.76	9.92
145X1	9.6	9.75	9.88
145X2	9.7	9.78	9.88
145Y1	10.0	9.78	9.87
145Y2	10.0	9.75	9.88
145Z1	9.9	9.75	9.92
145Z2	9.6	9.78	9.92

Table 5.2: B03 physical beams in arcminutes determined from the far field beam mapping experiment and from physical optics calculations. Calculated and measured beams are in good agreement.

The agreement of the measured physical beam and the predictions of the BMAX code is very good. The physical optics calculations were performed by Bill Jones and full details can be found in [41].

Having verified the accuracy of the physical optics calculations, the physical beam must be convolved with the pointing error in order to determine the final effective beam on the sky. The pointing solution methodology is described in detail in Section 6.2. The resulting pointing error is determined from comparison of calculated physical beams with profiles from the five brightest quasar sources in the deep field CMB maps. The pointing error is assumed to be Gaussian and uniform over all observed regions of the sky. The final effective beam used for all of the 145 GHz channels in the analysis is assumed to be Gaussian with a FWHM $= 11.5 \pm 0.23$ arcminutes, consistent with the FWHM of the quasars.

5.3 Time Constants

The frequency response of a bolometer can be modeled as a first order (one pole) low pass filter. The contribution from the bolometer thermal time constant is combined with the transfer function of the readout electronics to give the full system transfer function. The

full detector + readout transfer function which must be deconvolved from the timestream data in order to obtain the true signal on the sky. The transfer functions were determined pre-flight, first by measuring the electronics transfer function. The electronics result is multiplied by the bolometer transfer function which were measured using a 77 K liquid nitrogen load observed through a cold (2 K) Neutral Density Filter. This setup simulates the in-flight detector loading. The resulting time constants for the 145 GHz channels range from 43-97 ms with uncertainties $\sim 10\%$.

5.4 Calibration and Sensitivity

The bolometer responsivity depends both on the incident power and on the operating temperature. Varying altitude during the flight can affect both of these quantities. The resulting long-term gain drifts in the bolometers were determined by monitoring the amplitude response from the calibration lamp, which flashed every ~15 minutes throughout the flight.

The absolute calibration factor or responsivity, S_i, for each channel is determined by comparing angular power spectra measured by B03, WMAP and B98 in the same region of the sky. The uncalibrated B03 voltage signal is related to the CMB intensity measured by WMAP as $I_{WMAP} = V_{B03}/S_i$. The calibration procedure begins by making resampled WMAP maps for each B03 channel to ensure that the flagging and pointing are consistent. The calibration factor is determined from the ratio of the cross spectra,

$$S_i(\ell) = \frac{\langle a_{\ell m}^{WMAP} a_{\ell m}^{*\,B03} \rangle}{\langle a_{\ell m}^{WMAP} a_{\ell m}^{*\,WMAP} \rangle} \quad \text{or} \quad S_i(\ell) = \frac{\langle a_{\ell m}^{B98} a_{\ell m}^{*\,B03} \rangle}{\langle a_{\ell m}^{B98} a_{\ell m}^{*\,WMAP} \rangle} \tag{5.1}$$

Here, the beams for the respective experiments have been deconvolved from the $a_{\ell m}$s and, to the limit that all transfer functions have been properly removed, there should be no variation in the two ratios. Both ratios yield calibration factors as a function of ℓ. To obtain the final $\mu K/V_{DAS}$ calibration factor for each channel the data are binned in the

B03 Channel	Calibration ($\mu K/V_{DAS}$)	NET ($\mu K_{CMB}\sqrt{s}$)
145W1	163500.0	143.359
145W2	172700.0	138.604
145X1	167200.0	156.062
145X2	222700.0	152.749
145Y1	180200.0	158.001
145Y2	188900.0	166.965
145Z1	243600.0	186.031
145Z2	384200.0	281.18
245W	397900.0	281.358
245X	505900.0	357.726
245Y	446800.0	315.935
245Z	468600.0	331.351
345W	648800.0	458.771
345X	599500.0	423.91
345Y	876300.0	619.637
345Z	436900.0	308.929

Table 5.3: B03 calibration and sensitivity. The calibration is determined by comparing angular power spectra measured by B03, WMAP and B98 in the same region of the sky. The error in the final calibration is 2%. The sensitivity is in terms of in-flight noise equivalent temperatures (NETs) at a frequency of 1 Hz.

ℓ range from 100-300 and an average and standard deviation are determined. The final values from both ratios are entirely consistent. The calibration results are summarized in Table 5.3. The error in calibration is roughly 2%.

The in-flight noise is obtained via the Fourier transform of the timestream data (after the data have been deconvolved from the system transfer function). Figure 5.1 illustrates deep field averaged power spectral densities (PSDs) for channel B145W1. The top curve is the PSD of the raw timestream (signal plus noise) from channel B145W1. The middle curve is an estimate of the channel noise in terms of the noise only auto PSD. The CMB signal lies in the 0.05 to 1 Hz range. The bottom curve illustrates the cross correlation of B145W1 with B145W2. In general, in the 0.05-1 Hz range, the correlated noise is at least one order of magnitude below the auto-correlated noise. Noise correlations are irrelevant for the TT spectrum analysis, but must be treated carefully in order to extract the order

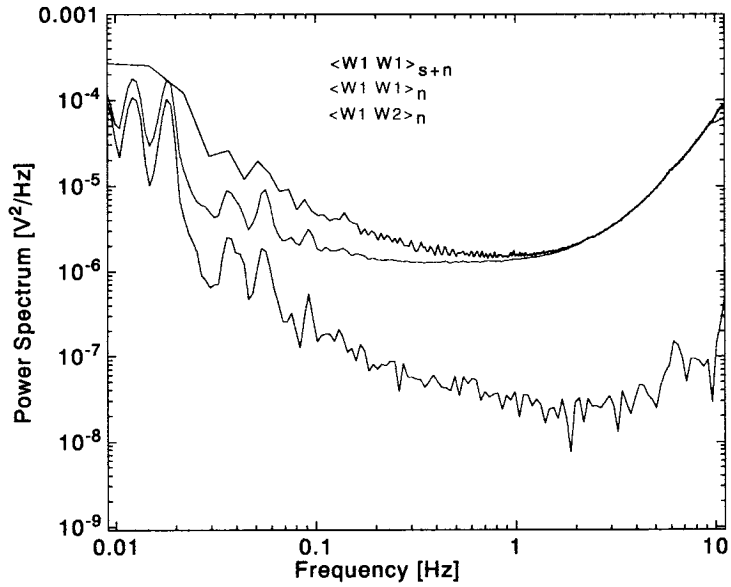

Figure 5.1: Deep field averaged power spectral densities (PSDs) for channel B145W1. Comparison of the top curve–signal plus noise PSD–and middle curve–noise only auto PSD–illustrates that the CMB signal lies in the 0.05 to 1 Hz range. The bottom curve is the cross correlation of B145W1 with B145W2. In the 0.05-1 Hz range, the correlated noise is at least one order of magnitude below the auto-correlated noise.

of magnitude smaller polarization signal. The noise estimation technique and treatment of correlated noise is discussed further in Section 6.4.

The detector sensitivity or noise equivalent temperature (NET) in units $\mu K_{CMB}\sqrt{s}$ is determined by dividing the measured in-flight voltage noise (in $V/sqrtHz$) by the channel responsivity to CMB. The NETs give a measure of the performance of the bolometer and readout electronics. Strictly speaking the NET is the temperature difference that will create a signal to noise ratio of unity. The in-flight NETs at 1 Hz are given in Table 5.3.

5.5 Polarization Properties

The polarization of a detector is characterized by two variables: the polarization angle, ψ_i, and polarization efficiency, ρ_i. The ψ_i alignment angle gives the orientation of the

bolometer on the sky. The polarization efficiency is the percentage or fractional efficiency of a detector to incident polarization. For example, a PSB with 95% efficiency will transmit 95% of the incident radiation in the intended linear polarization and 5% in the orthogonal polarization.

The polarization properties of each channel were measured before the flight using two methods. The first measurement involved placing a thermal source at the prime focus of the cold optics and determining the polarization properties for the receiver alone. The source is a 77K liquid nitrogen bath which is modulated by a chopper wheel rotating at 2Hz. A rotating polarization grid, with a ~10 min period of rotation, is placed directly beneath the cryostat window, in front of the chopped source. In the second measurement the polarization properties of the whole instrument are determined by simulating a far field polarized source. The far field source is produced by placing the liquid nitrogen load, chopper and grid combination in the focus of the spare B03 primary. The spare primary is inverted and mounted in an aluminum frame at a distance $\sim$ 6 m from the B03 telescope. The equation which describes the observed signal in both cases is given by a modified Malus's Law whereby,

$$V_i = S_i I_0 (1 - \rho_i sin^2(\psi_i - \psi_{grid})) \tag{5.2}$$

where S_i is the absolute calibration of a given detector, I_0 is the incident power, ρ_i is the detector's polarization efficiency (or $\epsilon_i = 1 - \rho_i$ is the cross polar response), ψ_i is the detector's polarization angle and ψ_{grid} is the transmission angle of the polarization grid. The polarization properties are determined by fits to the above equation for a variety of grid angles. Results from the two methods are entirely consistent when the polarization properties of the simulated far field source are taken into account. The results are presented in Table 5.4. The uncertainty in polarization angle measurement is roughly 2° and in cross polarization is 3%.

B03 Channel	Polarization Angle (deg)	Polarization Efficiency, $1-\epsilon$
145W1	134.90	0.920
145W2	44.80	0.938
145X1	178.40	0.945
145X2	89.00	0.930
145Y1	157.90	0.949
145Y2	67.00	0.940
145Z1	109.50	0.818
145Z2	23.20	0.912
245W	139.3	0.993
245X	42.9	0.993
245Y	179.5	1.000
245Z	86.9	0.986
345W	139.8	0.992
345X	42.8	0.992
345Y	179.7	0.996
345Z	86.5	0.982

Table 5.4: The polarization angles and polarization efficiencies, determined pre-flight for each channel. The uncertainty in polarization angle measurement is 2° and in cross polarization is 3%.

Chapter 6

The CMB Pipeline: From Raw Data to Power Spectra

In this chapter the CMB analysis pipeline is outlined beginning with the raw data obtained from the pointing sensors and bolometers followed by the the temperature and polarization maps, and ending with the power spectra. The final stage of analysis, the extraction of parameters from the power spectra, is outlined in Chapter 7. The first task to perform, outlined in Sections 6.1 and 6.2, is the cleaning and calibration of the raw sensor data in order to produce what can be deemed *the idealized data set.* Once an idealized data set is realized a noise model, in parallel with a best estimate signal-only map, are obtained using an iterative map-making process. These details are given in Sections 6.3 and 6.4. With a noise model, idealized data set, an iterative map maker and CMB sky simulator a Monte Carlo approach, described in Section 6.5, can be used to estimate the power spectra. The resulting power spectra from the analysis pipeline are presented in Section 6.6. An overview of the analysis pipeline is show in Figure 6.1.

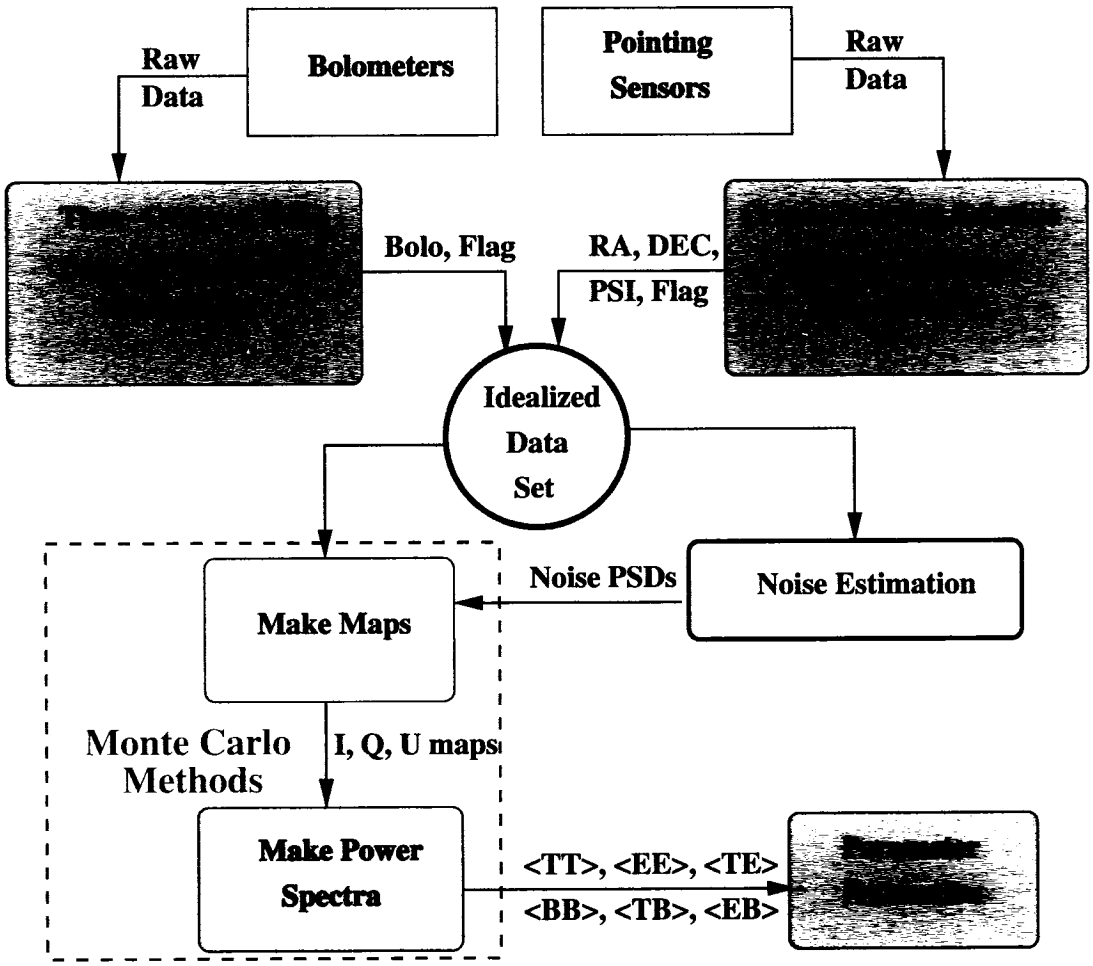

Figure 6.1: CMB analysis pipeline overview.

6.1 Bolometer Data

This section gives a brief outline of the issues involved in the cleaning and deconvolution of bolometer data. A more detailed description of various techniques can be found in [19, 59, 41]. The raw bolometer data contains various undesirable artifacts such as comic ray spikes, calibration lamp spikes and thermal instabilities resulting from elevation changes. In addition to these effects the bolometer data is convolved with a transfer function derived from the detector thermal response and the filtering of the receiver readout electronics. Given that the signal to be extracted is very tiny it is paramount

that these effect be carefully accounted for and removed from the timestream.

The first step in bolometer data cleaning is the identification of segments of timestream when events occurred, for example launch or fridge cycling, which completely marred the timestream data. These "glitches" are removed and flagged as bad data. The remaining gaps in the data are filled with constrained realizations of the noise. These segments of flagged data are subsequently not used in analysis but gap filling is necessary to allow for the Fourier transform of the data timestream.

The "de-glitched" bolometer data are deconvolved with pre-flight determined transfer functions. At this point, spikes caused by cosmic rays and calibration lamp pulses, are removed from the de-glitched, deconvolved data. Care must be taken to ensure that bright sources, which can be mistaken for comic ray spikes, remain in the timestream. These foreground sources are eventually removed from the CMB maps, but in the intermediate analysis, are used as pointing calibrators. A gyro-correlated signal is removed in the final stage of data cleaning. Long term calibration drifts, resulting from change in cryostat pressure associated with varying altitude, are corrected for in the final step.

6.2 Pointing Solution

6.2.1 Cleaned, Calibrated and Derived Pointing Data

Spikes in the raw pointing data caused by spurious events are removed and where possible (over a few samples) the data is linearly interpolated. This is done simply by comparing the pointing data in one sample with the data in neighboring samples and linearly interpolating if that particular sample is above some reasonable threshold. The data cleaning for the gyros, GPS and the FSS was straight-forward since all of these instruments operated continuously throughout the flight. The star camera data cleaning is much more difficult since its operation was not continuous and is complicated by repeated data (see Section 4.4.2).

Post-flight re-calibrations are applied to the SC, PSS and FSS data. For the SC/PSS azimuth and elevation this is a matter of rotating the coordinates through a small angle until the azimuth correlated signal in elevation is minimized. The FSS is recalibrated using azimuth data from the GPS and the SC. A look-up table of sun elevation versus raw FSS azimuth is constructed. Each element of the table contains a GPS/SC-derived, sun azimuth relative to the gondola, averaged over the whole flight. Raw FSS data is replaced by the corresponding element in the table.

The raw data from the azimuth, pitch and roll gyroscopes also required re-calibration given that the signals from these sensors are not completely orthogonal. To achieve this the gyroscope data are rotated until the correlated signal is a minimum. The large amplitude pendulations just after launch provided a good signal-to-noise ratio to ensure decorrelation of the gyroscope sensor signals.

Star Camera Data

Considerable effort was made to remove repeated samples of SC data. An algorithm was developed which searched for repeated frames and removed them from the timestream. The strategy for finding contaminated frames is to search for frames which were repeated in more than one pointing field, ensuring that the correct frame was removed. This worked well for the 'lock/unlock mode' (see Section 4.4.2) but not as well for 'intermediate modes'. In the end, data which could not be salvaged was flagged by hand. Figure 6.2 show the SC azimuth field, before and after corrections have been made. The effect of repeated frames on elevation data is less severe since the gondola moves very little in elevation during a scan. For this reason more of the elevation data can be preserved. The star camera was unfrozen (literally) for 65% of the flight. From this 40% of the SC azimuth and 70% of the SC elevation data were salvageable. Much of the flagged data is within $\sim$30 seconds of unflagged data and the gyroscope data can be used to fill in the gaps.

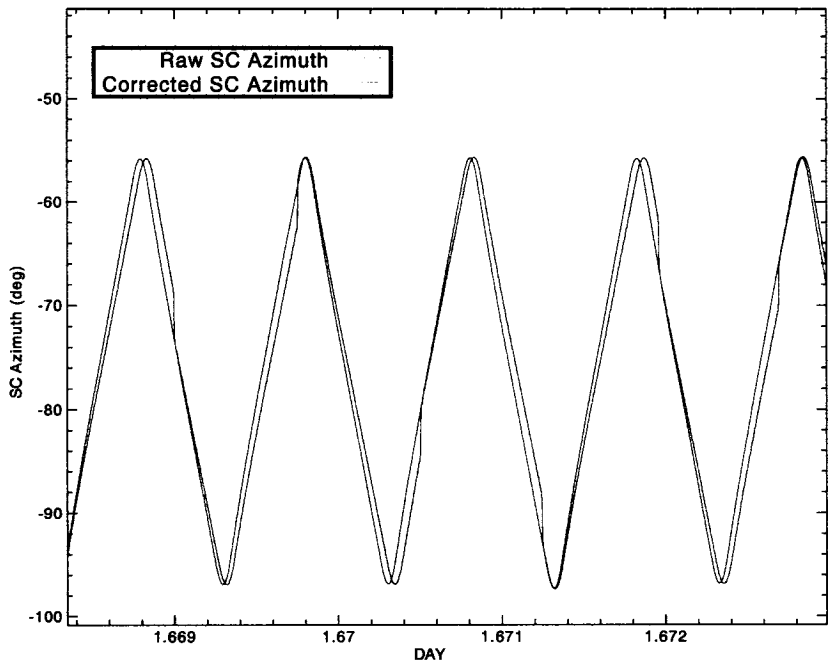

Figure 6.2: Comparison of raw and corrected SC azimuth. In the corrected field repeated frames have been removed from the timestream.

Cleaned SC data are rotated from SC $\rho - \theta$ coordinates into azimuth-elevation coordinates. At this stage star position pixel information is included. The pre-flight determined calibration angles are adjusted at this point to ensure that the correlation between azimuth and elevation in the final SC pointing fields is minimal.

Derived Pitch and Roll

A useful derived quantity is obtained from the GPS up, north and east velocity data. The relatively stable LDB environment allows one to model the gondola as a pendulum; the arcsine of the acceleration of the gondola (determined from the derivative of the GPS velocity fields) is proportional to the pitch or roll. Is should be noted that the GPS provides platform pitch and roll data but it is only accurate to $\sim$ 6 arcminutes. The pitch and roll which are derived from the GPS velocity data (accurate to 0.1 m/s RMS)

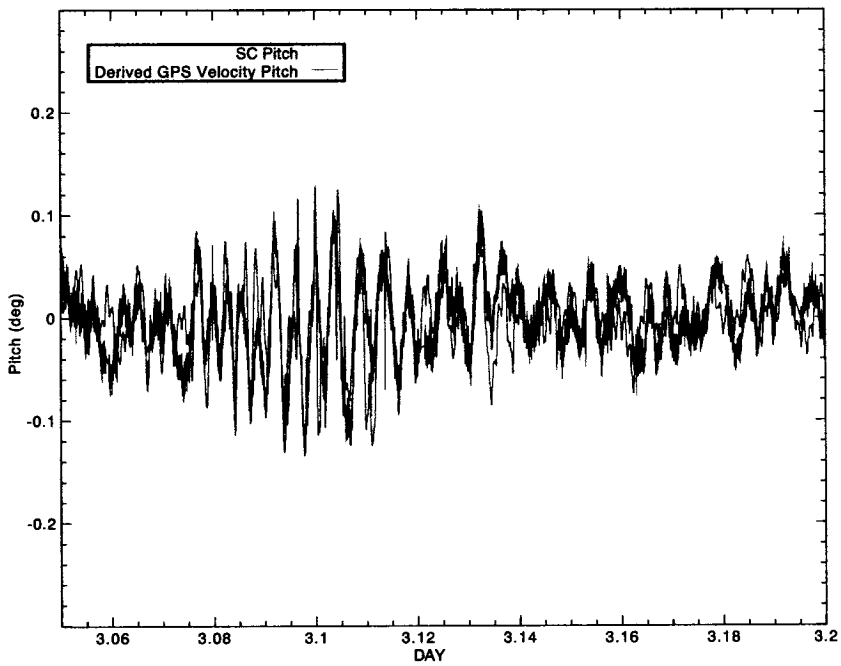

Figure 6.3: Comparison of the derived GPS velocity pitch with the SC determined pitch over a three hour time scale. These pointing fields are in good agreement for this chunk of data.

are precise to ~ 2 arcminutes on time scales less than a few hours. With this model first estimates of gondola pitch and roll, $PITCH_{GV}$ and $ROLL_{GV}$ may be calculated from the GPS velocity data. In Figure 6.3 the derived GPS velocity pitch is plotted (over roughly a three hour time scale) along with the SC-determined pitch. These pointing fields are in good agreement for this chunk of data. Agreement seems to worsen at lower altitudes, where wind shear is presumably higher.

6.2.2 Determination of Absolute Gondola Attitude

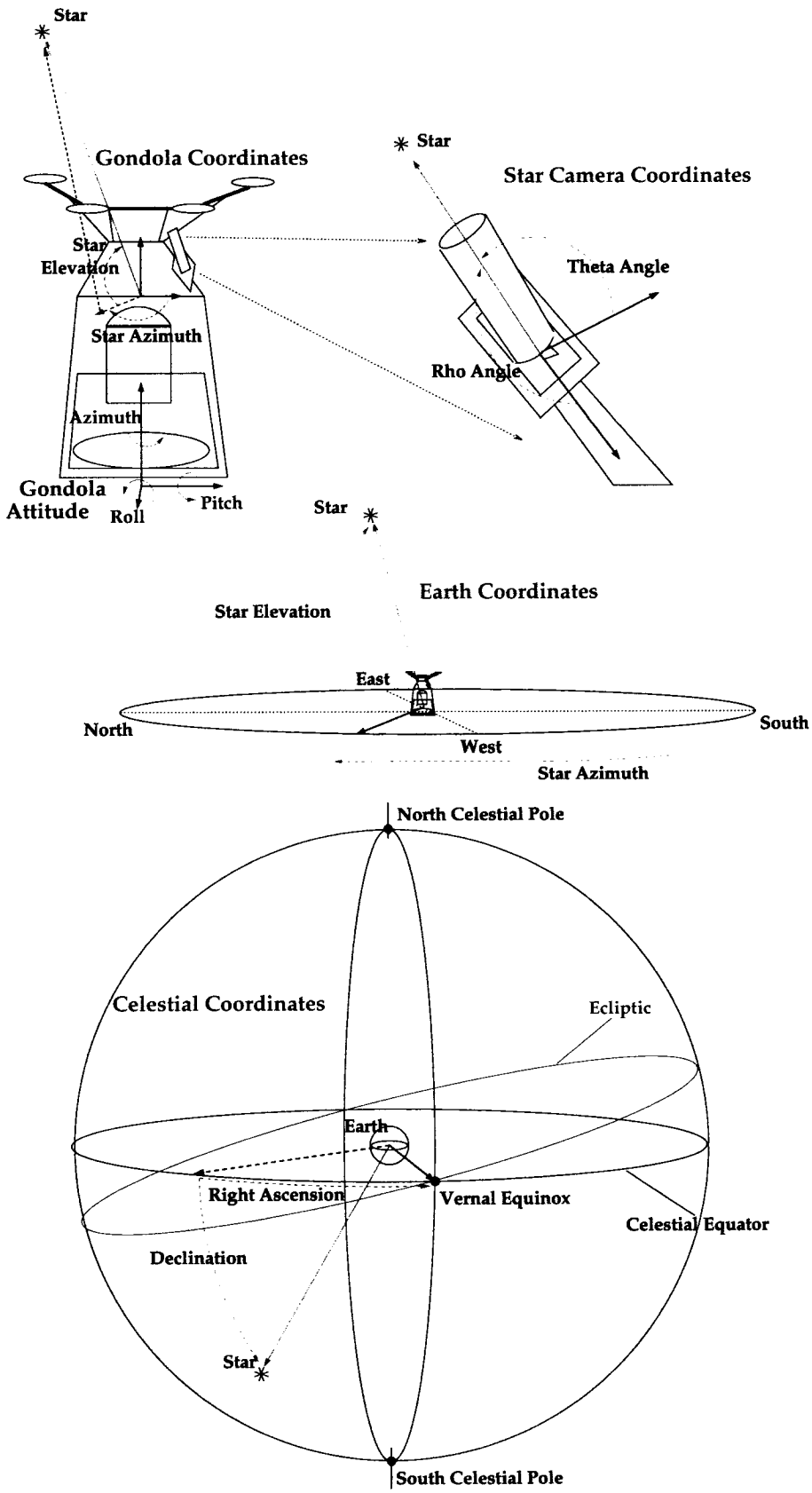

Figure 6.4: Star position defined in various coordinate systems.

Clean, calibrated pointing fields are combined to determine the gondola attitude, an Euler matrix describing the azimuth, pitch and roll of the gondola outer frame relative to the Earth. Figure 6.4 illustrates the gondola attitude matrix and the various coordinates systems used to describe the position of the Sun or a guide star. The pointing fields used in the final analysis include the FSS azimuth, the SC elevation, the $PITCH_{GV}$ and $ROLL_{GV}$ fields derived from the GPS velocity and the gyro-integrated azimuth, pitch and roll provide pointing information at different frequencies. For example the FSS, SC and $PITCH_{GV}$ and $ROLL_{GV}$ provide the long time scale, absolute pointing while the gyros provide the short time scale pointing data. At frequencies below ~50 MHz the pointing solution is based on the best fit azimuth, pitch and roll to the sun and star positions as determined by the star camera, the FSS, $PITCH_{GV}$ and $ROLL_{GV}$. Above this frequency threshold the solution is provided my integrated gyroscope data.

The SC-Gondola Rotation Matrix

The determination of the gondola attitude necessitates that the star and sun position information be in the same frame of reference. This requires calculation of the rotation matrix, $\mathbf{R}^{SCtoG}$, which converts star position in the SC frame into star position in the gondola reference frame. The gondola reference frame is (arbitrarily) chosen to be the the position of the sun/star relative to the back of the gondola outer frame. The FSS is bolted to the back of the gondola and thus is already in the required frame of reference. The Euler matrix $\mathbf{R}^{SCtoG}$ is constant over the flight (to the required level of accuracy) and is determined by fitting for the Euler angles which minimize the difference between the SC determined star position and the star position derived from a first guess gondola attitude (using FSS azimuth, $ROLL_{GV}$ and $PITCH_{GV}$).

Sun and Star Positions Relative to Gondola

The next step involves the determination of the two vectors describing the star and sun positions which use the best available sensor data for each time sample. The (measured) star position vector (azimuth and elevation of current locked star in the gondola reference frame), $\hat{x}_\star^G$, and (measured) sun position vector (azimuth and elevation of sun in the gondola reference frame), $\hat{x}_\odot^G$, along with the (known) star and sun positions relative to Earth, $\hat{x}_\star^E$ and $\hat{x}_\odot^E$ make up a solvable system of equations with the unknowns characterized by three Euler angles of the gondola attitude matrix $\mathbf{R}^{GtoE}$. This system of equations can be summarized by,

$$\mathbf{R}^{GtoE}\hat{x}_\star^G = \hat{x}_\star^E \tag{6.1}$$

$$\mathbf{R}^{GtoE}\hat{x}_\odot^G = \hat{x}_\odot^E. \tag{6.2}$$

Solving for the Euler Angles

The angles of the gondola attitude matrix, $\mathbf{R}^{GtoE}$ are solved for using a simple grid search of the three-dimensional χ^2 space to determine the least squares solution. That is minimizing the χ^2 term

$$\chi^2 = \left(\frac{(\mathbf{R}^{GtoE}\hat{x}_\star^G - \hat{x}_\star^E)^2}{\hat{\sigma}_\star^2} + \frac{(\mathbf{R}^{GtoE}\hat{x}_\odot^G - \hat{x}_\odot^E)^2}{\hat{\sigma}_\odot^2} \right) \tag{6.3}$$

where the errors are based on the estimated accuracy (from noise and systematics) of the sensor throughout the flight. The initial guess at each step in the grid search is based on the solution of the previous sample. This process yields the absolute gondola attitude for each time sample of the flight. However, gaps exist in this solution where absolute sensor data is not available. In addition this intermediate solution is very noisy on shortest time scales.

Filling in the Gaps

Gaps in the pointing data less than ~40 seconds long are filled with integrated gyro data and above ~50 MHz the pointing solution is strictly gyro signal. Gaps longer than ~40 seconds are flagged. The gyro data and absolute attitude data are filtered using a complementary sine-squared kernel which high pass filter the gyros and low pass filters the azimuth, pitch, roll solution from the absolute sensors. The low pass filter edges are 0.060 Hz, 0.060 Hz and 0.050 Hz for azimuth, pitch and roll respectively. The high pass filter edges are 0.080 Hz, 0.080 Hz and 0.060 Hz for azimuth, pitch and roll. Filtered high and low frequency timestreams are added together providing a final gondola attitude solution at all frequencies.

Determination of Detector RA, DEC and ψ

The elevation encoder signal is added to the gondola pitch, thereby translating gondola (outer frame) attitude into telescope (inner frame) attitude. The beam offsets for each detector are obtained from fits to the five brightest QSOs in the CMB field. Galactic and CMB source centroid offsets reveal a 0.1° shift in gondola pitch after the mid-flight ballast drop. To account for this approximately 6 hours of data during and after the ballast drop are flagged and a pitch shift is applied to all pointing data preceding the drop. The reconstructed elevation and azimuth of each beam on the sky, along with the measured polarization angles for each detector, and the GPS latitude, longitude and time are combined to determine the right ascension, declination and ψ angle for each beam. The CMB field pointing error, based on comparisons of analytical beams with observed beams, is ~2.5' in azimuth and ~1.5' in elevation. The FWHM effective beam used in final analysis is 11.5' $\pm$ 0.23.

6.3 Making I, Q and U Maps

A monochromatic plane electromagnetic wave propagating in the k-direction can be represented by

$$E_i = a_i(t)cos[\omega_0 t - \theta_i(t)]$$

$$E_j = a_j(t)cos[\omega_0 t - \theta_j(t)]$$

where $a_{i,j}$ and $\theta_{i,j}$ are the amplitudes and phases in the two transverse directions and ω_0 is the frequency of the wave. Polarization is characterized in terms of the Stokes parameters [13] which are given by,

$$I =< a_i^2 > + < a_j^2 >$$

$$Q =< a_i^2 > - < a_j^2 >$$

$$U =< 2a_i a_j cos(\theta_i - \theta_j) >$$

$$V =< 2a_i a_j sin(\theta_i - \theta_j) >$$

The quantity I is the radiation intensity, Q and U represent linear polarization and V represents circular polarization. Since CMB fluctuations are generally discussed in terms of *temperature* rather than *intensity* fluctuations the relationship $\delta I/I_0 = 4\delta T/T_0$ (derived from the Stefan-Boltzmann Law) can be use to switch from units of intensity to units of brightness temperature. Thompson scattering is not expected to generate circular polarization in the CMB and the Stokes V is zero.

The challenge of making maps from CMB data timestreams has been discussed in detail by many (for example [68], [82], [33], [81], [61], [24] and [27]). For B03 analysis the CMB polarization measurement requires the production of polarization maps, the Stokes Q and U, in addition to the usual CMB temperature maps. This section gives a

brief outline of *JIQU*, the iterative polarized map maker used in B03 analysis. A more rigorous description of *JIQU* is given in [41, 42].

The timestream data can be modeled as

$$\mathbf{d} = \mathbf{Pm} + \mathbf{n} \tag{6.4}$$

where $\mathbf{d}$ is the time-ordered data (TOD) vector and $\mathbf{n}$ is the detector noise vector, both of which are in the time domain and are the length of the number of samples in the timestream, $\mathcal{N}_T$. The term $\mathbf{m}$ represents the map triplet of the Stokes I, Q and U arranged in a vector which is in the spatial or pixel domain and is of length $3 \times \mathcal{N}_{PIX}$, where $\mathcal{N}_{PIX}$ is the number of pixels in a map. The $\mathbf{P}$ term represents the $\mathcal{N}_T \times (3 \times \mathcal{N}_{PIX})$ pointing matrix which relates pixels to time samples. The elements of P can be described by,

$$P_{tp} = \begin{cases} (1,\ \rho\cos(2\psi_t),\ \rho\sin(2\psi_t)) & \mathrm{t} \in \mathrm{p} \\ 0 & \mathrm{t} \notin \mathrm{p} \end{cases} \tag{6.5}$$

where ρ represents the detector polarization efficiency and ψ is the polarization orientation of the detector. Thus at time t the observed data coming from one detector takes the form,

$$d_t = I_t + \rho\cos(2\psi_t)Q_t + \rho\sin(2\psi_t)U_t + n_t. \tag{6.6}$$

In principle there is a calibration factor in the above equation which has been left out to simplify the notation.

Armed with a description of the polarized data for each time sample, the map-making formalism can be developed and the unknowns (the data derived signal-only and noise-only maps) in Equation 6.4 can be found. The formalism is rooted in Bayes' Theorem which states that the probability of the theory (parameters we seek) given the data is proportional to the likelihood of the data given the theory. In this case the data is the TOD and the parameters are the map triplet, $\mathbf{m}$ and the noise model, $\mathbf{n}$. This can be

written

$$P(\mathbf{m},\mathbf{n}|\mathbf{d}) \propto P(\mathbf{d}|\mathbf{m},\mathbf{n}) = \mathcal{L}(\mathbf{d}|\mathbf{m},\mathbf{n}). \tag{6.7}$$

The likelihood is maximized in order to obtain the best possible estimate of the I, Q, U maps. The likelihood expression is given by,

$$\mathcal{L}(\mathbf{d}|\mathbf{m},\mathbf{n}) = \frac{1}{|(2\pi)^{\mathcal{N}_t}\mathbf{N}|^{1/2}} \exp(-\frac{1}{2}(\mathbf{d}-\mathbf{Pm})^T\mathbf{N}^{-1}(\mathbf{d}-\mathbf{Pm})) \tag{6.8}$$

where $\mathbf{N}$ is the noise covariance matrix given by $\mathbf{N} = \mathbf{N}_{tt'} =< \mathbf{n}\mathbf{n}^T >$.

In order to make a map solution tractable, the assumptions of noise which is both Gaussian and stationary has to be made. These assumptions are valid once non-Gaussian events (spikes, turnarounds) have been removed from the timestream and the data has been divided up into chunks (over which the noise is relatively stable). For B03 the data were divided into roughly hour-long chunks, which corresponded to the time between elevation changes.

Maximizing the likelihood (Equation 6.8) with respect to the $\mathbf{m}$ is equivalent to minimizing the term in the exponential. The solution for the maximum likelihood map (see for example [82]) is given by,

$$\mathbf{m} = (\mathbf{P}^T\mathbf{N}^{-1}\mathbf{P})^{-1}\mathbf{P}^T\mathbf{N}^{-1}\mathbf{d}. \tag{6.9}$$

This expression is computationally difficult to determine since it requires inversions of rather large matrices. In addition this solution requires that the noise be known a priori, which is not the case.

The approach taken is to use iterative methods where it becomes possible to solve for both the signal-only and the noise-only maps simultaneously. A Jacobi iterator is used which has been shown to converge to the maximum likelihood solution [68]. The *kth* +

1 iteration is given by

$$\mathbf{m}^{k+1} = \mathbf{m}^k + \delta\mathbf{m}^{k+1} \tag{6.10}$$

where,

$$\delta\mathbf{m}^{k+1} = \text{diag}[\mathbf{P}^T(\mathbf{N}^k)^{-1}\mathbf{P}]^{-1}\mathbf{P}^T(\mathbf{N}^k)^{-1}(\mathbf{d} - \mathbf{P}\mathbf{m}^k) \tag{6.11}$$

is the Jacobian iterator. This correction is applied to each iteration of the signal maps until both the maps and the noise become stable.

More explicitly, setting $\mathbf{n}^k = \mathbf{d} - \mathbf{P}\mathbf{m}^k$, the last part of Equation 6.11 can be written,

$$\hat{\mathbf{n}}^k = (\mathbf{N}^k)^{-1}\mathbf{n}^k = \mathcal{F}^{-1}\left(\frac{\mathcal{F}(\mathbf{n}^k)}{\mathcal{F}(\mathbf{n}^k)^2}\right). \tag{6.12}$$

where the assumption of noise stationarity over a chunk allows the calculation to be carried out in the Fourier domain. Applying $\mathbf{P}^T$ to the filtered noise timestreams yields for each pixel,

$$\hat{n}_p^k = \sum_{t\in p} P_{pt}\hat{n}_t^k = \sum_{t\in p}\begin{pmatrix} \hat{n}_t^k \\ \rho\cos(2\psi_t)\hat{n}_t^k \\ \rho\sin(2\psi_t)\hat{n}_t^k \end{pmatrix}. \tag{6.13}$$

The first part of Equation 6.11 can be written,

$$\text{diag}[\mathbf{P}^T(\mathbf{N}^k)^{-1}\mathbf{P}]^{-1} = \text{diag}\left[\sum_{tt'} P_{pt}(N_{tt'}^k)^{-1}P_{t'p'}\right]^{-1} \tag{6.14}$$

$$= \sum_t (n_t^k)^2 M_{pp'}^{-1}\delta_{pp'} \tag{6.15}$$

where the Stokes decorrelation matrix, $M_{pp'}$, for any given pixel is

$$M_{pp'} = \sum_{t\in p} P_{pt}P_{tp'} = \sum_{t\in p}\begin{pmatrix} 1 & \rho cos(2\psi_t) & \rho sin(2\psi_t) \\ \rho cos(2\psi_t) & \rho^2 cos(2\psi_t)^2 & \rho^2 sin(2\psi_t)cos(2\psi_t) \\ \rho sin(2\psi_t) & \rho^2 cos(2\psi_t)sin(2\psi_t) & \rho^2 sin(2\psi_t)^2 \end{pmatrix}. \tag{6.16}$$

In the ideal case the decorrelation matrix is sufficient to separate I, Q and U components. In practice, however polarization efficiency, ρ, and the polarization angles, the ψs, are not sufficiently well known. In order to ensure that the Stokes parameters are uncorrelated the map-making algorithm was applied to the sum and difference of the data from a PSB pair, rather than to the individual timestreams.

The final I, Q and U maps, with 5 arcminute pixels, for the deep and shallow regions are shown in Figures 6.5 and 6.6. The Q and U maps are noise dominated. The majority of the polarization signal is derived from the deep Q and U maps.

6.4 Constructing a Noise Model

The raw noise timestreams that comprise the outputs of the map maker are not a perfect realization of detector noise. These estimates are are flawed in two ways. First, there exists an intrinsic noise bias which results from finite chunk length and finite signal-to-noise ratio, as well as any residual signal which has not been subtracted from the data timestream (see [3] and [41] for a discussion). This bias is corrected for using Monte Carlo methods. The procedure begins by performing noise estimation (running the map maker) on an ensemble of signal plus noise realizations for a given set of simulated noise PSDs. The average of the ensemble output noise estimates are then compared to the input simulated noise. This ratio represents the noise bias which is then applied as a correction factor to the best estimate noise PSD (for each detector) obtained from the real data.

Second, the detectors have correlated noise which must be taken into consideration. Auto and cross-correlated noise PSDs for B145W1 are depicted in Figure 5.1. Beginning with the (bias-corrected) noise PSDs a noise correlation matrix is constructed which contains all of the PSB pair and autocorrelated noise information at a given frequency. Taking the simple case of one PSB pair this would be:

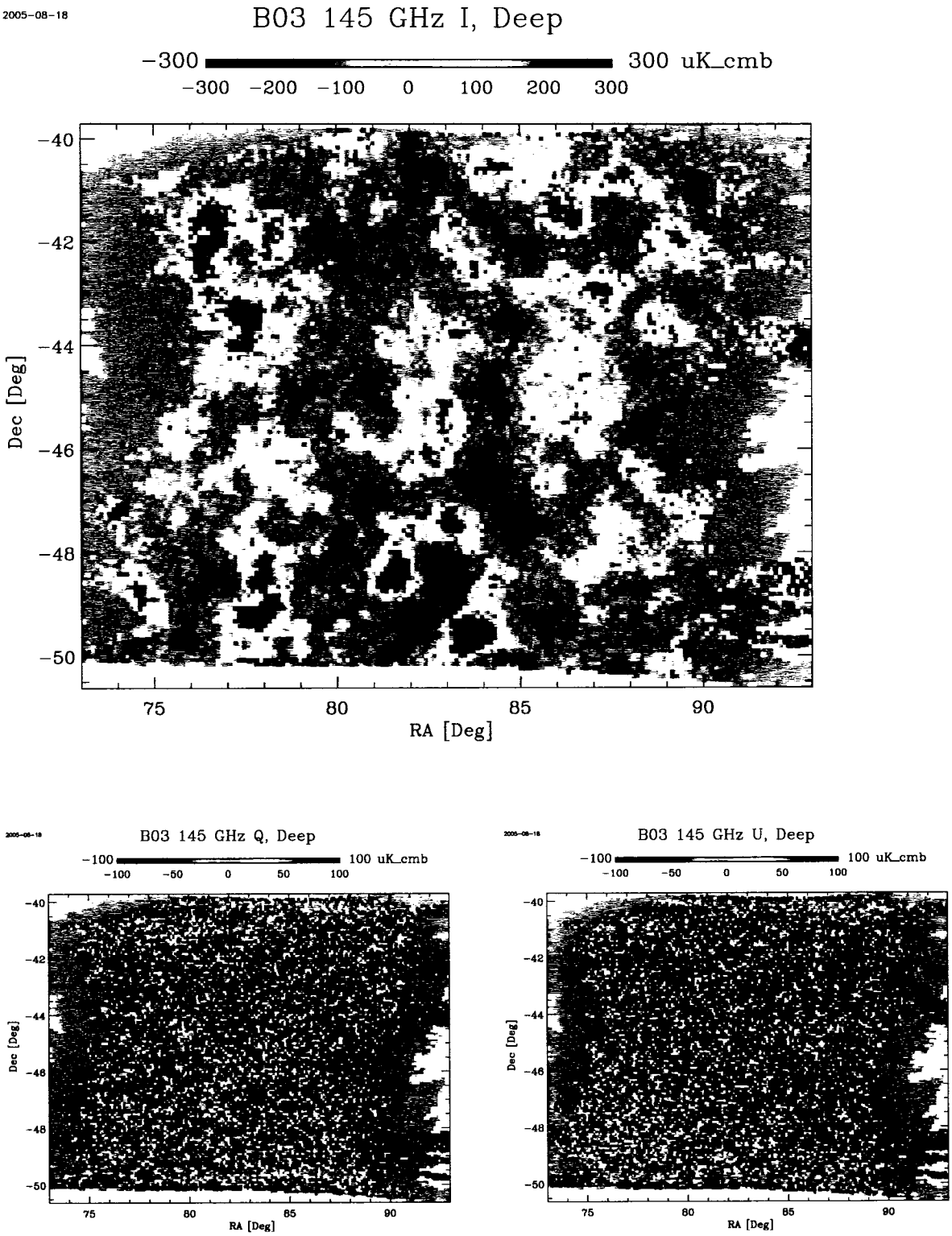

Figure 6.5: Top panel: CMB deep Stokes I map derived from all of the 145 GHz channels. Bottom panel: CMB deep Stokes Q and U maps made from the data of all eight 145 GHz channels. The polarization maps are noise dominated. The majority of the polarization signal is derived form the deep (as opposed to the shallow) Q and U maps.

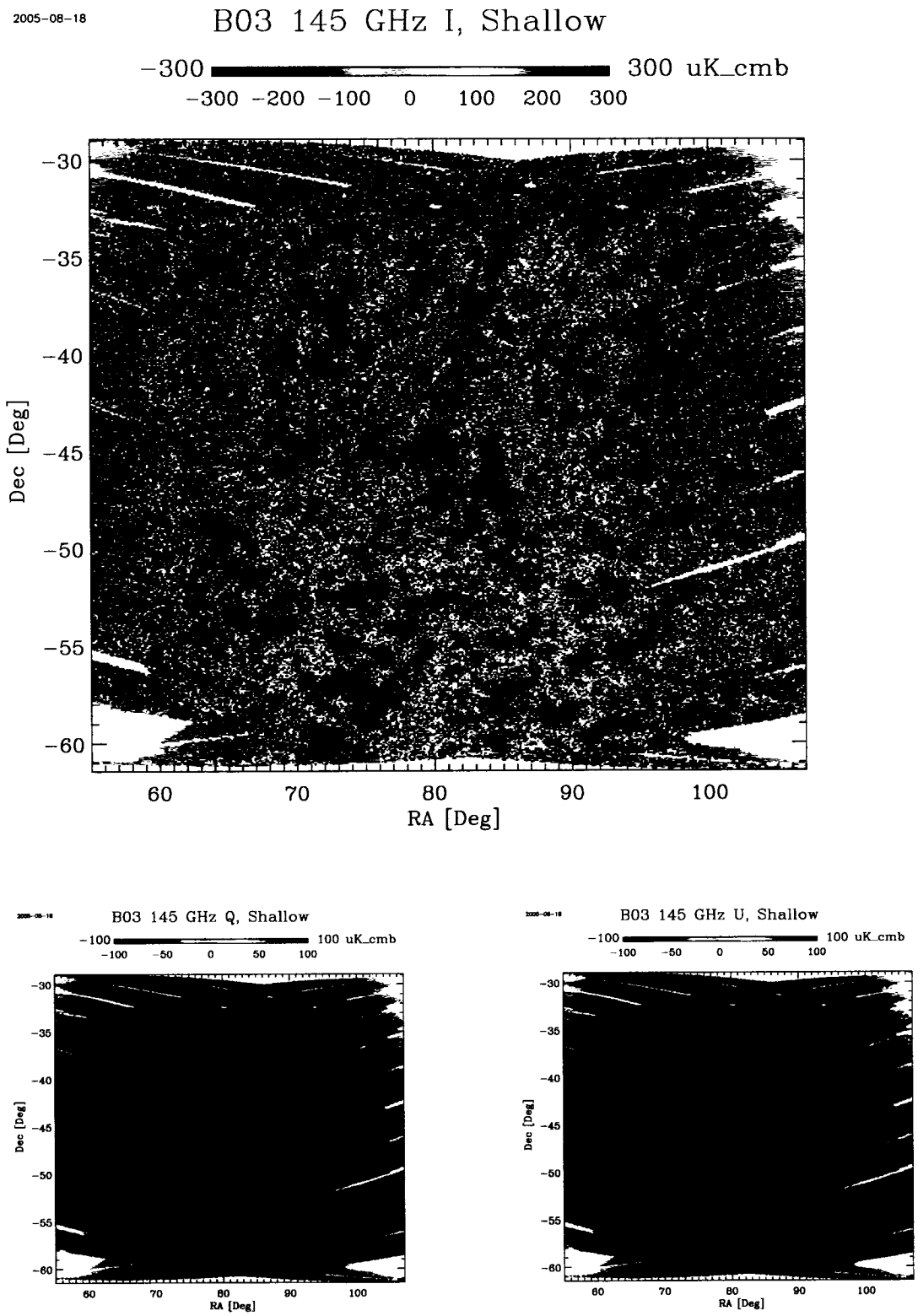

Figure 6.6: Top panel: CMB shallow Stokes I map derived from all of the 145 GHz channels. Bottom panel: CMB shallow Stokes Q and U maps made from the data of all eight 145 GHz channels. The shallow polarization maps are very noise dominated and contribute very little to the polarization signal.

$$\mathbf{C(f)} = \begin{pmatrix} < n1(f)^2 > & < n1(f)n2(f) > \\ < n2(f)n1(f) > & < n2(f)^2 > \end{pmatrix} \tag{6.17}$$

where n1 (for 'PSB1') and n2 (for 'PSB2') are the Fourier transforms of the (bias-corrected) noise estimate timestreams for two detectors and f denotes frequency domain. The Cholesky factorization of the complex (Hermitian positive definite) $\mathbf{C(f)}$ matrix is determined or $\mathbf{H(f)}$, where $\mathbf{C(f)} = \mathbf{H(f)H(f)^T}$. Next normal uncorrelated complex variates or white noise timestreams are constructed, one for each channel. For this one PSB pair example $w1(t)$ for PSB1 and $w2(t)$ for PSB2. In the final step, the Fourier transformed white noise timestreams are "rotated from the correlation space" via:

$$\mathbf{H(f)} \begin{bmatrix} w1(f) \\ w2(f) \end{bmatrix} = [N1(f), N2(f)]. \tag{6.18}$$

The above operation is performed for each frequency and the inverse Fourier transform of end products are the desired uncorrelated noise timestreams for each detector.

6.5 Making Power Spectra out of CMB Maps

This section outlines the formalism for converting T, Q, and U fluctuations in the maps into the power spectra $C_\ell^{TT}, C_\ell^{EE}, C_\ell^{BB}, C_\ell^{TE}, C_\ell^{TB}$ and C_ℓ^{EB}. This derivation of the power spectra follows [91], which is also reviewed in the HEALPix documentation [31].

The approach taken is to expand the Stokes parameters in terms of spherical harmonic components from which the power spectra can be constructed. The rotationally invariant temperature anisotropy can be directly expanded into spherical harmonics. Unlike the scalar quantity T, the Stokes Q and U depend not only on line of sight position on the sky, but also on the rotations around that position. In order to obtain rotationally invariant polarization power spectra the polarization maps are treated as combined quantities

$Q \pm iU$ and spin-weighted (spin-2) spherical harmonics [30] are used. The expansions are as follows,

$$T(\hat{\mathbf{n}}) = \sum_{lm} a_{T,lm} Y^0_{lm}(\hat{\mathbf{n}}) \tag{6.19}$$

$$(Q \pm iU)(\hat{\mathbf{n}}) = \sum_{lm} a_{\pm 2,lm} Y^{\pm 2}_{lm}(\hat{\mathbf{n}}). \tag{6.20}$$

Here, the term Y^0_{lm} represents the usual spherical harmonic functions, the term $Y^{\pm 2}_{lm}$ represents the spin-2 spherical harmonics and $\hat{\mathbf{n}}$ is the line of sight unit vector.

The expansion coefficients, a_{lm}, are the amplitude of each harmonic and are determined by multiplying the temperature or polarization distribution by the appropriate ${Y^s_{lm}}^*$ (where $*$ denotes complex conjugate) and integrating over the celestial sphere. They are given by,

$$a_{T,lm} = \int d\Omega {Y^0_{lm}}^* T(\hat{\mathbf{n}}) \tag{6.21}$$

$$a_{\pm 2,lm} = \int d\Omega Y^{\pm 2 *}_{lm} (Q \pm iU)(\hat{\mathbf{n}}). \tag{6.22}$$

The polarization expansion coefficients can be represented as another linear combination,

$$a_{E,lm} = -(a_{2,lm} + a_{-2,lm})/2 \tag{6.23}$$

$$a_{B,lm} = -i(a_{2,lm} - a_{-2,lm})/2. \tag{6.24}$$

This formalism is convenient because it introduces what are called the E-mode (curl-free) and B-mode (curl-like) polarization.

Assuming that CMB fluctuations are Gaussian, then the final power spectra which completely describe the statistics of the CMB are,

$$C_l^{AB} = \frac{1}{2l+1} \sum_m < a^{A*}_{lm} a^B_{lm} > \tag{6.25}$$

where A and B are T, E or B. Of course, the measured CMB power spectra include

instrumental effects which must be removed in order to obtain the true power spectra on the sky. To determine the final CMB spectra a Monte Carlo approach is taken.

6.5.1 The Monte Carlo Approach

The MASTER Code

The method of using Monte Carlo (MC) simulations for estimating the underlying angular power spectrum on the CMB sky was first devised for the analysis of B98 data. This method, embodied in the MASTER code [36], allowed for the first time fast estimation of the power spectrum which avoided time-consuming matrix inversions. The MASTER technique involves the direct spherical harmonic transform of the data map to what is deemed the *pseudo-*C_ℓ, which is written, $\widetilde{C}_\ell$. This is the measured spectrum, which includes instrumental effects for instance, those of incomplete sky coverage, instrument beam and experimental noise. The instrumental effects are removed from the $\widetilde{C}_\ell$ via Monte Carlo methods in order to obtain the true underlying angular power spectrum on the sky. Instrumental effects are included by characterizing the power spectrum in the following way,

$$\widetilde{C}_\ell = \sum_{\ell'} K_{\ell\ell'} F_{\ell'} B^2_{\ell'} C_{\ell'} + \widetilde{N}_\ell \tag{6.26}$$

where $K_{\ell\ell'}$ is the coupling kernel which describes the effect of windowing the sky, B_ℓ describes the instrument beam, F_ℓ is a transfer function which accounts for any filtering applied to the data, $C_{\ell'}$ is the true full sky angular power spectrum and $\widetilde{N}_\ell$ is the noise power spectrum. Note that, at this point, the formalism does not include polarization details. The discussion is extended to include polarization spectra in Section 7.1.1.

The transfer function, F_ℓ and noise term, $\widetilde{N}_\ell$, are both determined via MC methods. Noise-only timestreams are simulated based on the noise estimation method of Section 6.4. These simulated noise-only timestreams are projected onto the sky with the actual instrument scanning strategy, making a noise-only map which is subsequently

transformed into noise-only power spectra. The $\widetilde{N}_\ell$ is derived from the ensemble average of $\sim$ 400 noise realizations. The transfer function is derived from signal-only MC simulations. From a known input C_ℓ, $\sim$ 200 signal-only power spectra are derived. The signal-only version of Equation 6.5.1 may then be used to calculate F_ℓ. In practice, to avoid inversion of the coupling kernel matrix, $K_{\ell\ell'}$, an iterative method is employed to solve for F_ℓ.

It is conventional to bin the power spectrum multipoles into a number of bands. The binned full-sky power spectrum can be written,

$$\widehat{C}_b = K^{-1}_{bb'} P_{b'\ell} \left(\widetilde{C}_\ell - \langle \widetilde{N}_\ell \rangle \right) \tag{6.27}$$

where the $P_{b\ell}$ operator relates bins to multipoles through, $C_b = P_{b\ell} C_\ell$. The term $K_{bb'}$ is a binned version of the coupling matrix given by,

$$\widehat{K}_{bb'} = P_{b\ell} K_{\ell\ell'} F_{\ell'} B^2_{\ell'} Q_{\ell' b} \tag{6.28}$$

where $Q_{\ell b}$ is simply the reciprocal of the $P_{b\ell}$ operator such that $C_\ell = Q_{\ell b} C_b$.

The uncertainties in the final binned power spectra estimates are also obtained using MC simulations. In this case signal plus noise simulations are generated and Equation 6.5.1 is applied to each. The covariance matrix for the binned power spectrum is given by,

$$\widehat{C}_{bb'} = \langle \left(\widehat{C}_b - \langle \widehat{C}_b \rangle \right) - \left(\widehat{C}_{b'} - \langle \widehat{C}_{b'} \rangle \right) \rangle. \tag{6.29}$$

The diagonal elements of $C_{bb'}$ can then be used to represent the uncertainties in the final binned spectra bandpowers. While the formalism introduced above for MASTER has the advantage of being relatively simple, the disadvantage of this time consuming final step (the generation of signal plus noise Monte Carlo simulations for uncertainty estimation) lead to the development of MASTER's successor, FASTER.

The FASTER and XFASTER Codes

The FASTER and XFASTER methods are described in detail in [18]. A brief overview is given in this section.

The FASTER technique is rooted in Bayesian statistics. The assumption is made that the true signal on the sky is drawn from a Gaussian distribution. The CMB likelihood is then the convolution of the true sky signal probability distribution with the probability distribution of the map and is written,

$$\mathcal{L}(\mathbf{a}|\mathbf{z}) = \frac{1}{|(2\pi)^{N/2}\mathbf{C}|^{1/2}} \exp(-\frac{1}{2}\mathbf{a}^{\rm obs} \cdot \mathbf{C}^{-1} \cdot \mathbf{a}^{\rm obs\dagger}) \tag{6.30}$$

where $\mathbf{a}^{\rm obs}$ are the observed spherical harmonic coefficients , $\mathbf{C}$ is the total theory signal plus noise covariance matrix described by, $\mathbf{C}(\mathbf{z}) = \mathbf{S}(\mathbf{z}) + \mathbf{N}$ and $\mathbf{z}$ is a set of model C_ℓ parameters. The location in (ℓ, m) space where the likelihood function is a maximum or where,

$$\left.\frac{\partial \mathcal{L}}{\partial C_\ell}\right|_{C_\ell = C_\ell^{max}} = 0 \tag{6.31}$$

is the desired quantity. The solution, derived in [9], is

$$C_\ell^{max} = \frac{1}{2}\sum_{\ell'} F_{\ell\ell'}^{-1} {\rm Tr}\left[\mathbf{C}^{-1} \cdot \frac{\partial \mathbf{S}}{\partial C_{\ell'}} \cdot \mathbf{C}^{-1} \cdot (\mathbf{C}^{\rm obs} - \mathbf{N})\right] \tag{6.32}$$

where the elements of the matrix $\mathbf{C}^{\rm obs}$ are given by $C^{\rm obs}_{\ell m,\ell' m'} = a^{\rm obs}_{\ell m} a^{\rm obs}_{\ell' m'}$. The term $F^{-1}_{\ell\ell'}$ is the inverse Fisher information matrix which essentially gives a measure of how fast the likelihood distribution falls away from the maximum. It is determined by the expression,

$$F_{\ell,\ell'} = \frac{1}{2}{\rm Tr}\left[\frac{\partial \mathbf{S}}{\partial C_{\ell'}} \cdot \mathbf{C}^{-1} \cdot \frac{\partial \mathbf{S}}{\partial C_{\ell'}} \mathbf{C}^{-1}\right]. \tag{6.33}$$

Further simplifications can be made to avoid matrix inversion and speed up compu-

tation. As with the MASTER technique isotropy is assumed both in the noise term and in the underlying sky signal and the spectra are summed into bands. The cut-sky model power spectrum, $\widetilde{C}_\ell^{mod}$, is parameterized with respect to the full-sky spectrum through,

$$\widetilde{C}_\ell^{mod} = \sum_{\ell'} K_{\ell\ell'} B_{\ell'}^2 F_{\ell'} C_{\ell'}^{(S)} q_{\ell'} \tag{6.34}$$

where q_ℓ is the quadratic estimator and in this form represents the deviation from a template 'shape' full-sky spectrum $C_\ell^{(S)}$. $K_{\ell\ell'}$, B_ℓ and F_ℓ are the coupling kernel, beam and transfer function as in Equation 6.5.1. In terms of bandpowers the pseudo power spectrum expression becomes,

$$\widetilde{C}_\ell^{mod} = \sum_b q_b \widetilde{C}_{b\ell}^{(S)} \equiv \sum_b q_b \sum_{\ell'} K_{\ell\ell'} B_{\ell'}^2 F_{\ell'} C_{\ell'}^{(S)} \chi_b(\ell') \tag{6.35}$$

with the binning function $\chi_b(\ell) = 1$ within a band and $\chi_b(\ell) = 0$ outside the band. The bandpower deviation, q_b, has maximum likelihood solution given by,

$$q_b^{max} = \frac{1}{2} \sum_{b'} F_{bb'}^{-1} \sum_\ell (2\ell+1) g_\ell \frac{\widetilde{C}_{b'\ell}^{(S)}}{(\widetilde{C}_\ell^{mod} + \langle \widetilde{N}_\ell \rangle)^2} (\widetilde{C}_\ell^{obs} - \langle \widetilde{N}_\ell \rangle). \tag{6.36}$$

The g_ℓ term describes the number of degrees of freedom effectively available in the cut-sky observation [36] and is given by $g_\ell = f_{sky} w_2^2 / w_4$, where f_{sky} is the fraction of the sky observed, and w_i is the i-th moment of the weighted mask applied to the data. The bandpower Fisher matrix is given by,

$$F_{bb'} = \frac{1}{2} \sum_\ell (2\ell+1) g_\ell \frac{\widetilde{C}_{b\ell}^{(S)} \widetilde{C}_{\ell b'}^{(S)}}{(\widetilde{C}_\ell^{mod} + \langle \widetilde{N}_\ell \rangle)^2}. \tag{6.37}$$

An iterative approach is used to obtain the maximum likelihood q_b. After starting with an initial arbitrary guess for q_b, the bandpower Fisher matrix Equation 6.5.1 and

q_b Equation 6.5.1 are iterated until the q_b estimate stabilizes. Uncertainties in the final bandpower spectrum are determined directly from the inverse of the Fisher information matrix.

In addition to spectral bandpowers and uncertainties, the FASTER program also calculates window functions and noise offsets. The former is an operator for obtaining theoretical bandpowers from model power spectra. The latter can be used to account for non-Gaussian behavior in the bandpowers caused by the effect of *cosmic bias*. Both are required products for parameter estimation and are discussed further in Section 7.1.1.

The discussion of the pseudo-$\widetilde{C}_\ell$ has been fairly general so far. There are in fact six spectra to be calculated. In the FASTER formalism they are,

$$\begin{aligned}
\widetilde{C}_\ell^{TT} &= \textstyle\sum_b q_b^{TT} \sum_{\ell'} K_{\ell\ell'} B_{\ell'}^2 F_{\ell'}^{TT} C_{\ell'}^{(S)TT} \chi_b(\ell) + \widetilde{N}_\ell^{TT} \\
\widetilde{C}_\ell^{EE} &= \textstyle\sum_b \Big(q_b^{EE} \sum_{\ell'} {}_+K_{\ell\ell'} B_{\ell'}^2 F_{\ell'}^{EE} C_{\ell'}^{(S)EE} \chi_b(\ell) + q_b^{BB} \sum_{\ell'} {}_-K_{\ell\ell'} B_{\ell'}^2 F_{\ell'}^{BB} C_{\ell'}^{(S)BB} \chi_b(\ell) \Big) + \widetilde{N}_\ell^{EE} \\
\widetilde{C}_\ell^{BB} &= \textstyle\sum_b \Big(q_b^{BB} \sum_{\ell'} {}_+K_{\ell\ell'} B_{\ell'}^2 F_{\ell'}^{BB} C_{\ell'}^{(S)BB} \chi_b(\ell) + q_b^{EE} \sum_{\ell'} {}_-K_{\ell\ell'} B_{\ell'}^2 F_{\ell'}^{EE} C_{\ell'}^{(S)EE} \chi_b(\ell) \Big) + \widetilde{N}_\ell^{BB} \\
\widetilde{C}_\ell^{TE} &= \textstyle\sum_b q_b^{TE} \sum_{\ell'} {}_\times K_{\ell\ell'} B_{\ell'}^2 F_{\ell'}^{TE} C_{\ell'}^{(S)TE} \chi_b(\ell) + \widetilde{N}_\ell^{TE} \\
\widetilde{C}_\ell^{TB} &= \textstyle\sum_b q_b^{TB} \sum_{\ell'} {}_\times K_{\ell\ell'} B_{\ell'}^2 F_{\ell'}^{TB} C_{\ell'}^{(S)TB} \chi_b(\ell) + \widetilde{N}_\ell^{TB} \\
\widetilde{C}_\ell^{EB} &= \textstyle\sum_b q_b^{B} \sum_{\ell'} {}_\times K_{\ell\ell'} B_{\ell'}^2 F_{\ell'}^{EB} C_{\ell'}^{(S)EB} \chi_b(\ell) + \widetilde{N}_\ell^{EB}
\end{aligned} \tag{6.38}$$

Note that distinct transfer functions and noise terms are calculated for each polarization type. The ${}_{+,\times}K_{\ell\ell'}$ terms are the polarization mask coupling kernels. The full polarized version of each multipole's covariance can be written,

$$\widetilde{\mathbf{D}}_\ell = \begin{pmatrix} \widetilde{C}_\ell^{TT} & \widetilde{C}_\ell^{TE} & \widetilde{C}_\ell^{TB} \\ \widetilde{C}_\ell^{TE} & \widetilde{C}_\ell^{EE} & \widetilde{C}_\ell^{EB} \\ \widetilde{C}_\ell^{TB} & \widetilde{C}_\ell^{EB} & \widetilde{C}_\ell^{BB} \end{pmatrix}. \tag{6.39}$$

Thus, the polarized version of the quadratic estimator takes the form,

$$q_b^{max} = \frac{1}{2}\sum_{b'} F_{bb'}^{-1} \sum_{\ell}(2\ell+1)g_\ell \mathrm{Tr}\left[\widetilde{\mathbf{D}}_\ell^{-1}\cdot\frac{\widetilde{\mathbf{S}}_\ell}{\partial q_{b'}}\cdot\widetilde{\mathbf{D}}_\ell^{-1}(\widetilde{\mathbf{D}}_\ell^{obs}-\widetilde{\mathbf{N}}_\ell)\right]. \tag{6.40}$$

where the noise matrix, $\mathbf{N}_\ell$ is defined similarly to $\widetilde{\mathbf{D}}_\ell$. The polarized version of the Fisher matrix is,

$$F_{bb'} = \frac{1}{2}\sum_{\ell}(2\ell+1)g_\ell \mathrm{Tr}\left[\widetilde{\mathbf{D}}_\ell^{-1}\cdot\frac{\widetilde{\mathbf{S}}_\ell}{\partial q_{b'}}\cdot\widetilde{\mathbf{D}}_\ell^{-1}\cdot\frac{\widetilde{\mathbf{S}}_\ell}{\partial q_{b'}}\right]. \tag{6.41}$$

The form of the signal matrix derivatives, $\frac{\widetilde{\mathbf{S}}_\ell}{\partial q_{b'}}$, depend on the polarization type of a particular band. For example for a TE band this term becomes,

$$\frac{\widetilde{\mathbf{S}}_\ell}{\partial q_b^{TE}} = \begin{pmatrix} 0 & \sum_{\ell'}\times K_{\ell\ell'}B_{\ell'}^2 F_{\ell'}^{TE} C_{\ell'}^{(S)TE}\chi_b(\ell) & 0 \\ \sum_{\ell'}\times K_{\ell\ell'}B_{\ell'}^2 F_{\ell'}^{TE} C_{\ell'}^{(S)TE}\chi_b(\ell) & 0 & 0 \\ 0 & 0 & 0 \end{pmatrix}. \tag{6.42}$$

The fact that B03 dataset produces a distinct set of shallow and deep maps, necessitates the evolution of FASTER to XFASTER; a program which includes all of the auto and cross-spectrum components from a set of maps in order to consistently estimate the spectral bandpowers. The full set of auto and cross spectra for the multi-map treatment can be summarized as,

$$C_l^{AB,IJ} = \frac{1}{2l+1}\sum_m < a_{lm}^{A*,I} a_{lm}^{B,J} > \tag{6.43}$$

where again A and B are T, E or B, and now I and J correspond to the deep or shallow region maps. The full covariance matrix for each multipole which includes all of the auto

and cross-spectrum components takes the form,

$$\widetilde{\mathbf{D}}_\ell = \begin{pmatrix} \widetilde{\mathbf{D}}_\ell^{\mathrm{deep\times deep}} & \widetilde{\mathbf{D}}_\ell^{\mathrm{deep\times shall}} \\ \widetilde{\mathbf{D}}_\ell^{\mathrm{shall\times deep}} & \widetilde{\mathbf{D}}_\ell^{\mathrm{shall\times shall}} \end{pmatrix}. \tag{6.44}$$

For XFASTER distinct transfer functions are determined for each polarization type *and* map-to-map correlation. More explicitly the transfer function term F_ℓ^{AB} extends to $F_\ell^{AB,IJ}$. In addition separate mask coupling kernels are calculated for each map-to -map correlation such that $K_\ell \rightarrow K_\ell^{IJ}$. The form of the XFASTER estimator is identical to Equation 6.5.1 for FASTER. For XFASTER however, all quantities include a map-to-map correlation index.

6.6 The B03 CMB Spectra

The six B03 CMB angular spectra are shown in Figures 6.7-6.9. The model plotted is a best fit to WMAP(first-year)+CBI+ACBAR data [79]. The agreement of the data with this model is apparent. The bandpowers for the spectra are also given in Table 6.1.

6.6.1 Instrumental Systematics Tests

Jackknifes

Two sets of jackknife tests are performed, whereby the timestream is divided into two subsets from each of which I, Q and U maps are made. These subset maps are then differenced and the power spectra of the differenced maps are computed. If the difference spectrum is consistent with zero the jackknife test is considered a pass. The first jackknife test splits the data in time, comparing the first half of the shallow and first half of the deep with the second half of the shallow and second half of the deep. This temporal jackknife gives a good gauge of time-varying systematic effects such as pointing accuracy, effects

ℓ_b^{TT}	C_b^{TT}	ΔC_b^{TT}	ℓ_b^{TE}	C_b^{TE}	ΔC_b^{TE}	ℓ_b^{TB}	C_b^{TB}	ΔC_b^{TB}
75	2265	386	150	-51	27	150	-18	27
125	4075	445	250	40	32	250	-8.7	31
175	5220	453	350	58	28	350	-16	27
225	5477	428	450	-90	29	450	6.5	28
275	5194	367	550	40	39	550	-2.5	35
325	3157	223	650	-18	45	650	-1.9	42
375	1827	139	750	-86	60	750	-88	58
425	1834	132	850	62	74	850	74	72
475	2127	145	950	-61	90	950	-70	88
525	2315	155	-	-	-	-	-	-
575	2370	159	-	-	-	-	-	-
625	1805	142	-	-	-	-	-	-
675	1660	145	-	-	-	-	-	-
725	2053	173	-	-	-	-	-	-
775	2388	203	-	-	-	-	-	-
825	1888	207	-	-	-	-	-	-
875	1902	227	-	-	-	-	-	-
925	1468	235	-	-	-	-	-	-
975	8558	234	-	-	-	-	-	-
1025	1004	273	-	-	-	-	-	-
1075	9948	324	-	-	-	-	-	-
1125	1229	382	-	-	-	-	-	-
1225	7707	238	-	-	-	-	-	-
1400	1245	465	-	-	-	-	-	-

ℓ_b^{EE}	C_b^{EE}	ΔC_b^{EE}	ℓ_b^{BB}	C_b^{BB}	ΔC_b^{BB}	ℓ_b^{EB}	C_b^{EB}	ΔC_b^{EB}
150	3.3	3.2	150	1.2	2.4	150	-1.8	2.1
250	4.3	4.2	250	1.6	3.2	250	-1.5	2.7
350	15.3	7.4	350	5.3	5.8	350	-7.6	4.8
450	6.3	9.3	450	-1.5	8.1	450	-6.6	6.3
600	29.5	12.1	600	-4.0	9.3	600	-1.1	7.6
800	57.0	28.6	800	19.7	25.2	800	-9.1	19.1
1000	30.2	72.1	1000	16.3	69.4	1000	122	50.4

Table 6.1: Bandpowers for the B03 TT, TE, TB, EE, BB and EB angular power spectra. For each spectrum there are three columns; the first is the central multipole value for each band, the second and third columns are the bandpowers and errors in units of μK^2.

of altitude changes and atmospheric contamination. The second jackknife test splits the data into subsets from each half of the focal plane. One subset consists of data from the channels 145W1, 145W2, 145X1 and 145X2 and the other subset from 145Y1, 145Y2, 145Z1 and 145Z2.

The jackknife results are presented in Table 6.2, where the number of degrees of freedom (DOF) and χ^2 (of jackknife to zero) value for each spectrum jackknife are given. The "probability to exceed" values are given for a more quantitative result and are calculated from the integral

$$PTE = \frac{2}{2^{(DOF/2)}\Gamma(DOF/2)} \int_{\chi}^{\infty} x^{DOF-1} e^{-x^2/2} dx. \tag{6.45}$$

If the PTE value is large then the observed jackknife and expected distribution (zero) are consistent. The convention is followed that if the PTE value is less than 5% then the disagreement is said to be significant. All but the TT temporal jackknifes are remarkably consistent with zero. The TT temporal jackknife failure is significant but with very small amplitude which is evident in Figure 6.7 where the amplitude of the jackknife spectrum is small compared to the bandpower uncertainties. Given that the channel TT jackknife is a pass, the failure of the TT temporal jackknife is believed to be caused by unpolarized atmospheric contamination which would be more prominent at lower altitudes (pre-ballast drop).

Propagation of Instrumental Uncertainties

In addition to the jackknife tests the effect of mis-estimation of several instrumental uncertainties on the final spectra is examined. The instrumental parameters and corresponding uncertainties that are investigated include the beam size (±2%), relative calibration (±0.8%), PSB orientation or polarization angle (±2°), the bolometer time constants (±10%), and PSB polarization efficiency (±3%). A full description of the de-

termination of instrumental uncertainties is given in [57]. The effect of mis-estimation is determined from 145 simulated signal-only timestreams which are generated varying an instrumental uncertainty parameter around its nominal value. The simulated timestreams are then analyzed with the measured parameter value and a systematic error bar is deduced from the standard deviation of the simulated results. The errors from the mis-estimation instrumental uncertainties are determined to be insignificant for B03. Further details can be found in [43, 67, 60].

Spectrum		DOF	χ^2	PTE (%)
Channel Jackknife	TT	24	20.6	66
	TE	9	10.6	30
	TB	9	12.3	20
	EE	7	5.7	58
	BB	7	6.3	51
	EB	7	5.3	62
Temporal Jackknife	TT	24	58.9	< 1
	TE	9	12.2	20
	TB	9	13.1	16
	EE	7	7.2	41
	BB	7	3.0	89
	EB	7	2.9	89

Table 6.2: Temporal and channel jackknife results for each power spectrum. First column is the number of degrees of freedom and second column is χ^2 (of jackknife to zero) value for each spectrum jackknife. The "probability to exceed" values are given for a more quantitative result. The TT temporal jackknife failure is significant but with very small amplitude as is evident in Figure 6.7.

6.6.2 Foregrounds

While microwave observations of the Interstellar Medium (ISM) and Intergalactic Medium (IGM) can be interesting science in themselves, for CMB measurement they represent undesirable foregrounds. Bright foreground point sources, which have the effect of adding power to the final CMB spectra, are easily identifiable and simply cut from the maps.

Accounting for diffuse galactic dust is more complicated. The full details and further discussion of foreground analysis can be found in [57, 43, 60, 67]. An overview of the method and results is given here.

Figure 6.10 taken from [83] summarizes the foreground emission in terms of frequency versus scale. Coloured regions indicate parts of frequency-multipole space where the foreground fluctuations exceed the CMB fluctuations. The most threatening foreground at B03 frequency and scale is the vibrational dust emission. Fortunately, the dust spectrum is expected to have considerable emission on the infrared, and hence spatial correlation of maps from infrared surveys with B03 CMB maps should allow for differentiation between dust contamination and the CMB signal. Cross-correlation of the B03 145 GHz maps with the Schlegel-Finkbeiner-Davis (SFD) [28] 100 μm dust map was performed. The analysis finds no statistically significant correlation between the B03 Stokes I maps (deep and shallow) and the dust maps. The B03 245 GHz and 345 GHz maps however, do exhibit spatial correlations with the dust map, as one might expect given Figure 6.10.

Polarized foregrounds are predicted to equally contaminate the E and B components of the CMB [83]. A good test of the contamination to the TE CMB spectrum is the lack of power in the TB spectrum. Figure 6.9 clearly indicates this to be the case, with the TB data giving a χ^2 to zero of 4.9/(9 DOF). Further evidence that the E and B signal are not contaminated comes from the cross-correlation of the B03 145 GHz data with IRAS dust intensity maps. The products $< T_{IRAS} B_{B03} >$ and $< T_{IRAS} E_{B03} >$ are found to be statistically consistent with zero, providing further evidence that the B03 E and B polarization signal are indeed coming from the CMB. See [57] for further details.

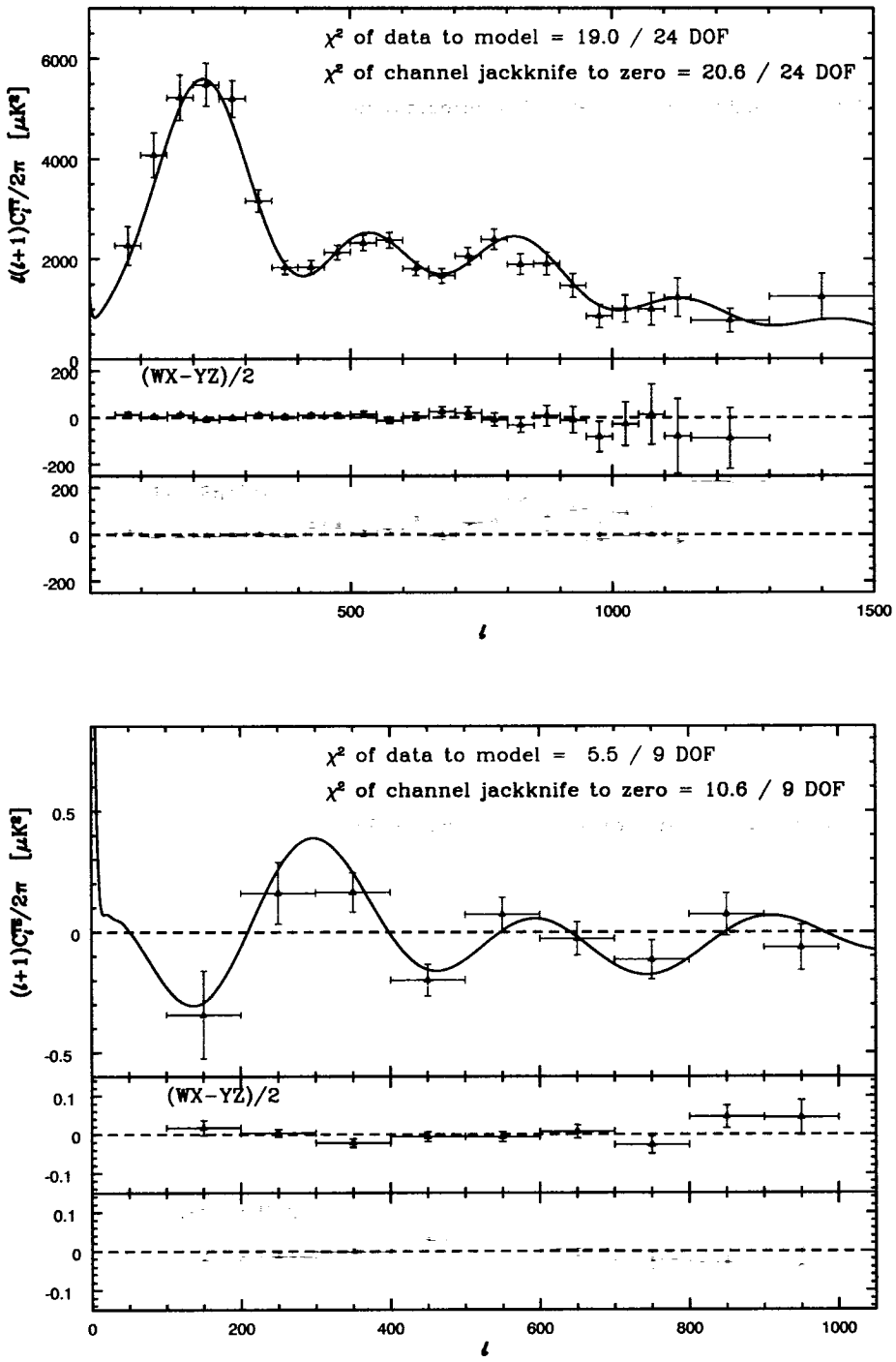

Figure 6.7: B03 TT and TE angular power spectra and jackknife data. The TT temporal jackknife failure is significant but with very small amplitude. All other jackknifes are consistent with zero. Model plotted (solid curve) is a best fit to WMAP(first-year)+CBI+ACBAR data from `http://lambda.gsfc.nasa.gov/product/map/` and is in very good agreement with the data.

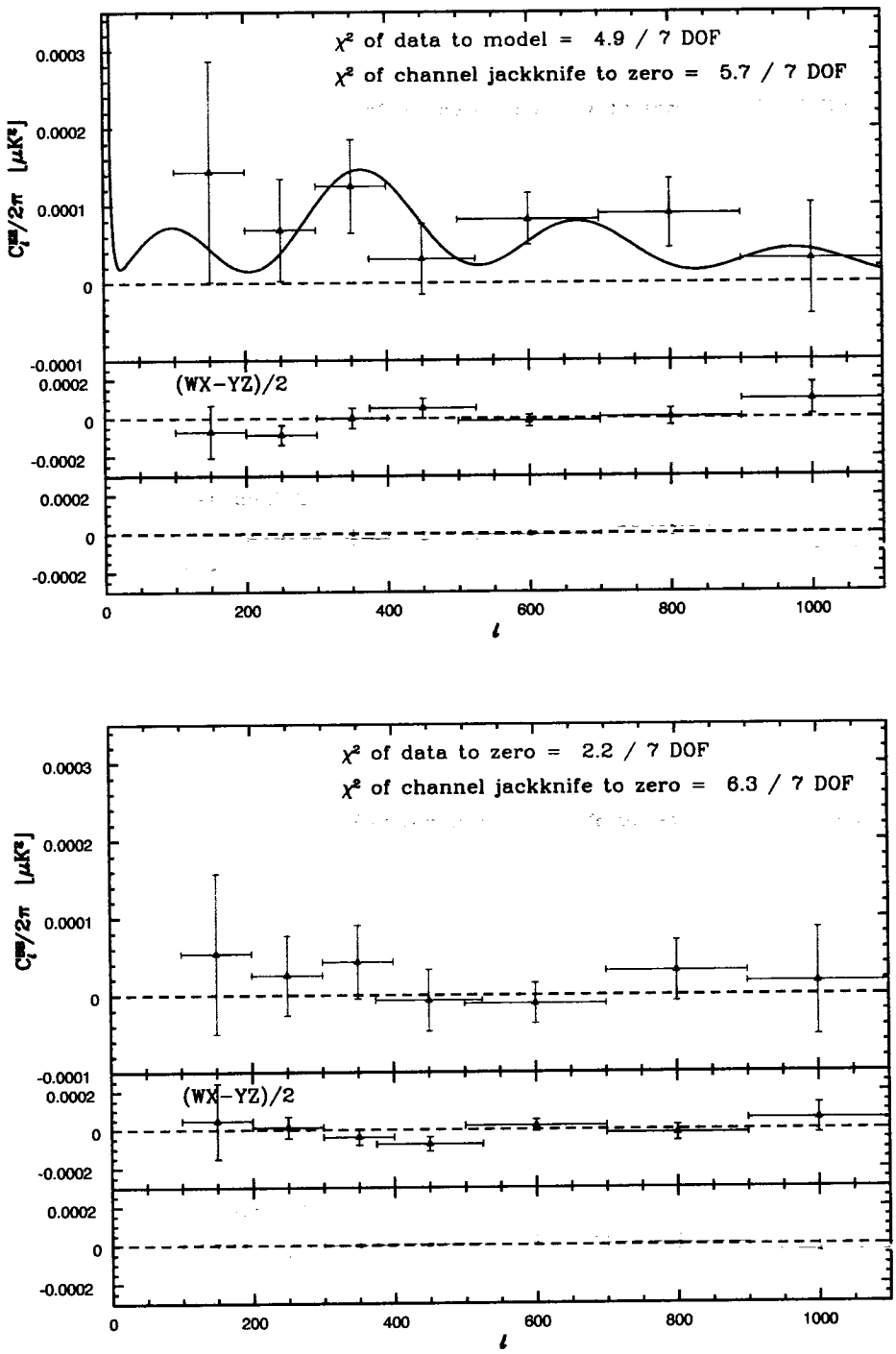

Figure 6.8: B03 EE and BB angular power spectra and jackknife data. Jackknifes are consistent with zero. Model plotted (solid curve) is a best fit to WMAP(first-year)+CBI+ACBAR data from `http://lambda.gsfc.nasa.gov/product/map/` and is in very good agreement with the EE data. The BB spectrum is consistent with zero. B-mode polarization is predicted to be at least one order of magnitude lower than E-mode polarization.

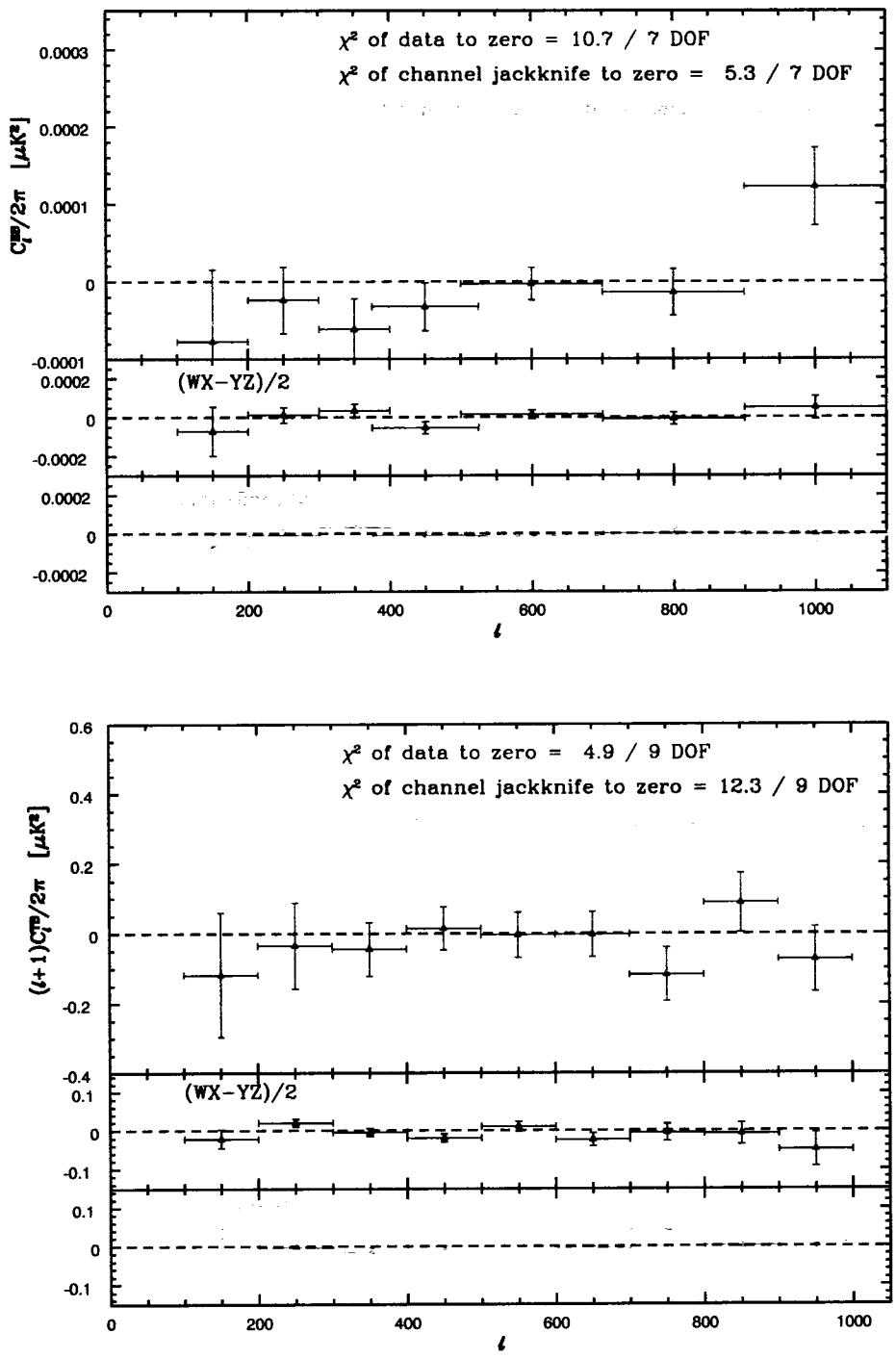

Figure 6.9: B03 TB and EB angular power spectra and jackknife data. Jackknifes are consistent with zero. Polarized foregrounds are predicted to equally contaminate the E and B. A good test of the foreground contamination to the TE and EE CMB spectrum is the lack of power in the TB and EB spectra.

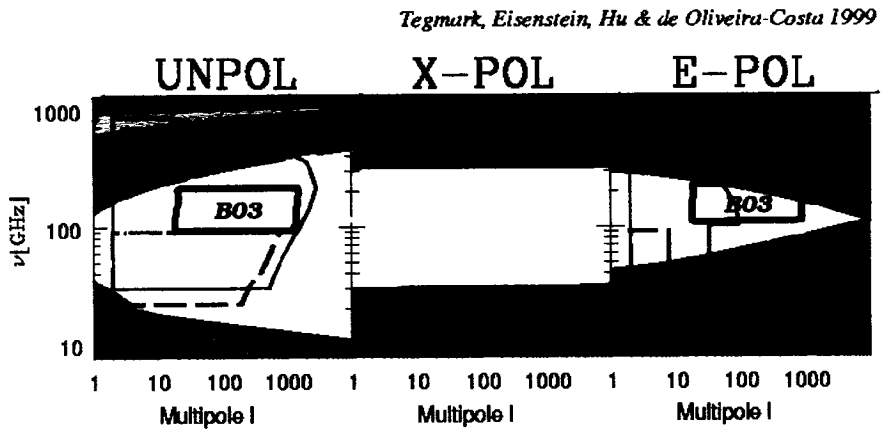

Figure 6.10: Realistic predicted CMB foregrounds, in frequency-multipole space, derived from [83]. Coloured regions indicate parts of frequency-multipole space where the foreground fluctuations exceed the CMB fluctuations. Box labeled B03 indicates the observing frequency and scale of BOOMERANG 2003 from which the final B03 power spectra are derived. The larger boxes are the parameter space for Planck observation (thin black lines) and WAMP observation (dashed lines). The most threatening foreground, fluctuating at the CMB fluctuation level, at B03 frequency and scale is the vibrational dust emission (red). Other foregrounds include synchrotron (magenta), free-free (cyan) and rotational dust emission (blue).
See [83] for details.

Chapter 7

Cosmological Parameters B03

This chapter is based largely on [54][1] and examines in detail the cosmological implications of the B03 data set. The required data products and methodology for parameter extraction are outlined in Section 7.1. Section 7.2 describes the various data combinations that are used in this analysis. Section 7.3.1 focuses on the standard ΛCDM model and, applying only weakly restrictive priors it is found that the simple parameter fits to B03 data alone are fully consistent with those derived from other existing CMB data. To this CMB data, including the B03 data, the recent Large Scale Structure (LSS) redshift survey data, consisting of matter power spectra from the Sloan Digital Sky Survey (SDSS) [84] and the 2 Degree Field Galaxy Redshift Survey (2dFGRS) [65] is added, and the marginalized parameter constraints from this combined cosmological data set are determined. In Section 7.3.2 the analysis is extended to include tests of several modifications of the standard model with the combined data sets. All of the models in Section 7.3 share the assumption that the initial perturbations of the primordial plasma are adiabatic. In Section 7.4 the constraints of the B03 and other data on a model with a mixture of a dominant adiabatic mode and a sub-dominant isocurvature mode are explored.

[1] AAS has been notified and all obligations for release of copyright have been fulfilled.

7.1 Data Products and Methodology

7.1.1 Summary of B03 Results

The parameter constraints presented in this analysis are based on the data outputs of the XFASTER hybrid Monte Carlo–maximum likelihood estimator [18][2]. The estimator uses a close to optimal, quadratic, Fisher matrix-based estimator which is calibrated using signal-only and noise-only simulations of the entire data set, from time stream to final maps. The XFASTER formalism is reviewed in Section 7.1.1. It determines true polarization and total temperature angular power spectra (averaged over pre-determined ℓ bands) on the sky. After an arbitrary initial guess, the quadratic estimator iterates onto the maximum likelihood solution [9], $C_B^{\rm dat}$, with errors determined by an estimate of the Fisher matrix for all band powers self-consistently.

The calculation of the full Fisher matrix also allows us to exclude band powers self consistently by cutting rows and columns from the inverse Fisher matrix. The effect of reduced sky coverage and/or pixel weighting is accounted for by computing all coupling kernels following [36] and [16]. The analysis typically includes a simultaneous determination of a complete set of TT, EE, BB, TE, TB, and EB band powers. The EB and TB spectra are consistent with zero (as expected) and are excluded from the parameter determination by cutting out the bands in the inverse Fisher matrix (equivalent to marginalizing over their contribution).

The spectra used in this analysis are shown in Figure 7.1. The data have been divided into bands which are generally $\Delta\ell = 50$ wide for TT and $\Delta\ell = 100$ wide for the three remaining spectra. The multipole ranges for the B03 spectra which are used in this analysis are presented in Table 7.1. All band-to-band correlations are included in the Fisher information matrix and are at most ~20%. The band spacing was chosen in part

[2] http://cmb.phys.cwru.edu/boomerang
http://oberon.roma1.infn.it/boomerang/b2k

B03 Spectrum	Multipole Range	Number of Bands	Reference
TT	$75\ (375) \leq \ell \leq 1400$	24 (18)	[43]
TE	$150 \leq \ell \leq 950$	9	[67]
EE & BB	$150 \leq \ell \leq 1000$	7	[60]

Table 7.1: B03 bandpowers. The lowest bandpowers of the TT spectrum ($\ell < 375$) are excluded when combining the B03 data with the WMAP results since the two spectra are signal dominated and therefore correlated.

to ensure that these correlations were not large.

The XFASTER code also calculates the required band window functions, W_ℓ^B, which are used to convert the model power spectra, $C_\ell^{\rm mod}$, into theoretical bandpowers via

$$\langle C_B^{\rm mod} \rangle = \frac{\mathcal{I}[W_\ell^B \mathcal{C}_\ell^{\rm mod}]}{\mathcal{I}[W_\ell^B]} \tag{7.1}$$

Here $\mathcal{C}_\ell^{\rm mod} = \ell(\ell+1)C_\ell^{\rm mod}/2\pi$ and the notation for the "logarithmic integral" of a spectrum [9] is given by $\mathcal{I}[f_\ell] \equiv \sum_\ell \frac{\ell+\frac{1}{2}}{\ell(\ell+1)} f_\ell$. The above operation permits direct comparison of theory $C_B^{\rm mod}$ with data $C_B^{\rm dat}$.

A final issue is the potential bias introduced by the non-Gaussian distribution of the bandpowers in the signal-dominated regime. It has been shown [9] that the variable $Z_B = \ln(C_B^{\rm dat} + C_B^N)$ is more normally distributed than the bandpowers C_B. The noise offsets, C_B^N, are a measure of the deconvolved noise spectrum on the sky and are calculated with the same quadratic estimator using XFASTER on the average of simulated noise-only observations.

The distribution of the bandpowers tends to a Gaussian in the noise-dominated regime and log-normal in the sample-variance-dominated regime. Both limits are significant for the TT bandpowers, hence all the TT bands are transformed to offset log-normal variables and the likelihood function is treated in the new variables as Gaussian for parameter estimation. For the polarization spectra EE and BB, which are noise-dominated, $Z_B = C_B^{\rm dat}$ is used, with no non-Gaussian correction. For TE $Z_B = C_B^{\rm dat}$ is also used since negative values of $C_B^{\rm dat}$ occur. The Fisher matrix of the bandpowers is transformed as

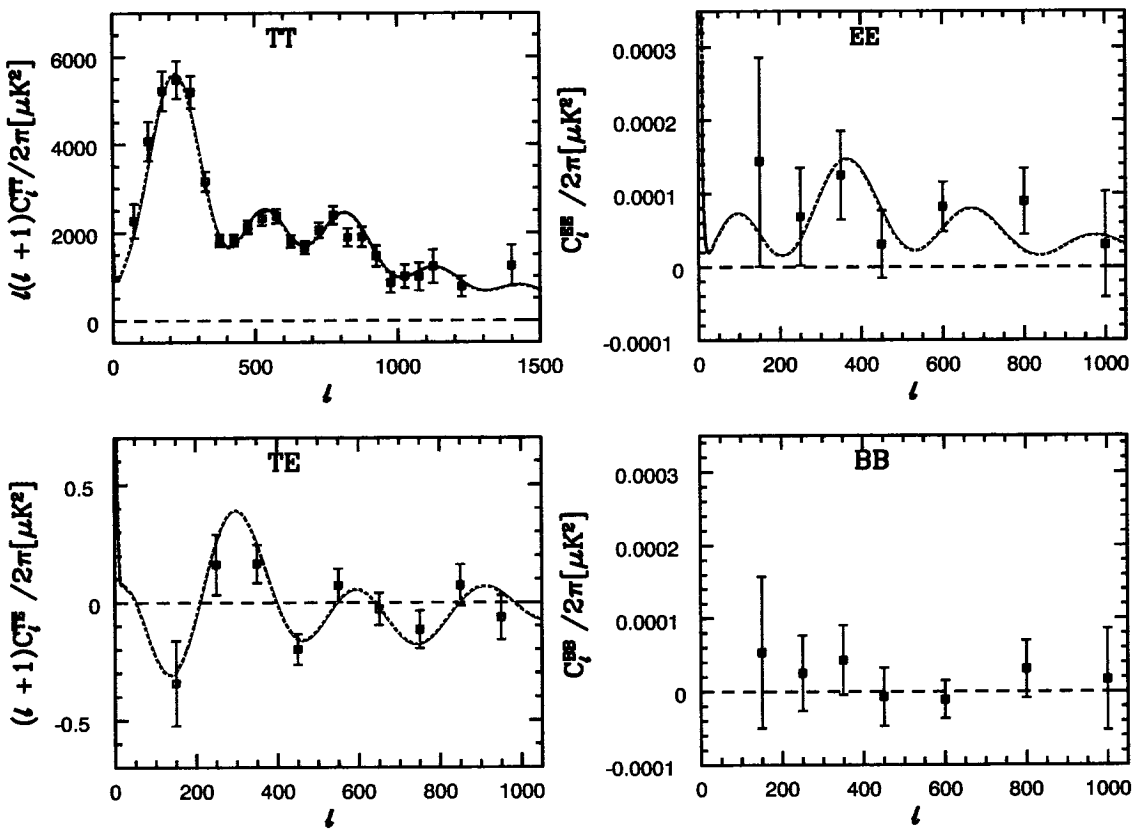

Figure 7.1: The B03 bandpowers used in this analysis. The total intensity TT, polarization EE and BB, and cross correlation TE spectra are included. The EB and TB spectra are excluded from this parameter analysis. The solid/black curve is the previous concordance model, a best fit to WMAP(first-year)+CBI+ACBAR data from `http://lambda.gsfc.nasa.gov/product/map/`, with $(\Omega_b h^2, \Omega_c h^2, n_s(k = 0.05), \exp(-2\tau), A(k = 0.05), h) = (0.0224, 0.111, 0.958, 0.802, 0.739, 0.720)$. The yellow/dotted curve is the CMBall (Table 7.3)+B03 maximum likelihood ΛCDM model from this analysis with (slightly different parameterization–see text), $(\Omega_b h^2, \Omega_c h^2, n_s(k = 0.05), \tau, \ln(10^{10} A_s(k = 0.05)), \theta) = (0.0228, 0.108, 0.959, 0.138, 3.12, 1.04)$.

$\widetilde{F}_{BB'} = Z'_B F_{BB'} Z'_{B'}$ with $Z'_B \equiv dZ_B/dC_B^{\rm dat} = (C_B^{\rm dat} + C_B^N)^{-1}$ if B is a TT bandpower and $Z'_B = 1$ otherwise.

In summary the XFASTER data products include the bandpowers, Fisher matrix, window functions and noise offsets.

7.1.2 Parameter Estimation Methodology

The Monte Carlo Markov Chain (MCMC) sampling technique used for this parameter estimation is described in detail in [62, 17, 51] and implemented in the publicly available COSMOMC[3] package. A brief summary of the relevant details is given here. The technique uses a Bayesian approach, generating samples of the posterior probability density function (PDF) of the parameters $\mathbf{y}$ given the data $\mathbf{z}$:

$$P(\boldsymbol{y}|\mathbf{z}) \propto P(\boldsymbol{y})P(\mathbf{z}|\boldsymbol{y}), \tag{7.2}$$

where $P(\mathbf{z}|\boldsymbol{y})$ is the likelihood PDF and $P(\boldsymbol{y})$ is the prior PDF of $\boldsymbol{y}$. The posterior is sampled by running a number of Markov Chains. The chains are constructed via the Metropolis-Hastings (MH) algorithm whereby a candidate parameter vector, $\boldsymbol{y'}$ is determined from an arbitrary *proposal density* distribution $q(\boldsymbol{y'}|\boldsymbol{y_n})$ where $\boldsymbol{y_n}$ is the current state of the chain. The candidate $\boldsymbol{y'}$ is accepted with *acceptance probability* given by

$$\alpha(\boldsymbol{y}|\boldsymbol{y_n}) = \min\left\{\frac{P(\boldsymbol{y'}|\mathbf{z})q(\boldsymbol{y_n}|\boldsymbol{y'})}{P(\boldsymbol{y_n}|\mathbf{z})q(\boldsymbol{y'}|\boldsymbol{y_n})}, 1\right\}. \tag{7.3}$$

At each point in the chain the acceptance probability for a candidate point is compared to a random number u drawn uniformly in the 0 to 1 range. If $u \leq \alpha(\boldsymbol{y'}|\boldsymbol{y_n})$ then the proposed vector is accepted and the next point in the chain is $\boldsymbol{y_{n+1}} = \boldsymbol{y'}$. If $u > \alpha(\boldsymbol{y'}|\boldsymbol{y_n})$

[3] `http://cosmologist.info/cosmomc`

then the proposed vector is rejected and $\boldsymbol{y_{n+1}} = \boldsymbol{y_n}$.

For the B03 CMB data the likelihood evaluation at each point in the chain requires the calculation of

$$\chi^2 = \sum_{BB'} (Z_B^{\rm mod}(\boldsymbol{y}) - Z_B^{\rm dat}) \widetilde{F}_{BB'} (Z_{B'}^{\rm mod}(\boldsymbol{y}) - Z_{B'}^{\rm dat}). \tag{7.4}$$

The WMAP data likelihood is computed using the likelihood code supplied by the WMAP team [87, 44], but with two modifications. The first modification is a change to the TE likelihood function to account for the correlation between the temperature and TE power spectrum estimators (the small correlations between the C_l estimators at different l are neglected) [23]. After the chains have been run importance sampling is used (e.g. see [51]) to correct the WMAP likelihood on large scales using the more computationally intensive likelihood code from [78]. This *Slosar-Seljak modification* uses a more accurate calculation of the WMAP likelihood at low multipoles ($\ell \leq 11$) and considers in more detail the errors associated with foreground removal.

The theoretical CMB spectra (as well as the matter power spectra) are computed using CAMB [52], a fast parallel Boltzmann code based on CMBFAST [74]. The statistics of interest, such as the marginalized posterior distribution of individual parameters, are calculated from the MCMC samples after removing burn in. Six chains are run for each combination of data and parameters that cannot be importance sampled. Numerical marginalization is performed over each data point's calibration and beam uncertainties at each sample in the chain. The calibration errors are assumed to be independent between data sets. Convergence is checked by ensuring that the standard deviation between chains of the 95%-percentile estimated from each chain is less than 0.2 in units of the all-chain parameter standard deviation. This should ensure that sampling errors on quoted limits are minimal.

Parameter estimates from MCMC have been shown to be in very good agreement

with those derived using an adaptive $\mathcal{C}_\ell$-grid [12] that was previously applied to the B98 analysis [73]. MCMC results for CMBall+B98 [11] are also in good agreement with those obtained for CMBall+B03 for the baseline model defined below with the same priors applied[4].

7.2 Data Combinations

7.2.1 The CMB Data

A number of combinations of data are considered. The B03 data set is broken into one subset consisting of the TT spectrum alone (B03TT), and another subset consisting of the EE, BB and TE spectra (B03pol) alone. Fits to the entire B03 data set, WMAP data alone and a combined B03 + WMAP data set are also considered. Next B03 is combined with available data from a collection of CMB experiments. Outlined in Table 7.3 are the experiments and multipole ranges which make up that collection, which is called CMBall. Note that because of the overlap in ℓ range (and sky coverage) of the ARCHEOPS [86] data with the WMAP data, the former cannot be included in the CMBall data set, unless a joint analysis is done. The B03 multipole range is given in Table 7.1. The cosmic variance of the WMAP and B03 data sets is correlated in the low multipole range (essentially over the first peak of the TT power spectrum). To account for this, the lower multipoles of the B03 TT spectrum ($\ell < 375$) are cut when combining B03 data with WMAP data.

7.2.2 The Large Scale Structure Data

For the final data combination the LSS observations from 2dFGRS and the SDSS are included. Some results of this analysis are sensitive to an overall galaxy bias factor, b_g,

[4]B03 and B98, with overlapping sky coverage, are correlated data sets. B98 is therefore excluded from this analysis and the combined B98 and B03 maps will be considered in a future analysis.

which is defined as the ratio of the square root of the galaxy-galaxy power spectrum for L_* galaxies to that of the mass density power spectrum today. Although the indications are that this is a number near unity [65, 84], here b_g is allow to take on arbitrary values by marginalizing it over a very broad distribution. Thus, the LSS information is only constraining models through the shape of the power spectrum, but not the overall amplitude. Constraining the overall amplitude is akin to imposing a prior on σ_8. To test sensitivity to this, varied Gaussian errors on b_g^2 about a mean are adopted. The mean is taken to be unity with errors on δb_g^2 appropriate for $\delta b_g = 0, 0.1, 0.5$ and 10, then marginalized over b_g^2. A uniform prior in b_g^2 leads to the same results as for $\delta b_g = 10$ [5]. Most parameter averages obtained are relatively insensitive to δb_g. The effect is commented on below: it has impact on the massive neutrino and dark energy equation of state constraints. SDSS data is used only for wavenumbers $k < 0.1h\mathrm{Mpc}^{-1}$ to avoid nonlinear corrections and to avoid possible non-uniform b_g complications. (See [84] for a discussion of these and other issues.)

An estimate using galaxy-galaxy lensing from SDSS [76] is $b_g = 0.99 \pm 0.07$. (These authors also used WMAP data to obtain this value, so it is not a completely independent determination of the bias.) An estimate using the 3-point function and redshift space clustering distortions for 2dFGRS gives $b_g = 1.04 \pm 0.04$ [88]. Based on these two analyses, adopting $b_g = 1.0 \pm 0.10$ to illustrate the effect of knowing the bias better, which translates into a σ_8 prior, seems reasonable.

7.2.3 Other Data Sets

The supernova data (SNIa) is applied in Section 7.3.2 to the determine the dark energy equation of state. For this the *gold* set, as described in [72] is used. Also, for a few cases the H_0 prior value from the HST Key Project [29] is included.

[5] Note that allowing b_g^2 to be negative has no effect and yields the same results as a (uniform) positive b_g^2 constraint.

7.3 Adiabatic Models

7.3.1 Baseline Model

Parameterization and Priors

For the baseline model a flat universe with photons, baryons, massless neutrinos, cold dark matter and a cosmological constant is considered. Initial conditions will be taken to be purely adiabatic (no isocurvature modes). A power law form for the power spectrum of the primordial comoving curvature perturbation, described by $\mathcal{P}_s = A_s(k/k_\star)^{(n_s-1)}$, where the n_s is the scalar spectral spectral index and A_s is the scalar amplitude (a pivot point $k_\star = 0.05\text{Mpc}^{-1}$ is chosen) is assumed. The physical baryon density and dark matter density are parameterized by $\Omega_b h^2$ and $\Omega_c h^2$, where $h = H_0/100\text{km s}^{-1}\text{Mpc}^{-1}$ is the Hubble parameter. The parameter θ is used to characterize the positions of the peaks in the angular power spectra, defined as one hundred times the ratio of the sound horizon to the angular diameter distance at last scattering [45]. Finally, the parameter τ is used to describe the Thomson scattering optical depth to decoupling. Thus the baseline model is a function of six cosmological parameters to which the following flat weak priors are imposed: $0.5 \leq n_s \leq 1.5$; $2.7 \leq \ln(10^{10}A_s) \leq 4.0$; $0.005 \leq \Omega_b h^2 \leq 0.1$; $0.01 \leq \Omega_c h^2 \leq 0.99$; $0.5 \leq \theta \leq 10.0$; and $0.01 \leq \tau \leq 0.8$. Additional weak priors restrict the age of the universe to 10Gyr $\leq$ age $\leq$ 20Gyr and the expansion rate to $0.45 \leq h \leq 0.9$. All priors are summarized in Table 7.2. Besides being generally agreed upon by cosmologists, the weak priors are consistent with those used in much of the CMB literature, *e.g.,* [50], [12] and [71]. Note that some of the results are sensitive to the choice of prior on H_0 and the effect of strengthening the H_0 prior is explored in Sections 7.3.2 and 7.3.2.

In addition to the base parameter values, the results also include marginalized constraints for several derived parameters including: Ω_Λ, the relative dark energy density; the age of the Universe; Ω_m, the relative total matter density; σ_8, the root mean square

Parameter	Limits	Parameter	Limits
$\Omega_b h^2$	0.005 - 0.1	n_s	0.5 - 1.5
$\Omega_c h^2$	0.01 - 0.99	$\ln[10^{10} A_s]$	2.7 - 4.0
θ	0.5 - 10.0	Age(Gyr)	10 - 20
τ	0.01 - 0.8	H_0	45 - 90

Table 7.2: List of weak priors imposed on baseline parameter set. Priors are uniform in the variable shown.

linear mass perturbation in $8h^{-1}$ Mpc spheres; z_{re}, the redshift of reionization assuming it is a sharp transition; and the Hubble constant, H_0.

Consistency of B03 Data Set

The resulting marginalized parameter constraints for the baseline model for each of the data combinations are given in Table 7.4 and presented graphically in Figure 7.2. In both Table 7.4 (and in the ones that follow) and Figure 7.2 the Bayesian 50% probability value (the median) obtained from the marginalized probability for each parameter is given. The quoted errors represent the 68% confidence interval obtained by integrating the marginalized distributions. In the case of upper or lower bounds, the 95% confidence limits are quoted. Note that the baseline CMBall+B03+LSS result is fairly insensitive to δb_g and that the less restrictive flat, uniform prior in b_g^2 has been chosen.

The comparison of B03pol and B03TT provides a robust internal consistency check. Note that the B03pol constraints to $\Omega_b h^2$ and $\Omega_c h^2$ are quite good with uncertainties which are only slightly larger than those of the B03TT result. However, the B03pol constraints on n_s, τ and A_s are weak and results for these cases are prior driven. Presented in Figure 7.3 is a 2D likelihood plot of θ versus the combined parameter $A_s e^{-2\tau}$. The latter determines the overall power in the *observed* CMB anisotropy (except at low ℓ), and is therefore better constrained than the primordial power A_s. CosmoMC uses a covariance matrix for the parameters and is therefore able to ascertain linear combination degeneracies. Although $\ln A_s$ and τ are used as base parameters, the proposal density knows that the combination $\ln(A_s e^{-2\tau})$ is well constrained and can explore the poorly

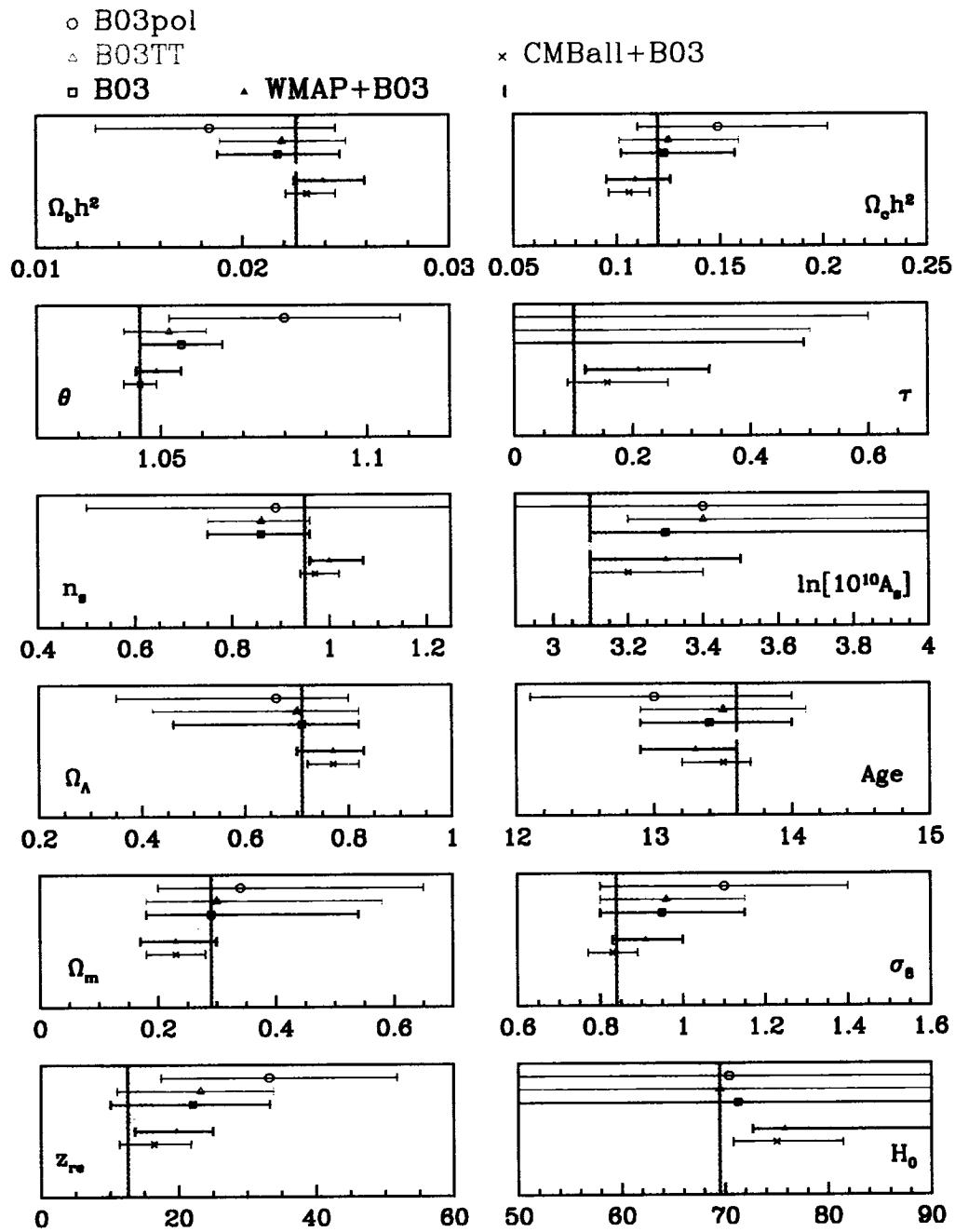

Figure 7.2: Median values obtained from the marginalized probability for each parameter for the baseline, standard model. The errors bars represent the 68% confidence interval. The 95% upper limit is given for the case of τ for B03 data alone. The flat weak priors imposed are as outlined in Table 7.2. The baseline CMBall+B03+LSS result is fairly insensitive to δb_g and that the less restrictive flat, uniform prior in b_g^2 has been chosen for this case.

constrained orthogonal direction efficiently. The B03 data alone does particularly well at constraining $A_s e^{-2\tau}$. The angular-diameter distance variable θ defines the shift with ℓ of the overall $\mathcal{C}_\ell$ pattern, in particular of the pattern of peaks and troughs. With all of the CMB data it is the best determined parameter in cosmology, 1.045 ± 0.004; with B03pol it is an important test which demonstrates the consistency of the positions of the polarization spectra peaks and troughs relative to those forecasted from the TT data, although the errors are larger with $\theta = 1.08 \pm 0.03$. For the CBI TT, TE and EE data in combination with WMAP TT and TE, [71] found $\theta = 1.044 \pm 0.005$. With just the CBI EE polarization data they determined $\theta = 1.06 \pm 0.04$, again showing the consistency of the data with the TT forecast of the polarization peaks and trough.

The B03 median parameter values are remarkably consistent with the parameter constraints from WMAP data alone. Note that in general the Slosar-Seljak modification to WMAP tends to broaden WMAP parameter likelihood curves and that the most significant impact on the median values is in τ ($\sim 0.3\sigma$ increase) and in Ω_m ($\sim 0.6\sigma$ decrease). Adding B03 to the WMAP data decreases the parameter uncertainties by an average of $\sim$15%. The most significant effect is a $\sim$30% decrease in the σ_8 uncertainty. Figure 7.4 shows the likelihood curves for the 6 base parameters and 6 derived parameters for a variety of data combinations. Overall the various data combinations are generally in good agreement at better than the 1σ level. The largest outlier is $\Omega_c h^2$ which increases by 1.5σ with the addition of the LSS data set. Also, similar to what is found in [79], the addition of small scale CMB data lowers both the value for the amplitude of fluctuations at $k = 0.05\text{Mpc}^{-1}$ and the value of the scalar spectral index. The effect of adding the LSS data follows this trend.

7.3.2 Modified Standard Model

In this section five extensions of the standard model are explored by adding, in turn, one parameter to the baseline parameter set. In all cases the same weak priors on the base

Experiment	Multipole Range	Reference
WMAP TT	$2 \leq \ell \leq 899$	[35]
WMAP TE	$2 \leq \ell \leq 450$	[44]
DASI TT	$380 \leq \ell \leq 800$	[32]
VSA TT	$400 \leq \ell \leq 1400$	[21]
ACBAR TT	$400 \leq \ell \leq 1950$	[48]
MAXIMA TT	$450 \leq \ell \leq 1150$	[34]
CBI TT	$750 \leq \ell \leq 1670$	[70]

Table 7.3: The CMBall data set.

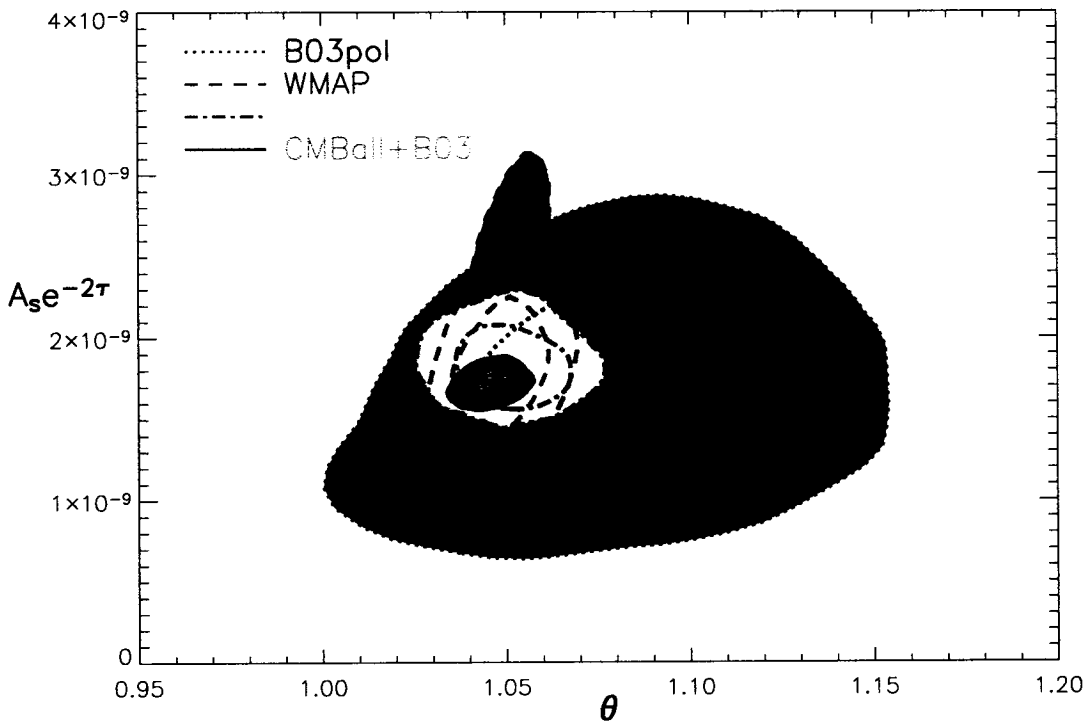

Figure 7.3: Constraints on $A_s e^{-2\tau}$ versus θ. Inner contours represent 68% likelihood regions and outer contours 95% likelihood regions. The peak position characterization parameter θ is best the determined parameter in cosmology, 1.045 ± 0.004, from the CMBall+B03 data set. The B03TT data does particularly well at constraining both the peak pattern and the combined $A_s e^{-2\tau}$ amplitude parameter. The constraint from WMAP alone on A_s is better than that from B03. The agreement between the B03pol and B03TT data is consistent with the basic inflation picture.

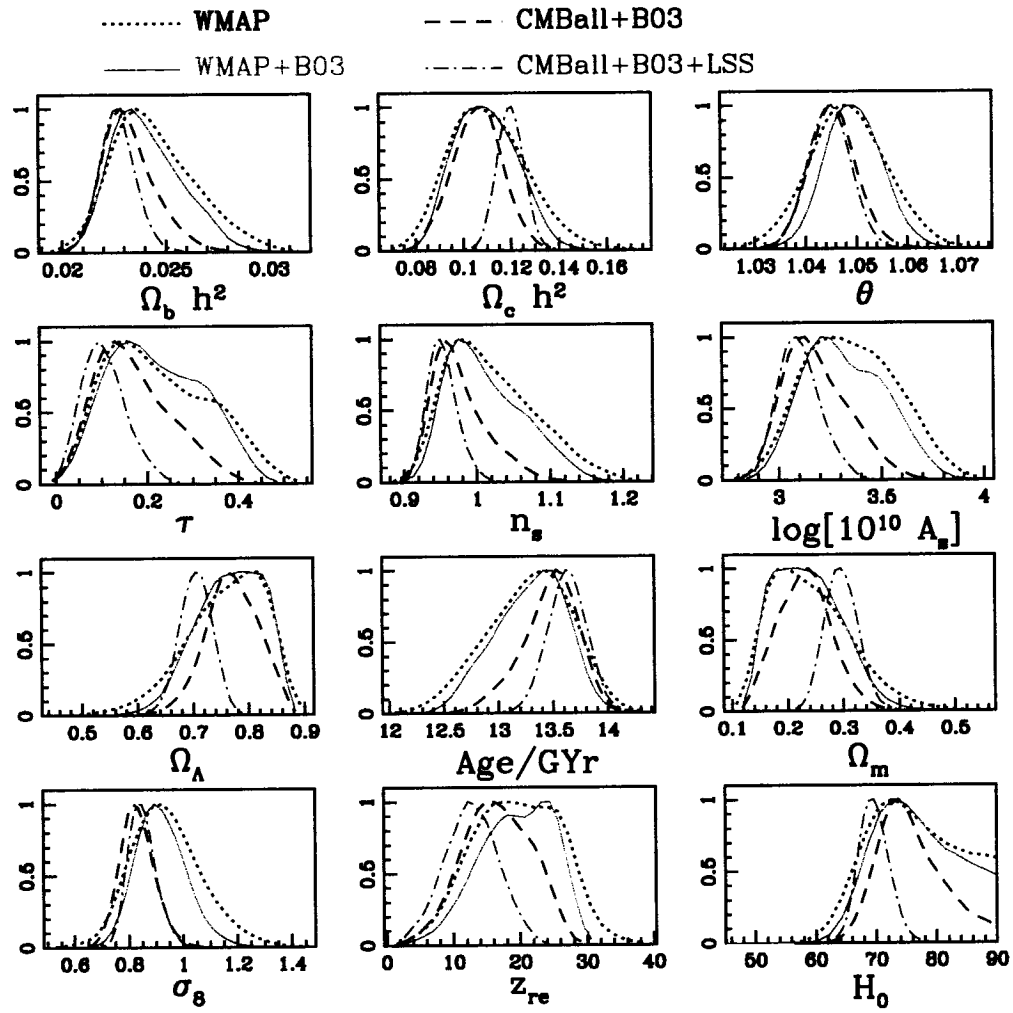

Figure 7.4: Marginalized one-dimensional distributions for the baseline model parameters for the data combinations WMAP only (black/dotted), WMAP + B03 (green/solid), CMBall + B03 (blue/dashed), and CMBall + B03 + LSS (red/dash-dotted). The curves are each normalized by their peak values. All distributions are derived from chains run with the weak set of external, uniform priors shown in Table 7.2. The LSS data consists of the 2dFGRS and SDSS redshift surveys (with a flat b_g^2 prior imposed). The most significant impact of the B03 data is on σ_8. Moreover, the σ_8 constraint from CMB data alone is quite strong, with the addition of LSS data having little effect.

	B03pol	B03TT	B03	WMAP	WMAP +B03	CMBall +B03	CMBall +B03+LSS
$\Omega_b h^2$	$0.0184^{+0.0061}_{-0.0055}$	$0.0219^{+0.0031}_{-0.0030}$	$0.0217^{+0.0030}_{-0.0029}$	$0.0242^{+0.0023}_{-0.0016}$	$0.0239^{+0.0020}_{-0.0014}$	$0.0231^{+0.0014}_{-0.0010}$	$0.0226^{+0.0009}_{-0.0008}$
$\Omega_c h^2$	$0.149^{+0.053}_{-0.039}$	$0.125^{+0.034}_{-0.024}$	$0.123^{+0.034}_{-0.021}$	$0.109^{+0.017}_{-0.014}$	$0.109^{+0.014}_{-0.012}$	$0.106^{+0.010}_{-0.010}$	$0.120^{+0.005}_{-0.005}$
θ	$1.080^{+0.028}_{-0.028}$	$1.052^{+0.009}_{-0.011}$	$1.055^{+0.010}_{-0.010}$	$1.048^{+0.008}_{-0.007}$	$1.049^{+0.006}_{-0.005}$	$1.045^{+0.004}_{-0.004}$	$1.045^{+0.004}_{-0.004}$
τ	< 0.66	< 0.50	< 0.49	$0.21^{+0.15}_{-0.10}$	$0.21^{+0.12}_{-0.09}$	$0.157^{+0.103}_{-0.068}$	$0.101^{+0.051}_{-0.044}$
n_s	$0.89^{+0.61}_{-0.39}$	$0.86^{+0.10}_{-0.11}$	$0.86^{+0.10}_{-0.11}$	$1.01^{+0.07}_{-0.05}$	$1.00^{+0.07}_{-0.04}$	$0.97^{+0.05}_{-0.03}$	$0.95^{+0.02}_{-0.02}$
$\ln[10^{10}A_s]$	$3.4^{+0.6}_{-0.7}$	$3.4^{+0.6}_{-0.2}$	$3.3^{+0.7}_{-0.2}$	$3.3^{+0.2}_{-0.2}$	$3.3^{+0.2}_{-0.2}$	$3.2^{+0.2}_{-0.1}$	$3.1^{+0.1}_{-0.1}$
Ω_Λ	$0.66^{+0.14}_{-0.31}$	$0.70^{+0.12}_{-0.28}$	$0.71^{+0.11}_{-0.25}$	$0.77^{+0.06}_{-0.08}$	$0.77^{+0.06}_{-0.07}$	$0.77^{+0.05}_{-0.05}$	$0.71^{+0.03}_{-0.03}$
Age(Gyr)	$13.0^{+1.0}_{-0.9}$	$13.5^{+0.6}_{-0.6}$	$13.4^{+0.6}_{-0.5}$	$13.3^{+0.3}_{-0.4}$	$13.3^{+0.3}_{-0.4}$	$13.5^{+0.2}_{-0.3}$	$13.6^{+0.2}_{-0.2}$
Ω_m	$0.34^{+0.31}_{-0.14}$	$0.30^{+0.28}_{-0.12}$	$0.29^{+0.25}_{-0.11}$	$0.23^{+0.08}_{-0.06}$	$0.23^{+0.07}_{-0.06}$	$0.23^{+0.05}_{-0.05}$	$0.29^{+0.03}_{-0.03}$
σ_8	$1.1^{+0.3}_{-0.3}$	$0.96^{+0.19}_{-0.16}$	$0.95^{+0.20}_{-0.15}$	$0.93^{+0.13}_{-0.11}$	$0.91^{+0.09}_{-0.08}$	$0.83^{+0.06}_{-0.06}$	$0.84^{+0.05}_{-0.05}$
z_{re}	$33.2^{+18.6}_{-15.7}$	$23.2^{+10.6}_{-12.2}$	$22.1^{+11.2}_{-12.0}$	$19.7^{+6.6}_{-6.7}$	$19.7^{+5.3}_{-6.0}$	$16.4^{+5.4}_{-5.0}$	$12.6^{+3.9}_{-4.0}$
H_0	$70.4^{+19.6}_{-25.4}$	$69.5^{+20.5}_{-24.5}$	$71.3^{+18.7}_{-26.3}$	$75.6^{+14.4}_{-3.5}$	$75.8^{+14.2}_{-3.1}$	$75.0^{+6.4}_{-4.2}$	$69.5^{+2.5}_{-2.3}$

Table 7.4: Marginalized parameter constraints for the baseline, 6 parameter, ΛCDM model. Parameter uncertainties represent the 68% confidence interval obtained by integrating the marginalized distributions. 95% confidence limits are quoted for the case of upper bounds. The following flat weak priors are imposed (as outlined in Table 7.2): $0.5 \leq n_s \leq 1.5$; $2.7 \leq \ln(10^{10}A_s) \leq 4.0$; $0.005 \leq \Omega_b h^2 \leq 0.1$; $0.01 \leq \Omega_c h^2 \leq 0.99$; $0.5 \leq \theta \leq 10.0$; and $0.01 \leq \tau \leq 0.8$. Additional weak priors restrict the age of the universe to 10Gyr ≤ age ≤ 20Gyr and the expansion rate to $45 \leq H_0 \leq 90$. The CMBall data set is as given in Table 7.3. The LSS data consists of the galaxy power spectra from the 2dFGRS and SDSS redshift surveys. The baseline CMBall+B03+LSS result is fairly insensitive to δb_g and for this case the less restrictive flat, uniform prior in b_g^2 has been chosen. The constraints from the B03pol data are in good agreement with the B03TT data, although some parameters constraints for the B03pol case are prior driven, *eg.* n_s, A_s and H_0. B03 does not constrain τ, but upper limits are given. The constraints from the various data set are consistent.

parameters as outlined in Table 7.2 are maintained. Some of the results are sensitive to the chosen prior range for H_0. For example, in certain cases the impact of strengthening the H_0 prior to the value from the HST Key Project [29], $h = 0.72 \pm 0.08$, with the errors treated as Gaussian is noted.

Running Index

The power law form for the power spectrum of the density perturbations is modified to allow the spectral index, n_s, to vary with scale. Following [46] this variation can be parameterized by the term $n_{\rm run} = dn_s/d\ln k$, such that $n_s = n_s(k_\star) + n_{\rm run}(k_\star)\ln(k/k_\star)$, where again $k_\star = 0.05{\rm Mpc}^{-1}$. The parameter $n_{\rm run}$ is restricted to lie between -0.3 and 0.3. Results from the combined data sets, CMBall+B03 and CMBall+B03+LSS, are given in Table 7.5.

The WMAP team report in [79] a detection of the running index of $n_{\rm run} = -0.031^{+0.016}_{-0.017}$ from their combined WMAPext+2dFGRS+Lyman α data set. [78] present a reduction in significance of the detection of $n_{\rm run}$ when their full likelihood analysis and detailed foreground removal is applied to the WMAP data. The Slosar-Seljak modification to WMAP decreases the significance of $n_{\rm run}$, but that inclusion of the data from the small scale CMB experiments has the opposite effect (as was the case found by [79]). From CMB data alone a median value for $n_{\rm run} = -0.071^{+0.035}$ is determined. This result is somewhat sensitive to the choice of prior. [79] apply a strong $\tau < 0.3$ prior which effectively reduces the median value of $n_{\rm run}$ for their CMB data only case. A Gaussian HST prior on H_0 is applied which lowers the significance of the running index to $n_{\rm run} = -0.065 \pm 0.035$ for the CMBall + B03 data set. Inclusion of the LSS data (with uniform prior in b_g^2) further reduces the significance and the median value from the larger combined data set is $n_{\rm run} = -0.050^{+0.026}_{-0.027}$. Note that the application of a Gaussian prior to b_g^2 has no impact on the running index parameter. Application of the HST prior on H_0 yields a final median value $n_{\rm run} = -0.048 \pm 0.026$ for the CMBall + B03 + LSS (+HST) data set. Figure 7.5

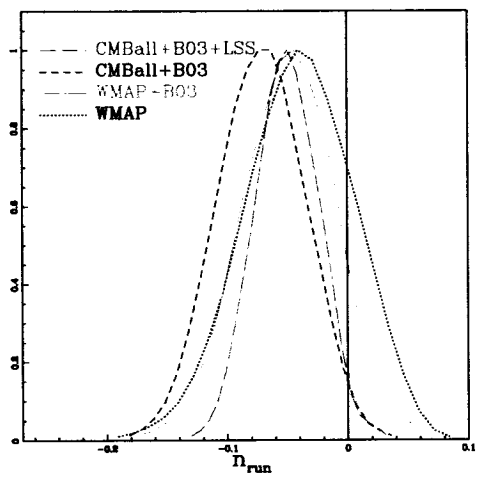

Figure 7.5: Marginalized one-dimensional distributions for the $n_{\rm run}$ parameter for the baseline + running index model. Weak priors imposed are those outlined in Table 7.2. The running index parameter is restricted to lie between -0.3 and 0.3. Application of the HST prior on H_0 slightly reduces the significance of a running index.

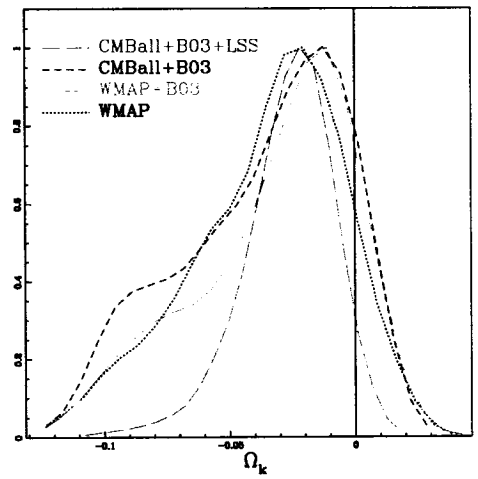

Figure 7.6: Marginalized one-dimensional distributions for Ω_k for the baseline model which allows non-zero curvature. Weak priors imposed are those outlined in Table 7.2. Ω_k is restricted to the range -0.3 and 0.3. The relatively wide scope for positive curvature is associated with the angular-diameter-distance degeneracy which is only partly broken by the CMB data. Application of the HST prior on H_0 to the larger combined data set somewhat reduces the possibility of significant curvature.

shows the likelihood curves for the $n_{\rm run}$ parameter for various data combinations. It is interesting to compare this result with that of [75], who argue that if the state-of-the-art modeling of Lyman α forest measurements is dominated by statistical rather than systematic errors, then $|n_{\rm run}| < 0.01$

Curvature

In this section a modification to the standard model which allows the possibility of non-flat geometry is considered. The curvature density is parameterized by Ω_k and is allowed to vary between -0.3 to 0.3. Table 7.5 shows the results for the CMBall+B03 and CMBall+B03+LSS data sets. The CMB data alone places a constraint on the curvature which is $\Omega_k = -0.030^{+0.026}_{-0.046}$. Shown in Figure 7.6 are the likelihood profiles for WMAP,

WMAP+B03, CMBall+B03 and CMBall+B03+LSS. While the addition of B03 data to the WMAP data tends to lower the significance of curvature, adding more small scale CMB data increases the width of the low end tail. Addition of the LSS data, with uniform prior in b_g^2, yields a median value of $\Omega_k = -0.024^{+0.014}_{-0.019}$. Application of the Gaussian prior in b_g^2 (with 10% uncertainty in b_g) has a slight effect with a resulting median value of $\Omega_k = -0.021^{+0.014}_{-0.016}$. If the H_0 value is restricted by the application of a Gaussian HST prior, the curvature density determined from the CMBall + B03 data set is $\Omega_k = -0.013^{+0.014}_{-0.018}$. Moreover, application of the more stringent H_0 prior reduces the median value of the curvature from the combined CMBall + B03 + LSS data set (flat b_g^2 prior) to $\Omega_k = -0.017^{+0.011}_{-0.014}$. The result agrees well with the constraint $\Omega_k = -0.010 \pm 0.009$ obtained by combining CMB data with the red luminous galaxy clustering data, which has its own signature of baryon acoustic oscillations [26].

Tensor Modes

So far in this chapter only scalar perturbations have been assumed. However inflationary models can produce tensor perturbations from gravitational waves that are predicted to evolve independently of the scalar perturbations, with an uncorrelated power spectrum $\mathcal{P}_\mathrm{t}$. The amplitude of a tensor mode falls off rapidly after horizon crossing and the effect is therefore predominantly on the largest scales: tensor modes entering the horizon along the line of site to last scattering distort the photon propagation and generate an additional anisotropy pattern. The tensor component is parameterized by the ratio $A_\mathrm{t}/A_\mathrm{s}$, where A_t is the primordial power in the transverse traceless part of the metric tensor on $0.05\mathrm{Mpc}^{-1}$ scales. A very weak prior on the amplitude ratio, restricting it to lie between 0 to 20, is imposed.

A tensor spectral index, defined by $\mathcal{P}_\mathrm{t} \propto k^{n_\mathrm{t}}$, must also be set. In inflation models it is related to the amplitude ratio by $A_\mathrm{t}/A_\mathrm{s} \approx -8n_\mathrm{t}/(1 - n_\mathrm{t}/2)$, so one parameter suffices. Rather than let n_t float as a second added parameter, it is chosen to make $\mathcal{P}_\mathrm{t}$ flat in k

(and thus set n_t to zero) for the computations of the tensor-induced component of $\mathcal{C}_\ell$.

Results are presented in Table 7.5, and Figure 7.7 illustrates the likelihood curves for the amplitude ratio for a number of data combinations. The influence of the high precision of the WMAP data on the largest scales is evident. Adding the small scale CMB data only slightly reduces the limit. An upper limit on the tensor ratio from CMB data (CMBall+B03 data set) alone of $A_t/A_s < 0.71$ (95% confidence limit) is determined. The CMB data appear to select models with relatively large tensor-to-scalar ratios. However, these models which have large values for the Hubble parameter ($H_0 \sim 85$) are allowed due to the poor constraint on H_0 when including tensor modes. In this case, the constraints on H_0 are driven mainly by the choice of weak priors and the data only provides a lower limit (see Table 7.5). With the application of the HST prior (which excludes these models with large H_0 values) the tensor limit from the CMBall+B03 data set is reduced to $A_t/A_s < 0.635$. A similar effect is obtained with the addition of the LSS data which further reduces the limit to $A_t/A_s < 0.36$. When b_g is constrained in the LSS data, the limits are very similar. The application of the more restrictive prior discussed above, with only $n_s \leq 1$ allowed to have a tensor contribution, lowers the CMBall+B03 limit to $A_t/A_s < 0.45$ and the CMBall+B03+LSS limit to $A_t/A_s < 0.31$.

Massive Neutrinos

Measurements from solar and atmospheric neutrino experiments, such as the Sudbury Neutrino Observatory [1] and Super-Kamiokande [85], indicate that neutrinos change flavour: different generations of neutrinos oscillate into each other. The implication of flavour changing is that neutrinos have mass. Given that neutrinos are the second most abundant particles in the Universe, massive neutrinos could have considerable impact on the energy density of the early Universe. This analysis considers the case of three neutrinos of degenerate mass, such that $\Omega_\nu h^2 = 3m_\nu/94.0\,\mathrm{eV}$. This assumption is well justified given the small square mass difference measured by oscillation experiments (at

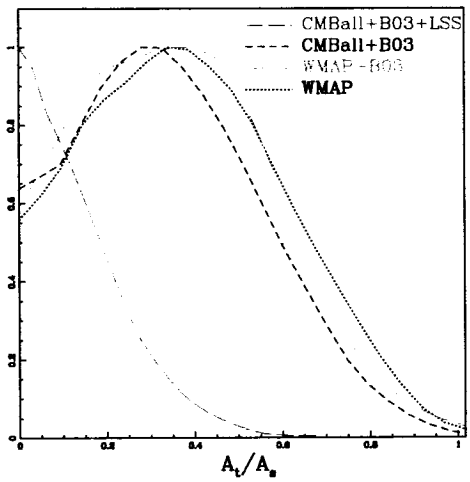

Figure 7.7: Marginalized one-dimensional distributions for the amplitude ratio A_t/A_s for the baseline model modification which allows tensor modes. Weak priors imposed are those outlined in Table 7.2. the weak prior $0 < A_t/A_s < 20$ is imposed to the tensor contribution. From CMB data alone (CMBall+B03) an upper limit (95% confidence) on the amplitude ratio of $A_t/A_s < 0.71$. For these models however, H_0 is only poorly constrained (see text). Addition of the LSS data reduces this limit to $A_t/A_s < 0.36$.

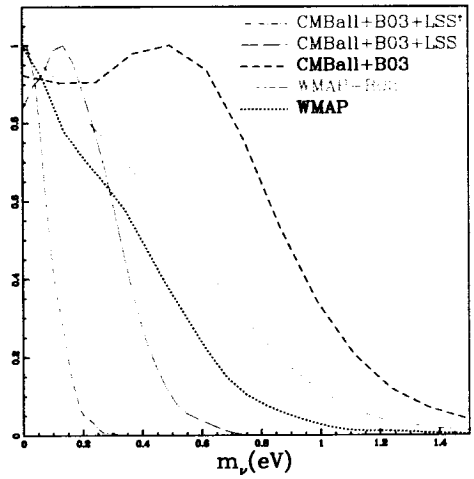

Figure 7.8: Marginalized one-dimensional distributions for m_ν for the baseline model which allows massive neutrinos (3 species of degenerate mass). Weak priors imposed are those outlined in Table 7.2. The massive neutrino contribution is parameterized as a fraction of the dark matter energy density, $f_\nu = \Omega_\nu h^2/\Omega_{DM} h^2$. From CMB data alone (CMBall+B03) an upper limit (95% confidence) on the neutrino mass of $m_\nu < 1.0\,\mathrm{eV}$. Adding the LSS data reduces this limit to $m_\nu < 0.40\,\mathrm{eV}$, without any b_g constraint, and to $m_\nu < 0.16\,\mathrm{eV}$, when $b_g = 1.0 \pm 0.10$ is used.

most $\delta m_\nu^2 \sim 10^{-3}\,\mathrm{eV}$, [2]). The massive neutrino contribution is parameterized as a fraction of the dark matter energy density, $f_\nu = \Omega_\nu h^2/\Omega_{DM} h^2 = 1 - \Omega_{CDM} h^2/\Omega_{DM} h^2$.

Results for the combined data sets are given in Table 7.5. From CMB data alone the upper limit on the neutrino fraction is $f_\nu < 0.21$ (95% confidence limit). This translates to an upper limit on the neutrino mass of $m_\nu < 1.0\,\mathrm{eV}$ or $\Omega_\nu h^2 < 0.033$. This limit is more stringent than the 3 eV upper limit on the electron neutrino mass determined from tritium beta decay experiments and recommended in the Review of Particle Physics [25]. Including the LSS data (flat b_g^2 prior) pushes this limit down considerably to $f_\nu < 0.093$ (95% confidence) and limits the neutrino mass to $m_\nu < 0.40\,\mathrm{eV}$. This result is somewhat larger than that found in [79]. The addition of more and more small scale CMB data drives the limit up as is evident in Figure 7.8. When $b_g = 1.0 \pm 0.10$ is used, the neutrino fraction upper limit is reduced to $f_\nu < 0.041$ (95% confidence), corresponding to a neutrino mass limit of $m_\nu < 0.16\,\mathrm{eV}$. This neutrino mass limit is in good agreement with the strong limit ($m_\nu < 0.18\,\mathrm{eV}$) obtained by [76], who included the bias constraint and the SDSS and WMAP data. In their analysis of b_g they found $\sigma_8 = 0.85^{+0.07}_{-0.06}$, with $b_g = 1.02^{+0.08}_{-0.08}$. This compares with the values we obtain: $\sigma_8 = 0.85 \pm 0.04$ with $\delta b_g = 0.10$ and $\sigma_8 = 0.73^{+0.08}_{-0.07}$ with $\delta b_g = \infty$.

Dark Energy

The standard model predicts (and CMB observations strongly support) a universe which is nearly flat, implying a total energy density approaching critical. The total matter density however, comprises only one third of the total energy density. The prevailing energy density component comes from some form of dark energy which up to now has been assumed to take the form of a vacuum density or cosmological constant, Λ, with equation of state described by $w = p/\rho = -1$, where p and ρ are the dark energy pressure and density respectively. In this section the possibility that the dark energy component is a rolling scalar field or quintessence (see for example [69] or [40]) is considered, allowing

the effective constant equation of state parameter w to differ from -1. The parameter w is treated as a redshift-independent phenomenological factor and it is allowed to vary with a uniform prior over the range -4 to 0. The cases with w restricted to lie in the range -1 to 0 was also considered and similar limits were found. To be self-consistent, perturbations in the dark energy should be allowed for when w is not -1, although these have a small impact and only at low multipoles. The effective sound speed for the perturbations is set to unity in CAMB, the value for a scalar field.

The marginalized one-dimensional distributions for various data combinations are presented in Figure 7.9. From CMB data alone $w = -0.86^{+0.35}_{-0.36}$. The addition of the LSS data, applying the conservative uniform flat prior on b_g^2 to the galaxy bias factor, yields a median value of $w = -0.64^{+0.15}_{-0.18}$. This result is highly sensitive to the choice of prior on b_g^2. The uniform flat prior on b_g^2 gives a relatively high best fit bias value of $b_g = 1.3$. Applying a more restrictive Gaussian prior to b_g^2 gives: $w = -0.94^{+0.13}_{-0.16}$ with $b_g = 1.0 \pm 0.10$; and $w = -0.74^{+0.13}_{-0.17}$ with $b_g = 1.0 \pm 0.50$. The effect of adding the SNIa data is explored which significantly improves the constraint on w yielding $w = -0.94^{+0.093}_{-0.097}$ with the flat prior on b_g^2. Results for the CMBall+B03 data set and the CMBall+B03+LSS+SNIa data set are given in Table 7.5.

Figure 7.10 illustrates the degeneracy in the $\Omega_m - w$ plane that cannot be broken by CMB data alone and is only weakly broken with the addition of the LSS data (flat prior on b_g^2). Application of a more restrictive Gaussian prior to b_g^2 for the LSS data or addition of the SNIa data breaks the degeneracy.

7.4 Sub-dominant Isocurvature Model

So far, it has been assumed that in the early radiation dominated era the matter and radiation densities are all identically perturbed, giving an overall total density and hence curvature perturbation. This is not, however, the only possibility. Isocurvature modes

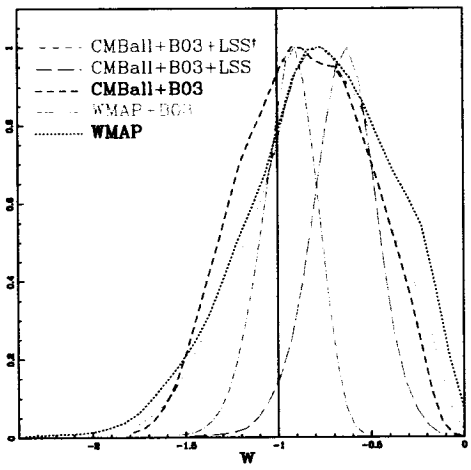

Figure 7.9: Marginalized one-dimensional distributions for the dark matter equation of state parameter w. Weak priors imposed on the base parameters are those outlined in Table 7.2. The prior $-4 < w < 0$ is imposed. The † denotes the application of a Gaussian prior to b_g^2 (with $b_g = 1 \pm 10\%$). The nominal flat uniform prior on b_g^2 yields a slightly higher median value for w, driven by higher values of b_g. Adding the SNIa data however, reduced the median value to $-0.94^{+0.093}_{-0.097}$.

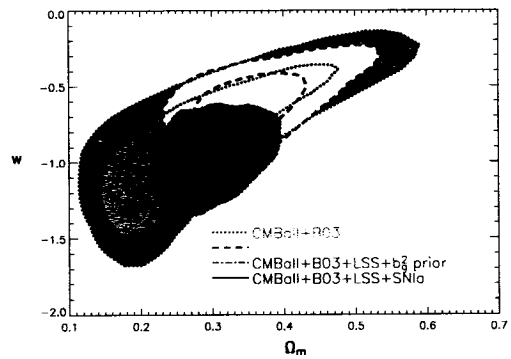

Figure 7.10: Constraints on w versus Ω_m for a flat ΛCDM model that allows the dark energy equation of state parameter, w, to differ from -1. Inner contours represent 68% likelihood regions and outer contours 95% likelihood regions. A more stringent Gaussian b_g^2 prior (with $b_g = 1 \pm 10\%$) or the addition of SNIa data is required to break the strong geometric degeneracy.

	Base+Running Index		*Base+Curvature*	
	CMBall +B03	CMBall +LSS+B03	CMBall +B03	CMBall +LSS+B03
$\Omega_b h^2$	$0.0237^{+0.0020}_{-0.0019}$	$0.0218^{+0.0010}_{-0.0009}$	$0.0227^{+0.0014}_{-0.0009}$	$0.0226^{+0.0010}_{-0.0009}$
$\Omega_c h^2$	$0.102^{+0.017}_{-0.011}$	$0.125^{+0.007}_{-0.007}$	$0.108^{+0.009}_{-0.013}$	$0.111^{+0.008}_{-0.008}$
θ	$1.048^{+0.005}_{-0.005}$	$1.044^{+0.004}_{-0.004}$	$1.044^{+0.005}_{-0.004}$	$1.044^{+0.004}_{-0.004}$
τ	$0.33^{+0.11}_{-0.16}$	$0.145^{+0.031}_{-0.030}$	$0.149^{+0.115}_{-0.064}$	$0.128^{+0.032}_{-0.118}$
n_s	$0.96^{+0.05}_{-0.06}$	$0.90^{+0.04}_{-0.04}$	$0.96^{+0.05}_{-0.02}$	$0.95^{+0.03}_{-0.02}$
$\ln[10^{10}A_s]$	$3.5^{+0.2}_{-0.3}$	$3.2^{+0.1}_{-0.1}$	$3.2^{+0.2}_{-0.1}$	$3.1^{+0.1}_{-0.1}$
Ω_Λ	$0.80^{+0.05}_{-0.09}$	$0.67^{+0.04}_{-0.04}$	$0.68^{+0.11}_{-0.15}$	$0.67^{+0.04}_{-0.05}$
Age(Gyr)	$13.3^{+0.4}_{-0.4}$	$13.7^{+0.2}_{-0.2}$	$14.9^{+1.3}_{-1.3}$	$14.7^{+0.7}_{-0.6}$
Ω_m	$0.20^{+0.09}_{-0.05}$	$0.33^{+0.04}_{-0.04}$	$0.35^{+0.19}_{-0.13}$	$0.35^{+0.06}_{-0.05}$
σ_8	$0.91^{+0.07}_{-0.07}$	$0.88^{+0.07}_{-0.05}$	$0.81^{+0.06}_{-0.05}$	$0.81^{+0.06}_{-0.05}$
z_{re}	$26.2^{+4.1}_{-8.0}$	$16.8^{+5.0}_{-5.0}$	$16.0^{+6.3}_{-4.9}$	$14.5^{+4.9}_{-4.5}$
H_0	$78.7^{+11.3}_{-9.3}$	$66.7^{+1.5}_{-1.4}$	$61.3^{+14.3}_{-16.3}$	$61.8^{+2.3}_{-2.3}$
$n_{\rm run}$	$-0.071^{+0.035}_{-0.037}$	$-0.050^{+0.026}_{-0.027}$	-	-
Ω_k	-	-	$-0.030^{+0.026}_{-0.046}$	$-0.024^{+0.014}_{-0.019}$

	Base+Tensor Modes		*Base+Massive Neutrinos*	
	CMBall +B03	CMBall +LSS+B03	CMBall +B03	CMBall +LSS+B03
$\Omega_b h^2$	$0.0246^{+0.0013}_{-0.0013}$	$0.0232^{+0.0010}_{-0.0009}$	$0.0224^{+0.0016}_{-0.0011}$	$0.0224^{+0.0009}_{-0.0008}$
$\Omega_c h^2$	$0.0945^{+0.0102}_{-0.0074}$	$0.117^{+0.006}_{-0.006}$	$0.121^{+0.013}_{-0.015}$	$0.125^{+0.008}_{-0.007}$
θ	$1.048^{+0.004}_{-0.005}$	$1.046^{+0.004}_{-0.004}$	$1.046^{+0.005}_{-0.005}$	$1.045^{+0.004}_{-0.004}$
τ	$0.158^{+0.076}_{-0.066}$	$0.0991^{+0.0542}_{-0.0438}$	$0.145^{+0.114}_{-0.069}$	$0.103^{+0.054}_{-0.042}$
n_s	$1.02^{+0.03}_{-0.04}$	$0.97^{+0.03}_{-0.02}$	$0.94^{+0.05}_{-0.03}$	$0.94^{+0.02}_{-0.02}$
$\ln[10^{10}A_s]$	$3.1^{+0.1}_{-0.1}$	$3.1^{+0.1}_{-0.1}$	$3.1^{+0.2}_{-0.1}$	$3.1^{+0.1}_{-0.1}$
Ω_Λ	$0.83^{+0.03}_{-0.04}$	$0.72^{+0.03}_{-0.03}$	$0.64^{+0.12}_{-0.11}$	$0.65^{+0.05}_{-0.06}$
Age(Gyr)	$13.2^{+0.3}_{-0.2}$	$13.5^{+0.2}_{-0.2}$	$14.2^{+0.3}_{-0.5}$	$13.9^{+0.2}_{-0.2}$
Ω_m	$0.173^{+0.044}_{-0.026}$	$0.28^{+0.03}_{-0.03}$	$0.36^{+0.11}_{-0.12}$	$0.35^{+0.06}_{-0.05}$
σ_8	$0.77^{+0.07}_{-0.07}$	$0.84^{+0.05}_{-0.05}$	$0.58^{+0.15}_{-0.11}$	$0.73^{+0.08}_{-0.07}$
z_{re}	$15.4^{+4.3}_{-4.6}$	$12.2^{+4.0}_{-4.0}$	$16.3^{+6.4}_{-5.6}$	$13.0^{+4.1}_{-3.9}$
H_0	> 73.2	$71.2^{+3.1}_{-2.7}$	$63.1^{+9.9}_{-5.6}$	$64.9^{+3.8}_{-3.9}$
A_t/A_s	< 0.71	< 0.36	-	-
f_ν	-	-	< 0.21	< 0.09

	Base+w		*Baseline*	
	CMBall +B03	CMBall +LSS+B03+SNIa	CMBall +B03	CMBall +LSS+B03
$\Omega_b h^2$	$0.0232^{+0.0015}_{-0.0011}$	$0.0228^{+0.0009}_{-0.0009}$	$0.0231^{+0.0014}_{-0.0010}$	$0.0226^{+0.0009}_{-0.0008}$
$\Omega_c h^2$	$0.106^{+0.010}_{-0.011}$	$0.117^{+0.007}_{-0.008}$	$0.106^{+0.010}_{-0.010}$	$0.120^{+0.005}_{-0.005}$
θ	$1.046^{+0.005}_{-0.004}$	$1.045^{+0.004}_{-0.004}$	$1.045^{+0.004}_{-0.004}$	$1.045^{+0.004}_{-0.004}$
τ	$0.150^{+0.089}_{-0.066}$	$0.110^{+0.061}_{-0.047}$	$0.157^{+0.103}_{-0.068}$	$0.101^{+0.051}_{-0.044}$
n_s	$0.97^{+0.05}_{-0.03}$	$0.96^{+0.03}_{-0.02}$	$0.97^{+0.05}_{-0.03}$	$0.95^{+0.02}_{-0.02}$
$\ln[10^{10}A_s]$	$3.1^{+0.2}_{-0.1}$	$3.1^{+0.1}_{-0.1}$	$3.2^{+0.2}_{-0.1}$	$3.1^{+0.1}_{-0.1}$
Ω_Λ	$0.74^{+0.08}_{-0.13}$	$0.70^{+0.02}_{-0.02}$	$0.77^{+0.05}_{-0.05}$	$0.71^{+0.03}_{-0.03}$
Age(Gyr)	$13.6^{+0.4}_{-0.3}$	$13.6^{+0.2}_{-0.2}$	$13.5^{+0.2}_{-0.3}$	$13.6^{+0.2}_{-0.2}$
Ω_m	$0.26^{+0.13}_{-0.08}$	$0.30^{+0.02}_{-0.02}$	$0.23^{+0.05}_{-0.05}$	$0.29^{+0.03}_{-0.03}$
σ_8	$0.77^{+0.14}_{-0.15}$	$0.82^{+0.06}_{-0.06}$	$0.83^{+0.06}_{-0.06}$	$0.84^{+0.05}_{-0.05}$
z_{re}	$16.0^{+5.0}_{-5.0}$	$13.3^{+4.3}_{-4.2}$	$16.4^{+5.4}_{-5.0}$	$12.6^{+3.9}_{-4.0}$
H_0	$69.9^{+13.2}_{-12.8}$	$68.5^{+2.1}_{-2.0}$	$75.0^{+6.4}_{-4.2}$	$69.5^{+2.5}_{-2.3}$
w	$-0.86^{+0.35}_{-0.36}$	$-0.94^{+0.093}_{-0.097}$	-	-

Table 7.5: Marginalized parameter constraints for five modifications of the baseline model. Parameter uncertainties represent the 68% confidence interval. For the case of upper or lower bounds 95% confidence limits are quoted. The flat weak priors imposed on the base 6 parameters are as outlined in Table 7.2. One parameter is added in turn to the base set and the following priors are imposed on each: running index, $-0.3 < n_{\rm run} < 0.3$; curvature, $-0.3 < \Omega_k < 0.3$; amplitude ratio, $0 < A_t/A_s < 20$; neutrino fraction of dark matter, $0 < f_\nu < 1$; and dark energy equation of state, $-4 < w < 0$. The CMBall data set is as given in Table 7.3. The LSS data consists of the matter power spectra from the 2dFGRS and SDSS redshift surveys. The galaxy bias factor b_g is marginalized assuming a uniform flat prior in b_g^2. For the $Base + w$ case only both the LSS and SNIa data are added.

describe the other linear combinations of matter and radiation perturbations that do not initially contribute a curvature perturbation. Almost any measured TT power spectrum can be fit well by using combinations of initial perturbations, for example by adding structure to the primordial power spectrum, and/or by adding isocurvature modes. Determination of the basic cosmic parameters suffers with addition of these highly correlated extra degrees of freedom. Degeneracies may be broken by the addition of polarization data. In particular the temperature and polarization power spectra for isocurvature modes have the peaks out of phase with those from adiabatic modes (see *e.g.*, [7], [38]). A mix of isocurvature and adiabatic modes can give acceptable fits to the CMB temperature power spectra (*e.g.*, [15, 49]), and the polarization data may be added to distinguish among these more complex models.

To illustrate the constraints that can be determined from the current CMB data, a simple hybrid case is considered here consisting of the basic adiabatic mode model with constant spectral index, a single cold dark matter (CDM) isocurvature mode with its own constant primordial spectral index $n_{\rm iso}$, with no correlation between the two. This adds another two parameters to the basic six, $n_{\rm iso}$ and an amplitude ratio $R_2 \equiv (A_{iso}/A_{\rm s})$. The isocurvature perturbations are assumed to be Gaussian-distributed as was done for the adiabatic modes.

Rather than using $n_{\rm iso}$ as a basic parameter, two amplitude ratios are used for the two parameters that characterize the CDM isocurvature mode, following a suggestion of [49]:

$$R_2 \equiv \mathcal{P}_{\rm iso}(k_2)/\mathcal{P}_{\rm s}(k_2)\,,\ k_2 = 0.05{\rm Mpc}^{-1}, \qquad (7.5)$$
$$R_1 \equiv \mathcal{P}_{\rm iso}(k_1)/\mathcal{P}_{\rm s}(k_1),\ k_1 = 0.005{\rm Mpc}^{-1}\,.$$

Here $\mathcal{P}_{\rm s}(k)$ is the power in the primordial curvature perturbation and $\mathcal{P}_{\rm iso}(k)$ is the power in the primordial CDM-photon entropy perturbation. The k_2 scale corresponds to $\ell \sim 700$

and k_1 to $\ell \sim 70$. A uniform prior probability is adopted over the range 0 to 20 for R_1, and over 0 to 100 for R_2. The isocurvature spectral index $n_{\rm iso}$, defined by $\mathcal{P}_{\rm iso}(k) \propto k^{n_{\rm iso}}$, is now a derived parameter, expressible in terms of R_1, R_2 and the adiabatic spectral index $n_{\rm s}$, defined by $\mathcal{P}_{\rm s}(k) \propto k^{n_{\rm s}-1}$,

$$n_{\rm iso} = n_{\rm s} - 1 + \ln(R_2/R_1)/\ln(k_2/k_1)\,. \tag{7.6}$$

Two cases are explored. In the first both amplitude ratios are allowed to vary. In the second case, the isocurvature spectral index is fixed to $n_{\rm iso} = 3$. This is the deemed the "isocurvature seed" white noise spectrum with no spatial correlation.

Results are shown in Table 7.6 for the CMBall+B03+HST data combination. Aside from the more stringent HST data prior on H_0, all priors on the 6 base parameters are as outlined in Table 7.2. Although results indicate that there is no evidence for the presence of an isocurvature mode, the upper limits still allow for a sub-dominant component. The limits shown in Table 7.6 demonstrate that the large scale R_1, dominated by the WMAP data, is much better constrained at < 0.3 than the small scale $R_2 < 2.3$, which B03 probes. This translates into a preference for steeper $n_{\rm iso}$ than the scale invariant value. Since for neither is there an indication of a non-zero value, just upper limits, the results are sensitive to the prior probabilities assign to them. The choice of uniform prior for R_1 and R_2 is conservative in that the upper limits decrease with other choices, *e.g.*, one uniform in $\ln(R_i)$ (a non-informative prior), or one uniform in $n_{\rm iso}$ and R_2. The conservative choice actually downgrades the probability of steep $n_{\rm iso}$. (The B03pol data by itself only limits $R_1 < 17$ and $R_2 < 22$; the full B03 data gives $R_1 < 1.8$ and $R_2 < 5.3$.)

The strongest constraints come from the low ℓ part of the spectrum. However, spectra that are significantly steeper than inflation-motivated nearly-scale-invariant ones are still allowed by the data. To focus attention on the role played by the new, high ℓ B03 results, $n_{\rm iso}$ is now fixed at 3, the white noise 'seed' spectrum, the limiting case in which the

isocurvature perturbations when created were uncorrelated spatially. The large angular scales are highly suppressed and the isocurvature peaks and troughs emerge looking somewhat like an ℓ-shifted version of the adiabatic spectrum. The two spectra then test at what level interleaved isocurvature peaks are allowed by the CMB data. Results are shown in Table 7.6. To relate the $R_2 < 3.0$ limit to a more intuitive expression of what the CMBall+B03+HST data set data allows, note that over a bandpower in ℓ from 75 to 1400, $\mathcal{C}_B^{TT(\mathrm{iso})}/\mathcal{C}_B^{TT(\mathrm{s})} \sim (0.005)R_2$, hence the upper limit corresponds to an allowed CMB contamination of this sub-dominant component of TT of only a few percent. Over a bandpower in ℓ from 150 to 1000 the ratio $\mathcal{C}_B^{EE(\mathrm{iso})}/\mathcal{C}_B^{EE(\mathrm{s})} \sim (0.008)R_2$, for the allowed EE isocurvature bandpower contamination. B03pol gives $R_2 < 58$. The full B03 data set including TT gives $R_2 < 9.5$[6].

The $n_{\mathrm{iso}} = 3, 2$ illustration allows one to conclude that even with the errors on the EE and TE data, there is evidence against the isocurvature shifted pattern over the adiabatic pattern and only restricted room for an interleaved peak pattern, at a level below 50%. This test differs from the adiabatic-only peak/trough pattern shift using B03pol Fig.7.3 since there are no interleaved peaks and troughs in that case. Examination of the CAMB models obtained from the marginalized constraints in Table 7.6 reveals that the parameters chosen by COSMOMC adjust to make the adiabatic $\mathcal{C}_\ell^{\mathrm{s}}$ pattern compensate for the isocurvature $\mathcal{C}_\ell^{\mathrm{iso}}$ contamination.

[6]The $n_{\mathrm{iso}} = 2$ case mimics even more the peak/trough patterns in $\mathcal{C}_\ell$ except for the shift, so that case was tested as well. CMBall+B03+HST gives $R_2 < 2.7$, B03 alone, but with TT, gives $R_2 < 6.8$ and B03pol gives $R_2 < 41$. Translation to the allowed contamination is done with the bandpower ratios $\mathcal{C}_B^{TT(\mathrm{iso})}/\mathcal{C}_B^{TT(\mathrm{s})} \sim (0.007)R_2$, $\mathcal{C}_B^{EE(\mathrm{iso})}/\mathcal{C}_B^{EE(\mathrm{s})} \sim (0.009)R_2$.

	Baseline	Adiabatic + Iso	Adiabatic + White Iso
	CMBall +B03+HST	CMBall +B03+HST	CMBall +B03+HST
$\Omega_b h^2$	$0.0229^{+0.0011}_{-0.0009}$	$0.0246^{+0.0016}_{-0.0013}$	$0.0234^{+0.0013}_{-0.0010}$
$\Omega_c h^2$	$0.108^{+0.008}_{-0.009}$	$0.103^{+0.009}_{-0.009}$	$0.107^{+0.008}_{-0.009}$
θ	$1.045^{+0.004}_{-0.004}$	$1.051^{+0.006}_{-0.005}$	$1.046^{+0.005}_{-0.004}$
τ	$0.142^{+0.077}_{-0.058}$	$0.156^{+0.078}_{-0.062}$	$0.149^{+0.079}_{-0.063}$
n_s	$0.96^{+0.03}_{-0.02}$	$1.00^{+0.05}_{-0.04}$	$0.96^{+0.03}_{-0.02}$
R_1	–	< 0.28	–
R_2	–	< 2.3	< 3.0
$n_{\rm iso}$	–	$0.99^{+0.63}_{-0.46}$	$3.0(fixed)$
$\ln[10^{10} A_s]$	$3.1^{+0.2}_{-0.1}$	$3.1^{+0.1}_{-0.1}$	$3.1^{+0.2}_{-0.1}$
Ω_Λ	$0.76^{+0.04}_{-0.04}$	$0.80^{+0.04}_{-0.04}$	$0.77^{+0.04}_{-0.04}$
Age(Gyr)	$13.5^{+0.2}_{-0.2}$	$13.2^{+0.3}_{-0.3}$	$13.4^{+0.2}_{-0.2}$
Ω_m	$0.24^{+0.04}_{-0.04}$	$0.20^{+0.04}_{-0.04}$	$0.23^{+0.04}_{-0.04}$
z_{re}	$15.4^{+4.7}_{-4.5}$	$15.5^{+4.4}_{-4.4}$	$15.7^{+4.7}_{-4.8}$
H_0	$73.9^{+4.5}_{-3.5}$	$79.8^{+6.1}_{-5.0}$	$75.5^{+4.8}_{-3.8}$

Table 7.6: Marginalized parameter constraints for a model which includes both (dominant) adiabatic and (sub-dominant) isocurvature modes. Parameter uncertainties represent the 68% confidence interval. Upper bounds are 95% confidence limits. The flat weak priors are imposed on the base 6 parameters are as outlined in Table 7.2. The CMBall data set is defined in Table 7.3. The baseline model result is included (with the more stringent HST prior) for comparison. Two parameterizations for the isocurvature model are considered. For the first (column two) two parameters are added to the basic six: $R_2 \equiv \mathcal{P}_{\rm iso}(k_2)/\mathcal{P}_{\rm s}(k_2)$, with pivot scale $k_2 = 0.05{\rm Mpc}^{-1}$; and $R_1 \equiv \mathcal{P}_{\rm iso}(k_1)/\mathcal{P}_{\rm s}(k_1)$ with $k_1 = 0.005{\rm Mpc}^{-1}$. The priors $0 < R_1 < 20$ and $0 < R_2 < 100$ are imposed. For this case the isocurvature spectral index, $n_{\rm iso}$, is a derived parameter. Also considered is the "white isocurvature" case (column three) where $n_{\rm iso} = 3$ is fixed and the amplitude ratio $R_2 \equiv (A_{\rm iso}/A_{\rm s})$ is allowed to lie anywhere between 0 and 100.

Chapter 8

Conclusions

The B03 temperature angular power spectrum is the most precise *intermediate* scale measurement of CMB temperature anisotropy to date. The polarization power spectrum represents a $\sim 5\sigma$ detection in the $\ell = 100$ to $\ell = 1000$ multipole range. The success of the new PSB technology used in B03 to measure the CMB polarization signal is a crucial step toward ensuring the success of the High Frequency Instrument on the Planck satellite.

While the polarization data is not yet at the level of accuracy of the intensity data, cross checks of best fit parameters from the B03pol data and B03TT data indicate consistent results. The consistency of the shape parameter θ determined from B03pol and from B03TT demonstrates that the peak and trough positions forecast by the spectra are in robust agreement. The B03 data set does well at constraining the cosmological parameters of the standard ΛCDM model. The results are in good agreement with those derived from other CMB experiments, as is evident in Table 7.4. The parameter constraints derived from the B03 data set in combination with the WMAP data are highly competitive with those from the CMBall data set.

In Chapter 2 the following questions were posed: does the current data prefer the spectral index, n_s to vary with scale?; to what degree is a non-flat geometry is allowed?;

what are the upper limits on tensor modes?; is a massive neutrino dark matter component allowed?; and finally does the data allow the dark energy to take on some form other than a cosmological constant? These questions are addressed in Chapter 7. The resulting constraints from the CMBall+LSS data set, representing the most up-to-date parameter analysis, are: slight evidence (both $< 2\sigma$) for a running index and curvature; an upper (95% confidence) limit on the tensor-to-scalar ratio of $A_t/A_s < 0.36$; an upper (95% confidence) limit on the neutrino mass of $m_\nu < 0.40\,\mathrm{eV}$ $m_\nu < 0.4eV$ ($m_\nu < 1.0eV$ from CMB data alone); and, after adding the supernova (SNIa) data, a constraint on the dark energy equation of state of $w = -0.94^{+0.093}_{-0.097}$ (68% confidence interval). In all cases, the data prefers values for each of the non-standard parameters which are very close to the fixed values for the baseline model case. In other words the answer to–what happens when a new parameter is added?–is, not much. While the alternate models provide sufficient fits, there is little motivation for adding new parameters to the baseline model.

Isocurvature modes are beginning to be constrained by the current CMB polarization data and the upper limits and phenomenological discussion represent a good starting point for future analysis of these more complex models. The CMB polarization data is emerging but is not yet driving parameter determination. In the analysis of the CMBall + HST constraints to a model which includes a CDM isocurvature mixture, the resulting allowed isocurvature CMB bandpower contamination is only a few percent.

In closing, obtaining the final E-mode polarization spectrum was extremely challenging. The polarization signal is buried in the experimental noise and only after very careful treatment of noise cross-correlations was the EE spectrum realized. Of course, in addition to noise considerations, a good understanding of telescope systematics and solid pointing reconstruction are a necessity to obtain any of the CMB angular power spectra. While foregrounds at B03 frequencies and angular scale have been shown to be insignificant for this data set, foregrounds will certainly play a major role in future CMB experiments; when the amplitude of the polarized foreground signal may compete with

the amplitude of the CMB polarization signal. If the polarization data is to be used to independently constrain cosmological models, then all of these factors must be carefully considered. In addition the measurement of the B-mode polarization which is predicted to be at least an order of magnitude lower than the E-mode signal will be extremely sensitive to systematics, experimental beam, foregrounds and noise. At the moment, the standard adiabatic inflationary model is a good fit to the experimental data. However alternate models are not completely ruled out and fit the data well. The measurement of B-mode polarization would be a direct probe of the initial conditions described by Inflation.

Bibliography

[1] Q. R. Ahmad et al. Direct evidence for neutrino flavor transformation from neutral-current interactions in the sudbury neutrino observatory. *Phys. Rev. Lett.*, 89:011301, 2002.

[2] P. Aliani, V. Antonelli, M. Picariello, and E. Torrente-Lujan. The neutrino mass matrix after kamland and sno salt enhanced results. 2003. hep-ph/0309156.

[3] Alexandre Amblard and Jean-Christophe Hamilton. Noise power spectrum estimation and fast map making for cmb experiments. 2003. astro-ph/0307203.

[4] D. Barkats et al. First measurements of the polarization of the cosmic microwave background radiation at small angular scales from capmap. *Astrophys. J.*, 619:L127–L130, 2005.

[5] A Berk et al. Modtran: A moderate resolution model for lowtran 7, air force geophysics laboratory technical report. *GL-TR-89-0122, Hanscom AFB, MA*, 1998.

[6] J. R. Bond and G. Efstathiou. Cosmic background radiation anisotropies in universes dominated by nonbaryonic dark matter. *Astrophys. J.*, 285:L45–L48, 1984.

[7] J. R. Bond and G. Efstathiou. The statistics of cosmic background radiation fluctuations. *Mon. Not. Roy. Astron. Soc.*, 226:655–687, 1987.

[8] J. R. Bond, G. Efstathiou, and M. Tegmark. Forecasting cosmic parameter errors

from microwave background anisotropy experiments. *Mon. Not. Roy. Astron. Soc.*, 291:L33–L41, 1997.

[9] J. R. Bond, A. H. Jaffe, and L. E. Knox. Radical compression of cosmic microwave background data. *Astrophys. J.*, 533:19, 2000.

[10] J. R. Bond and A. S. Szalay. The collisionless damping of density fluctuations in an expanding universe. *Astrophys. J.*, 274:443–468, 1983.

[11] J. Richard Bond, Carlo R. Contaldi, Antony M. Lewis, and Dmitry Pogosyan. The cosmic microwave background and inflation parameters. *Int. J. Theor. Phys.*, 43:599–622, 2004.

[12] J. Richard Bond, Carlo R. Contaldi, and Dmitry Pogosyan. Cosmic microwave background snapshots: pre-wmap and post- wmap. *Phil. Trans. Roy. Soc. Lond.*, A361:2435–2467, 2003.

[13] M. Born and E. Wolf. *Principles of Optics.* New York: Pergamon, 1980.

[14] A. Boscaleri et al. The argo experiment pointing system as an example for other single-axis platform pointing systems. *Measurement Science and Technology*, 5:190, 1994.

[15] M. Bucher, Joanna Dunkley, P. G. Ferreira, K. Moodley, and C. Skordis. The initial conditions of the universe: how much isocurvature is allowed? 2004. astro-ph/0401417.

[16] Gayoung Chon, Anthony Challinor, Simon Prunet, Eric Hivon, and Istvan Szapudi. Fast estimation of polarization power spectra using correlation functions. *Mon. Not. Roy. Astron. Soc.*, 350:914, 2004.

[17] Nelson Christensen, Renate Meyer, Lloyd Knox, and Ben Luey. Ii: Bayesian methods

for cosmological parameter estimation from cosmic microwave background measurements. *Class. Quant. Grav.*, 18:2677, 2001.

[18] C. Contaldi et al. Faster and xfaster cmb power spectrum estimation. *in prep*, 2005.

[19] Brendan P. Crill. *Ph.D. Thesis.* California Institute of Technology, November 2000.

[20] J. Davis and R.J. Webb. The absolute flux distribution of sirius. *Proc. A.S.A. 1 (8)*, 1970.

[21] Clive Dickinson et al. High sensitivity measurements of the cmb power spectrum with the extended very small array. 2004. astro-ph/0402498.

[22] S. Dodelson. *Modern Cosmology.* Academic Press, 2003.

[23] Olivier Dore, Gilbert P. Holder, and Abraham Loeb. The cmb quadrupole in a polarized light. *Astrophys. J.*, 612:81–85, 2004.

[24] Olivier Dore, Lloyd Knox, and Alan Peel. Cmb power spectrum estimation via hierarchical decomposition. *Phys. Rev.*, D64:083001, 2001.

[25] S. Eidelman et al. Review of Particle Physics. *Physics Letters B*, 592:1+, 2004.

[26] Daniel J. Eisenstein et al. Detection of the baryon acoustic peak in the large-scale correlation function of sdss luminous red galaxies. 2005. astro-ph/0501171.

[27] Pedro G. Ferreira and Andrew H. Jaffe. Simultaneous estimation of noise and signal in cosmic microwave background experiments. 1999.

[28] Douglas P. Finkbeiner, Marc Davis, and David J. Schlegel. Extrapolation of galactic dust emission at 100 microns to cmbr frequencies using firas. 1999.

[29] W. L. Freedman et al. Final Results from the Hubble Space Telescope Key Project to Measure the Hubble Constant. *Astrophys. J.*, 553:47–72, 2001.

[30] J. N. Goldberg, A. J. Macfarlane, E. T. Newman, F. Rohrlich, and E. C. G. Sudarshan. Spin-s spherical harmonics and . *J. Math. Phys.*, 8:2155, 1967.

[31] K. M. Gorski et al. Healpix – a framework for high resolution discretization, and fast analysis of data distributed on the sphere. *Astrophys. J.*, 622:759–771, 2005.

[32] N. W. Halverson et al. DASI first results: A measurement of the cosmic microwave background angular power spectrum. *Astrophys. J.*, 568:38–45, 2002.

[33] J. Ch. Hamilton. Cmb map-making and power spectrum estimation. 2003. astro-ph/0310787.

[34] S. Hanany et al. Maxima-1: A measurement of the cosmic microwave background anisotropy on angular scales of 10 arcminutes to 5 degrees. *Astrophys. J.*, 545:L5, 2000.

[35] G. Hinshaw et al. First year Wilkinson Microwave Anisotropy Probe (WMAP) observations: Angular power spectrum. *Astrophys. J. Suppl.*, 148:135, 2003.

[36] E. Hivon et al. Master of the cmb anisotropy power spectrum: A fast method for statistical analysis of large and complex cmb data sets. 2001. astro-ph/0105302.

[37] Wayne Hu and Naoshi Sugiyama. Small scale cosmological perturbations: An analytic approach. *Astrophys. J.*, 471:542–570, 1996.

[38] Wayne Hu, Naoshi Sugiyama, and Joseph Silk. The physics of microwave background anisotropies. *Nature*, 386:37–43, 1997.

[39] Edwin Hubble. A relation between distance and radial velocity among extra-galactic nebulae. *Proceedings of the National Academy of Sciences*, 15, 1929.

[40] G. Huey, L. Wang, R. Dave, R. R. Caldwell, and P. J. Steinhardt. Resolving the cosmological missing energy problem. *Phys. Rev.*, D59:063005, 1999.

[41] W. C. Jones. *Ph.D. Thesis.* California Institute of Technology, May 2005.

[42] W.C. Jones et al. Instrumental and analytic methods for bolometric polarimetry. *in prep*, 2005.

[43] William C. Jones et al. A measurement of the angular power spectrum of the cmb temperature anisotropy from the 2003 flight of boomerang. 2005. astro-ph/0507494.

[44] A. Kogut et al. Wilkinson Microwave Anisotropy Probe (WMAP) first year observations: TE polarization. *Astrophys. J. Suppl.*, 148:161, 2003.

[45] A. Kosowsky, M. Milosavljevic, and R. Jimenez. Efficient cosmological parameter estimation from microwave background anisotropies. *Phys. Rev. D.*, 66:063007, 2002.

[46] Arthur Kosowsky and Michael S. Turner. Cbr anisotropy and the running of the scalar spectral index. *Phys. Rev.*, D52:1739–1743, 1995.

[47] John Kovac et al. Detection of polarization in the cosmic microwave background using dasi. *Nature*, 420:772–787, 2002.

[48] Chao-lin Kuo et al. High resolution observations of the cmb power spectrum with acbar. *Astrophys. J.*, 600:32–51, 2004.

[49] Hannu Kurki-Suonio, Vesa Muhonen, and Jussi Valiviita. Correlated primordial perturbations in light of cmb and lss data. *Phys. Rev.*, D71:063005, 2005.

[50] A. E. Lange et al. Cosmological parameters from the first results of boomerang. *Phys. Rev.*, D63:042001, 2001.

[51] Antony Lewis and Sarah Bridle. Cosmological parameters from CMB and other data: a Monte- Carlo approach. *Phys. Rev.*, D66:103511, 2002.

[52] Antony Lewis, Anthony Challinor, and Anthony Lasenby. Efficient computation of CMB anisotropies in closed FRW models. *Astrophys. J.*, 538:473–476, 2000.

[53] L. Longair. *Galaxy Formation.* Springer, 1998.

[54] C. J. MacTavish et al. Cosmological parameters from the 2003 flight of boomerang. 2005. astro-ph/0507503.

[55] Silvia Masi et al. A self-contained 3he refrigerator for long duration balloon experiments. *Cryogenics*, 38:319, 1998.

[56] Silvia Masi et al. A long-duration cryostat suitable for balloon borne photometry. *Cryogenics*, 39:217, 1999.

[57] Silvia Masi et al. Instrument, method, brightness and polarization maps from the 2003 flight of boomerang. 2005. astro-ph/0507509.

[58] J. C. Mather et al. Measurement of the cosmic microwave background spectrum by the code firas instrument. *Astrophys. J.*, 420:439–444, 1994.

[59] Thomas E. Montroy. *Ph.D. Thesis.* University of California Santa Barbara, June 2003.

[60] Thomas E. Montroy et al. A measurement of the cmb spectrum from the 2003 flight of boomerang. 2005. astro-ph/0507514.

[61] P. Natoli, G. de Gasperis, C. Gheller, and N. Vittorio. A map-making algorithm for the planck surveyor. 2001. astro-ph/0101252.

[62] Radford. M. Neal. Probabilistic inference using Markov Chain Monte Carlo methods. http://www.cs.toronto.edu/~radford/review.abstract.html, 1993.

[63] P. J. E. Peebles and J. T. Yu. Primeval adiabatic perturbation in an expanding universe. *Astrophys. J.*, 162:815–836, 1970.

[64] Arno A. Penzias and Robert Woodrow Wilson. A measurement of excess antenna temperature at 4080-mc/s. *Astrophys. J.*, 142:419–421, 1965.

[65] Will J. Percival et al. The 2dF Galaxy Redshift Survey: The power spectrum and the matter content of the universe. *MNRAS*, 327:1297, 2001.

[66] Francesco Piacentini. *Ph.D. Thesis.* Universita' degli Studi di Roma La Sapienza, December 2003.

[67] Francesco Piacentini et al. A measurement of the polarization-temperature angular cross power spectrum of the cosmic microwave background from the 2003 flight of boomerang. 2005. astro-ph/0507507.

[68] S. Prunet et al. Noise estimation in cmb time-streams and fast map-making. application to the boomerang98 data. 2001. astro-ph/0101073.

[69] Bharat Ratra and P. J. E. Peebles. Cosmological consequences of a rolling homogeneous scalar field. *Phys. Rev.*, D37:3406, 1988.

[70] A. C. S. Readhead et al. Extended mosaic observations with the cosmic background imager. *Astrophys. J.*, 609:498–512, 2004.

[71] A. C. S. Readhead et al. Polarization observations with the cosmic background imager. *Science*, 306:836–844, 2004.

[72] Adam G. Riess et al. Type ia supernova discoveries at z¿1 from the hubble space telescope: Evidence for past deceleration and constraints on dark energy evolution. *Astrophys. J.*, 607:665–687, 2004.

[73] John E. Ruhl et al. Improved measurement of the angular power spectrum of temperature anisotropy in the cmb from two new analyses of boomerang observations. *Astrophys. J.*, 599:786–805, 2003.

[74] U. Seljak and M. Zaldarriaga. A line of sight integration approach to Cosmic Microwave Background anisotropies. *Astrophys. J.*, 469(2):437–444, 1996.

[75] Uros Seljak et al. Cosmological parameter analysis including sdss ly-alpha forest and galaxy bias: Constraints on the primordial spectrum of fluctuations, neutrino mass, and dark energy. 2004. astro-ph/0407372.

[76] Uros Seljak et al. Sdss galaxy bias from halo mass-bias relation and its cosmological implications. *Phys. Rev.*, D71:043511, 2005.

[77] D.S. Sheppard, F. LeGuern, and B.W. Christenson. Composition and mass fluxes of the mount erebus volcano plume,. *Volcanological and Environmental Studies of Mount Erebus, Antarctica*, 66:83–96, 1994.

[78] Anze Slosar, Uros Seljak, and Alexy Makarov. Exact likelihood evaluations and foreground marginalization in low resolution wmap data. *Phys. Rev.*, D69:123003, 2004.

[79] D. N. Spergel et al. First year wilkinson microwave anisotropy probe (WMAP) observations: Determination of cosmological parameters. *Astrophys. J. Suppl.*, 148:175, 2003.

[80] Suzanne Staggs and Sarah Church. Experimental cmb status and prospects: A report from snowmass 2001. *eConf*, C010630:E609, 2001.

[81] R. Stompor et al. From the time-ordered data to the maximum-likelihood temperature maps of the cosmic microwave backgorund anisotropy. 2000. astro-ph/0012418.

[82] Max Tegmark. How to make cmb maps without losing information. *Astrophys. J.*, 480:L87–L90, 1997.

[83] Max Tegmark, Daniel J. Eisenstein, Wayne Hu, and Angelica de Oliveira-Costa. Foregrounds and forecasts for the cosmic microwave background. *Astrophys. J.*, 530:133–165, 2000.

[84] Max Tegmark et al. The 3d power spectrum of galaxies from the sdss. 2003. astro-ph/0310725.

[85] T. Toshito et al. Super-kamiokande atmospheric neutrino results. 2001. hep-ex/0105023.

[86] Matthieu Tristram et al. The cmb temperature power spectrum from an improved analysis of the archeops data. *Astron. Astrophys.*, 436:785–797, 2005.

[87] L. Verde et al. First year Wilkinson Microwave Anisotropy Probe (WMAP) observations: Parameter estimation methodology. *Astrophys. J. Suppl.*, 148:195, 2003.

[88] Licia Verde et al. The 2df galaxy redshift survey: The bias of galaxies and the density of the universe. *Mon. Not. Roy. Astron. Soc.*, 335:432, 2002.

[89] J. Wardell, P.R. Kyle, and C. Chaffin. Co2 emissions from mt. erebus. *International Symposium on Antarctic Earth Science (ISAES).*

[90] M. L. Wilson and Joseph Silk. On the anisotropy of the cosomological background matter and radiation distribution. 1. the radiation anisotropy in a spatially flat universe. *Astrophys. J.*, 243:14–25, 1981.

[91] Matias Zaldarriaga and Uros Seljak. An all-sky analysis of polarization in the microwave background. *Phys. Rev.*, D55:1830–1840, 1997.

[92] Ya. B. Zeldovich. Gravitational instability: An approximate theory for large density perturbations. *Astron. Astrophys.*, 5:84–89, 1970.